BOSE-EINSTEIN CONDENSATION OF MICROCAVITY POLARITONS

by

Ryan Barrido Balili

B.S. Physics, MSU-Iligan Institute of Technology, 2002

M.S. Physics, University of Pittsburgh, 2005

Submitted to the Graduate Faculty of

the Department of Physics and Astronomy in partial fulfillment

of the requirements for the degree of

Doctor of Philosophy

University of Pittsburgh

2009

UNIVERSITY OF PITTSBURGH

DEPARTMENT OF PHYSICS AND ASTRONOMY

This dissertation was presented

by

Ryan Barrido Balili

It was defended on

June 11, 2009

and approved by

David W. Snoke, Professor, Physics and Astronomy

Hrvoje Petek, Professor, Physics and Astronomy

W. Vincent Liu, Assistant Professor, Physics and Astronomy

Robert Coalson, Professor, Chemistry

P. Kevin Chen, Assistant Professor, Electrical and Computer Engineering

Dissertation Director: David W. Snoke, Professor, Physics and Astronomy

BOSE-EINSTEIN CONDENSATION OF MICROCAVITY POLARITONS

Ryan Barrido Balili, PhD

University of Pittsburgh, 2009

The strong coupling of light and excitons in a two-dimensional semiconductor microcavity results in a new eigenstate of quasiparticles called polaritons. Microcavity polaritons have generated much interest due to the wealth of interesting optical phenomena recently observed in these systems such as nonlinear emission, macroscopic coherence, and bosonic stimulated scattering. The efficiency of amplification, parametric oscillation, and coherent emission of light makes it promising for applications in coherent control, microscopic optical switching, and other opto-electronic devices. Most of all, because of their light mass and bosonic character, these particles are predicted to undergo Bose-Einstein condensation (BEC) at much higher temperatures and lower densities than their atomic counterparts.

Standard methods of growing semiconductor microcavities are quite inefficient in producing well-tuned samples with strong coupling of light and excitons. Wafers with continuously varying thicknesses are often produced, leaving only tiny regions with strong coupling. In our experiments, an inhomogeneous stress is applied to the microcavity in order to actively couple naturally detuned exciton and cavity modes at fixed $k_{||} = 0$, and at the same time, create an in-plane spatial trap, potentially making BEC of polaritons possible.

Our recent experiments with exciton-polaritons in the stress trap have shown compelling evidence of BEC. At the bottom of the trap where the coupling is strongest, line narrowing and nonlinear increase of photoluminescence intensity are observed. Also a single, spatially narrow condensate of polariton gas is formed analogous to the case of atoms in a three-dimensional harmonic potential. Above a critical density, we observe a massive occupation of polaritons in the ground state, spontaneous build-up of linear polarization, and macroscopic

coherence of the condensate all in agreement with predictions. The results are similar to what is observed in the naturally resonant unstressed case. Comparison with the stressed trap and the nonstressed case, however, revealed that stress traps play a significant contribution in forming a polariton condensate. Furthermore, the stress trap case has shown, where the unstressed case has not, two distinct thresholds, one from photon lasing and another from a BEC transition.

Keywords: stress, trapped, polariton BEC, condensation, polaritons, semiconductor, microcavities.

TABLE OF CONTENTS

LIST OF TABLES

LIST OF FIGURES

To my greatest mentors, my parents, George and Mercy, who taught me how to live and, more importantly, how to love.

PREFACE

Before anything I else, I thank God for the strength he has given me all these years to continue my studies here in University of Pittsburgh. To Him belongs all glory and honor!

This thesis would not have been possible if not for my wife, Nikki, who has been my constant support and ecouragement all these years. Your encouragement has made our challenges more bearable. Life has been so much more enjoyable since you came along.

I am thankful for the encouragement of my parents, my brother and my sisters.

The results of my experiments and my progress as a student would not have reached its completion with out the support and guidance of my supervisor Prof. David Snoke. He never left me behind and was with me from beginning to the end. To him I express my gratitude.

I am thankful for my committee members, K. Chen, H. Petek, V. Liu, and R. Coalson for taking time to watch my progress as a graduate student.

I am also grateful for Yingmei Liu and Sava Denev who showed me the ways of the lab when I was still new with the group.

I would like to thank V. Hartwell, Z. Vörös, B. Zhang, C. Yang, B. Nelsen, J. Wuenschell, N. Sinclair, and A. Heberle for their invaluable comments, discussions, and help in many of my experiments. I would like to give special mention to B. Giles, K. Petrocelly and K. Kotek whom I had the pleasure working with in the machine shop. I thank them for the friendship and the wonderful times we spent working, learning, and playing together when we had the chance.

I am also indebted to Engr. R.H. Reid for helping me with the stress simulations using ANSYS. It would have taken me a long time to finish the final part of my PhD work with out his assistance.

Furthermore, this dissertation would not be possible if not for the semiconductor microcavity samples sent by L. Pfeiffer and K. West from Bell Labs. I am also grateful to our collaborators in Stanford University and H. Deng, G. Weihs, and Y. Yamamoto for contributions to the initial design of the samples. The preliminary research has been supported by the National Science Foundation under Grant No. 0404912 and by DARPA under Army Research Office Contract No. W911NF-04-1-0075.

Ryan B. Balili

Pittsburgh, PA

1.0 INTRODUCTION

1.1 OVERVIEW

In 1925, after generalizing Satyendra Nath Bose's work on the statistics of monoatomic ideal gases, Albert Einstein speculated that, at very low temperatures, a certain type of identical particles, now called bosons, would "collapse" or condense into its lowest energy state. This particle state is called the *Bose-Einstein condensate* (BEC). Previously observed macroscopic quantum phenomena like superfluidity and superconductivity were later successfully explained by the theory of BEC [1, 2, 3, 4]. In 1995, two independent teams, from NIST-JILA and MIT, lead by Eric Cornell and Wolfgang Ketterle, respectively, verified the Bose-Einstein condensation of rubidium and sodium atoms experimentally [5, 6], earning them the Nobel Prize for Physics in 2001. How did this interesting phenomenon come about? The explanation lies at the very heart of quantum theory. According to Louis de Broglie's postulate on wave-particle duality, all matter and radiation have wave and particle aspects. The associated wavelength of a particle is given by Planck's constant $h = 6.63\times10^{-34}\,\mathrm{kg\cdot m^2/s}$ divided by the particle's momentum p i.e $\lambda = h/p$. A particle's average velocity corresponds to the temperature in thermal equilibrium, given by $v = \sqrt{3k_BT/m}$ where $k_B = 1.38\times10^{-23}\,\mathrm{kg\cdot m^2/(K\cdot s^2)}$ is Boltzmann's constant. In other words, $p \propto \sqrt{mT}$ or $\lambda \propto 1/\sqrt{mT}$. At very low temperatures or with extremely light particles, the particle's momentum becomes so small that the de Broglie wavelength becomes comparable to the distance between particles (see Figure 1.1). The particles, or wave-packets in the wave nature point of view, start "adding up" or superposing constructively. A highly ordered state arises such that a macroscopic collection of these particles becomes dependent on a single wave function. All the particles thus behave in the same manner, spectacularly amplifying

the quantum nature of the individual particles.

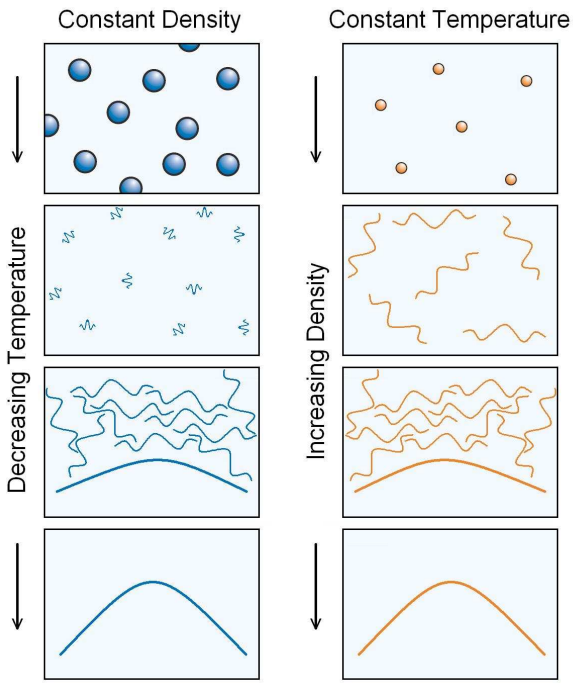

Figure 1.1: Criteria for achieving BEC. *Left:* For heavier particles temperatures must be decreased a lot to increase de Broglie wavelength. *Right:* For lighter particles, associated wavelength's are longer. Decreasing the distance between particles by increasing density can be an open variable for creating a condensate. In both methods, the same macroscopic condensate or wave comes out in the end.

The critical temperature for BEC of atoms is remarkably low. Atomic BEC physicists often boast of their system as the coldest place in the universe, down to the nanokelvin temperatures. Reaching close to absolute zero temperature was such a daunting feat in itself. It required advanced cryogenic systems and sophisticated techniques some of which have earned their own Nobel Prize (e.g. method of laser cooling [7]). Though BEC opened doors to new physics, it is imperative that we increase its critical temperature for any practical applications. This can be achieved if we use particles with far smaller mass (see Fig. 1.1). This is where polaritons come in.

Microcavity polaritons (MCPs) have in the past decade been the object of great interest for many scientists [8, 9, 10, 11, 12, 13, 14, 15, 16, 17, 18, 19] for its phenomenal optical properties and for those interested in the study of BEC. A polariton is a mixed state of a bound electron-hole pair and a photon. Electron-hole pairs are created when an electron is excited in a semiconductor and leaves a hole in the lattice. Given the right conditions, the electron binds with a positively charged hole, forming an exciton, a quasi-particle very much like a hydrogen atom. When an exciton couples with a photon, a polariton is created which

is a superposition of its original components. Polaritons are very light particles, making BEC possible even at room temperature.

Polaritons decay by emitting light with energy and momentum corresponding to the state of the polariton. The lifetime is short in semiconductor microcavities, as it is mainly dependent on how long the photon stays in the cavity. A microcavity is made up of two highly reflective mirrors facing each other. Sandwiched in the microcavity are quantum wells where the excitons are created. When trapped in an optical cavity, the photons couple with the excitons much more effectively, creating a strongly coupled polariton state. Increasing the quality of the mirrors increases the lifetime of the polaritons. Given sufficient density of particles, some will be able to scatter to the lowest energy state. Once a polariton occupies the lowest energy state, scattering to that state is enhanced considerably, leading to a macroscopic condensate. As the polariton condensate decays, intense coherent and monochromatic light is emitted. This spontaneous coherence effect has inspired the creation of new opto-electronic devices, namely the "polariton laser". Below a critical temperature, this new generation of "lasers" would not require population inversion and would have very low thresholds.

1.2 BRIEF SURVEY OF MICROCAVITY POLARITON RESEARCH

The study of exciton-polaritons in bulk materials began as early as 1958 with J. Hopfield[20] who first suggested the linear coupling of electronic excitations to the electromagnetic field. Application of the polariton concept to lower dimensional systems was later investigated in quantum wells (QWs) but failed to show evidence of normal-mode coupling since a two-dimensional (2D) QW exciton couples to a three-dimensional (3D) continuum of photon modes leading to an enhanced radiative decay[21, 22]. The first successful observation of strong coupling in two dimensions was made in 1992 by C. Weisbuch[23] in a semiconductor microcavity. By then, technological advancement in growing heterostructures allowed the manufacture of highly reflective dielectric mirrors. Photons, even those that are normal to the cavity, i.e. with zero in-plane momenta, lived long enough for the vacuum-field

Rabi oscillation frequency, which is proportional to the coupling strength, to be faster than the escape rate[24]. At that time, observations were understood as a semiclassical linear coupling of excitons to an light field in analogy with atoms in a resonant optical cavity[25]. Soon after, an equivalent quantum description was developed[26, 27], treating a quantized excitation coupled with a quantized light field.

The BEC transition in MCPs was first suggested by Imamoglu et. al.[28] in 1996. Not long after, evidence of final-state stimulation in microcavity systems under non-resonant excitation was reported[29, 30, 31, 8, 9]. Non-resonant pumping means generating carriers that have different energy from the final state of interest. This can be done by exciting either with high energy or with large in-plane momentum so that carriers emit many phonons, thereby losing coherence, before reaching the final state. Populating the ground state can also be done more directly using resonant excitation. This is achieved by simply pumping the low polariton energy levels with energy close to the ground state. Population build up of polaritons is more efficient using resonant excitation than using high-energy non-resonant excitation, where carriers are subject to decay during thermalization and suppressed relaxation caused by the "bottleneck effect" (see Section 2.2). However, in resonant pumping, residual coherence from the laser may affect the correlation observed in the ground state[32]. Resonant pumping also can give rise to parametric scattering process (see Section 2.2). These effects are interesting in themselves, with a variety of important applications, from coherent control[12] to creating entangled polariton states[33]. Nevertheless, the correlated behavior observed cannot be described in the physics of spontaneous thermodynamic phase transition, although this has been debated recently[34].

Our interest, however, is nonresonant excitation, i.e., incoherent pumping of particles. Several nonresonant excitation schemes have already indicated spontaneous coherence of polariton gas in various two-dimensional microcavity structures at around 4 Kelvin (e.g. Refs. [14, 8]). Though this is still not room temperature, it is a big improvement on the nanokelvin temperatures in atomic BEC. However, in these experiments, no confining potential was applied to trap the polaritons. In their systems, polaritons are generated only where the laser is focused. Polaritons diffuse freely away from the excitation region and fall into the local minima created either by disorder or the laser itself. This makes it hard to define what

the ground state is. In addition, coherent effects were only seen at the same place where the microcavity was excited and only when the laser was on. Polaritons generated in their microcavities did show signatures of a Bose-Einstein condensate such as nonlinear increase in photoluminescence emission and coherence. Nevertheless, a fundamental question has remained unanswered. Because the signatures of BEC are only seen where the laser excites the sample, is it possible that these effects are due to the driving of the laser itself? Part of my research has been to explore different schemes that may avoid facing this dilemma. Various techniques, such as creating a potential trap, pumping the microcavity with excess energy, and generating polaritons away from the trap are among those employed to remove ambiguities associated in the determination between BEC and ordinary photon lasing.

1.3 THESIS OUTLINE

This dissertation is organized as follows. In Chapter 2, I will briefly review the fundamental concepts involved in understanding MCPs. The physics behind the exciton-photon interaction, which is based on the optical response of particles with in each quantum well, will be discussed in this chapter. I will begin by treating this interaction quantum mechanically, which involves diagonalizing the exciton-photon Hamiltonian. After this, a semiclassical treatment is presented in the form of a transfer-matrix formalism, which is very useful in simulations and characterization of microcavities. In Chapter 3, I will discuss the physics behind the BEC phenomenon in two dimensions. I will also summarize key features of MCPs that have helped and challenged the prospects of finding BEC.

The main objective of my research is to investigate a possible thermodynamic transition to a Bose-Einstein condensate of MCPs. I will describe the relevant experimental procedures called for in order to reach that goal in Chapters 4 and 5. After that, in Chapters 6 and 7, I will proceed with detailing various experiments and results of our own microcavity samples that show evidence of BEC and other interesting physics for different pumping schemes. Every now and then, I will mention important experiments from other groups that have found similar phenomena. When comparing our results with other groups, significant

differences will be pointed out. In Chapter 8, I will present the latest feature observed and measured in stressed microcavities, namely the splitting of the polaritons states with stress. The current accepted theory for the splitting will be presented. I will also include simulations and numerical fits to the splitting data. Finally, I will give my conclusions in Chapter 9. Details of important calculations, simulations, and theories are attached in the Appendix.

2.0 MICROCAVITY POLARITONS

2.1 COUPLED QUANTUM OSCILLATOR MODEL

A semiconductor microcavity is made up of a Fabry-Perot cavity sandwiched between two reflectors facing each other with quantum wells (QWs) embedded in between. The reflectors, called distributed Bragg reflectors (DBRs), are made up of alternating quarter-wave layers of semiconductor materials with high and low indices of refraction. Confinement in the cavity leads to the quantization of the photon energy in the growth direction while the in-plane photon states remain unaffected. The exciton states of the embedded quantum wells also exhibit similar quantization in the growth direction and continuous states in the free in-plane motion. If the exciton and the cavity modes are in resonance with each other, the coupling of light and excitons occurs, creating the mixed matter-light quasi-particles we call polaritons. The dispersion relations of bare exciton and light mode no longer exist in this regime but two distinct dispersion called the polariton branches.

The bare cavity photon dispersion relation can be easily derived noting that the DBR's force the axial wave vector k_z to be quantized (see illustration on Fig. 2.1). Hence

$$E_{ph} = \hbar c k = \hbar c \sqrt{k_z^2 + k_{||}^2} = \hbar c \left[\left(\frac{N\pi}{n_{\text{eff}} L_c} \right)^2 + k_{||}^2 \right]^{1/2} \tag{2.1}$$

where k_z is along the epitaxial growth direction, $k_{||}$ is the wavevector parallel to the quantum well, L_c is the effective cavity length, n_{eff} is the effective intracavity index of refraction, and N is the mode number or the number of half-wavelengths in the cavity. For our microcavity ($n_{\text{eff}} \approx 3.6$, $L \approx 320$ nm), the mode spacing is 0.54 eV. Our microcavity (see structure in Appendix C) was designed to for an $N = 3$ cavity mode resonance, which means there are

three antinodes in the cavity. Quantum wells are placed in the antinodes, where the field intensity is maximum. This ensures optimum overlap between the exciton and the photon field.

The exciton in a QW has energy

$$E_{ex} = E_0 + \frac{\hbar^2 k_{||}^2}{2(m_e + m_h)} \tag{2.2}$$

where E_0 is the ground state exciton energy and $m_e(m_h)$ is the electron(hole) in-plane mass. Notice that the photon and the exciton is given the same in-plane momentum $k_{||}$. This is due to momentum conservation required by the in-plane translational invariance of the system. This results in the coupling of an exciton and photon with the same in-plane wave vector.

We can then treat the exciton and photon modes as coupled oscillators with coupling matrix element Ω. Using the exciton state $|ex\rangle$ and photon state $|ph\rangle$ as basis, the coupling is described by the matrix Hamiltonian (see Appendix A):

$$H = \begin{bmatrix} E_{ex} & \Omega/2 \\ \Omega/2 & E_{ph} \end{bmatrix} \tag{2.3}$$

where E_{ph} and E_{ex} are the energies of the cavity photon and exciton mode respectively. The eigenvectors of this Hamiltonian is a superposition of the exciton and photon states which can be represented as

$$\begin{aligned} |UP\rangle &= C\,|ex\rangle + X\,|ph\rangle \\ |LP\rangle &= X\,|ex\rangle - C\,|ph\rangle \end{aligned} \tag{2.4}$$

where

$$X^2 = \frac{1}{2} + \frac{E_{ph} - E_{ex}}{2\sqrt{(E_{ph} - E_{ex})^2 + \Omega^2}} \quad \text{and} \quad \mathrm{C}^2 = 1 - \mathrm{X}^2 \tag{2.5}$$

are the standard Hopfield coefficients[20, 35] describing the fraction of the exciton and the photon content of the polariton. The two coupled mode eigenstates of the system are called

the upper polariton (UP) and the lower polariton (LP), corresponding to the higher and the lower energy states, respectively. Diagonalizing the Hamiltonian we get the eigen energies

$$E_{\substack{UP\\LP}} = \frac{E_{ex} + E_{ph}}{2} \pm \left[\left(\frac{E_{ex} - E_{ph}}{2} \right)^2 + \left(\frac{\Omega}{2} \right)^2 \right]^{1/2} . \tag{2.6}$$

The energy splitting of these two modes at resonance is referred to as the Rabi splitting ($\Omega/2$) or the coupling constant (Ω). It is a function of the quantum oscillator strength f which contains the electric dipole matrix elements of the atomic transitions. It is also dependent on the number of atomic oscillators which is proportional to the number of QWs. To trace the physics behind the coupling term Ω and oscillator strength f, a more detailed derivation from the quantum theory of a classical dielectric is presented in Appendix B. The coupling constant can be determined experimentally by measuring the minimum splitting between the UP and LP spectral lines[1]. If we include exciton broadening δ_{ex} and cavity line broadening δ_{ph}, a more realistic form the UP and LP energies is given by

$$E_{\substack{UP\\LP}} = \frac{E_{ex} + E_{ph} - i\left(\delta_{ex} + \delta_{ph}\right)}{2} \pm \left[\left(\frac{E_{ex} - E_{ph} - i\left(\delta_{ex} - \delta_{ph}\right)}{2} \right)^2 + \left(\frac{\Omega}{2} \right)^2 \right]^{1/2} . \tag{2.7}$$

When the splitting is larger than the difference in line widths of the exciton and the cavity lines ($|\delta_{ex} - \delta_{ph}| \ll \Omega$), then the system is considered to be in the strong-coupling regime.

Because of the finite lifetime of the photon component, MCPs convert directly into external photons. The direct correspondence of the polariton state inside the cavity with the outgoing photons allows one to easily examine its dispersion curve in reflectivity and luminescence measurements. Note that $\sin\theta = k_{||}/k$. Using the equation of the cavity photon dispersion we get the relationship between the $k_{||}$ wave vector and the angle (θ) as $k_{||} = \frac{E_{ph}}{\hbar c} \sin\theta$. Hence, a particular $k_{||}$-mode can be accessed simply by selecting the angle (θ) of the pump laser injection. In the same way, by recording the PL spectra as a function of emission angle, we can get a complete measurement of the momentum and energy distribution of polaritons.

[1]Typical values of the Rabi splitting are in the order of meV. It is also worth pointing out that the typical values of the longitudinal-transverse (LT) splitting are of the order of μeV [35] and are only significant at incident or emission angles far from normal.

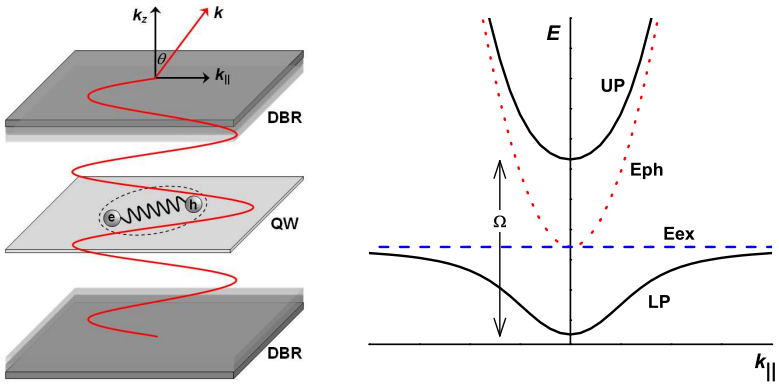

Figure 2.1: *Left:* Basic structure of microcavities and illustration of the photon-exciton oscillator coupling. *Right:* Dispersion relation of the upper and lower polariton (solid curves).

In our experiments, a reservoir of free carriers are first created in the electron-hole continuum by pumping the microcavity with a high energy laser 130 meV above LP energy. The carriers cool subsequently by emitting phonons. As the carriers lose energy, they bind into excitons and interact with cavity photons populating the polaritons states. This pumping scheme allows the particles to lose coherence imparted by the pump laser. Polaritons decay by emitting photons corresonding to its state in the dispersion which can then be measured using standard techniques of photoluminescence spectroscopy.

2.2 FEATURES OF THE MICROCAVITY POLARITON

2.2.1 Weakly Interacting and Light Mass

It is well established [36] that MCPs behave as a gas of weakly interacting bosons. The cavity photons are essentially non-interacting. Polaritons owe their short-range interaction to their exciton components. The the half-light, half-exciton character of the polaritons, with the photon component having a very steep dispersion, gives it a very small in-plane

mass. For the sample used in our experiments, we measured the mass[2] of the polaritons to be 7×10^{-5} times the vacuum electron mass [37]. This makes MCPs very interesting to study in relation to BEC and in relation to a new generation of opto-electronic devices that can be designed based on the BEC of polaritons. In addition, the distinct dispersion of this system has produced a wealth of interesting optical phenomena such as nonlinear emission, polaritonic amplification, and reports of bosonic stimulated scattering [8, 9, 10, 15].

2.2.2 Lifetime Variation in Momentum Space

The lifetime of excitons in the QWs is in the order of nanoseconds. Polaritons, however, are a mix of excitons and photons, making their lifetime much shorter than the exciton lifetime. In the microcavity, the polariton lifetime is very much limited by the quality of the DBRs. The higher the reflector quality, or Q-factor, the longer the photon stays in the cavity, the longer the polariton lifetime. The value of the Q-factor, $Q = \lambda_c/\Delta\lambda_c$, where λ_c is the cavity resonance, is equivalent to the average number of round trips of a photon inside the cavity. For our MC sample, with cavity resonance $\lambda_c = 775.7$ nm and resonance width of $\Delta\lambda_c = 0.2$ nm, $Q \approx 3880$. The estimated photon lifetime, $\tau_{ph} = 2n_{\text{eff}}LQ/c$, in the cavity is about 30 ps, where the effective cavity index $n_{\text{eff}} \approx 3.6$, cavity length $L \approx 320$ nm and c is the speed of light.

Quantitatively, the polariton lifetime τ depends on the fraction and lifetime of each individual photon and exciton component, according to

$$\tau = \left(\frac{f_{ph}}{\tau_{ph}} + \frac{f_{ex}}{\tau_{ex}} \right)^{-1}, \tag{2.9}$$

where $f_{ph}(f_{ex})$ and $\tau_{ph}(\tau_{ex})$ are the photon(exciton) fraction and the bare photon(exciton) lifetime. Note that $f_{ex} = 1 - f_{ph}$ where $f_{ex} = X^2$ and $f_{ph} = C^2$ from Eq. (2.5). The amount

[2]The effective mass m is given by

$$m = \frac{\hbar^2}{d^2E(k_{||})/dk_{||}^2}, \tag{2.8}$$

where $E(k_{||})$ is the energy dispersion and $k_{||}$ is the in-plane momentum. The curvature $d^2E(k_{||})/dk_{||}^2$ can be calculated by fitting the dispersion relation, deduced from angle-resolved measurements (e.g. Fig. 7.5), with a parabola.

of mixing is dependent on the particular shape of the photon and exciton dispersion $E(k_{||})$. The photon fraction f_{ph} is given by[35]

$$f_{ph} = \frac{1}{2} - \frac{E_{ph}(k_{||}) - E_{ex}(k_{||})}{2\sqrt{\left(E_{ph}(k_{||}) - E_{ex}(k_{||})\right)^2 + \Omega^2}} \tag{2.10}$$

where E_{ph} is the cavity photon energy and E_{ex} is the exciton energy for a particular in-plane wavevector $k_{||}$, and Ω is the coupling constant. Hence, polaritons in the ground state have a much shorter lifetime compared to polaritons at higher energy states. This is detrimental to creating a condensate in thermal equilibrium. For the sample studied, at resonance, the lifetime of the lower polaritons was measured, using second harmonic cross-correlation, to be about 7.7 ps [38], which is comparable to polariton lifetime reported elsewhere in similar structures [9]. Fortunately, absolute time scales are irrelevant in the BEC transition. What matters is the thermalization time compared to the lifetime of the polaritons, and the thermalization time can be in the sub-picosecond range.

Knowledge of the lifetime variation in momentum space is also important later in Chapter 6.2 and Chapter 7.4 for converting from raw PL intensity to occupation number. For a constant number of polaritons, the shorter the lifetime of a polariton, the more intense the PL, since at a given detection time more particles decay from a particular state. The PL intensity is converted to occupation number by the lifetime correction.

2.2.3 Bottleneck Effect

Another important feature of the polaritons is called the "bottleneck effect" which arises due to the steep region of the the lower polariton branch and the reduced exciton fraction in as the polaritons become more photonlike. Ideally, optically excited electrons and holes that are created in the quantum well form excitons and thermalize through interaction with each other, with other free carriers, and by interacting the lattice phonons. However, thermalization due to scattering with phonons is much slower as polaritons become more photonlike[39, 38]. In addition, as discussed in the previous section, recombination times are much shorter for photonlike polaritons. These effects result in a depletion region near the zone center and a reduced polariton relaxation in that area. In the "bottleneck" region,

phonons cannot provide an efficient polariton relaxation because of a reduced density of states (see Fig. 2.2). Nevertheless, our group [40] and others [30, 41] have seen a nonlinear increase in luminescence from the ground state even with non-resonant optical pumping. These results suggest that other relaxation mechanisms overcome this "bottleneck". The primary mechanism is polariton-polariton scattering [38]. If has also been suggested that free carrier scattering with polaritons may play a role [38, 11].

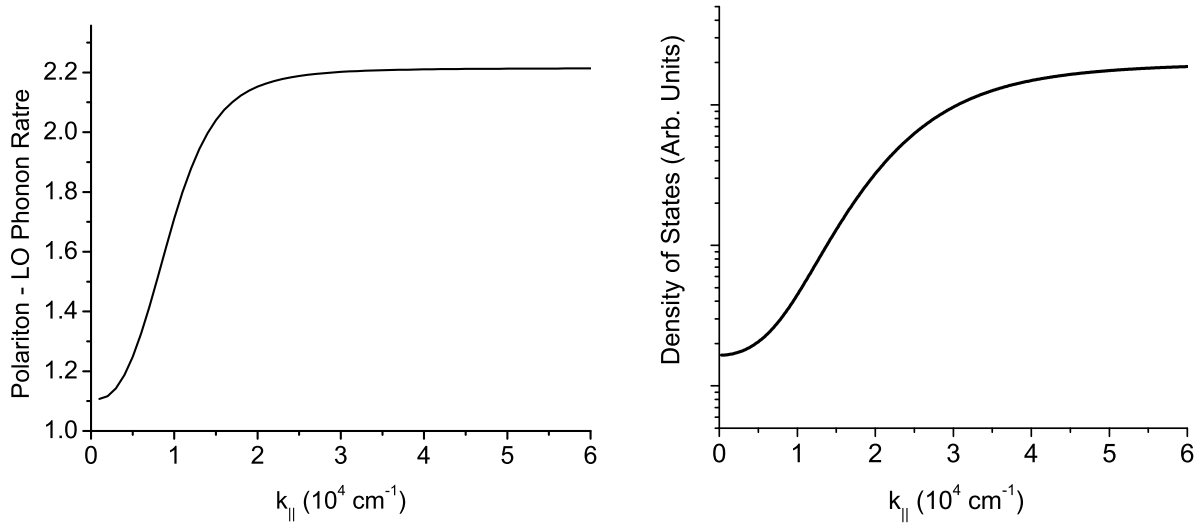

Figure 2.2: Left: Scattering rate of polaritons via longtitudinal optical phonon emission solved using Fermi Golden Rule[42, 38]. Right: Density of states of the lower polariton.

2.2.4 Magic Angle

The shape of the lower polariton branch allows energy-momentum conserving scattering processes into the polariton ground state at a particular in-plane wavenumber k often called the "magic angle"(see Fig. 2.3). Two polaritons under resonant pumping can scatter into zero and $2k$ states with energies E_0 and E_{2k} such that $2E_k = E_0 + E_{2k}$. Basically, an optical parametric oscillation is achieved where the signal (E_0) and idler (E_{2k}) pair created leaves the microcavity at different angles corresponding to their k state [43, 44, 12, 45]. This parametric processes has been shown to have long coherence times[12], making them ideal for coherent-control applications. The short duration and efficiency of amplification also

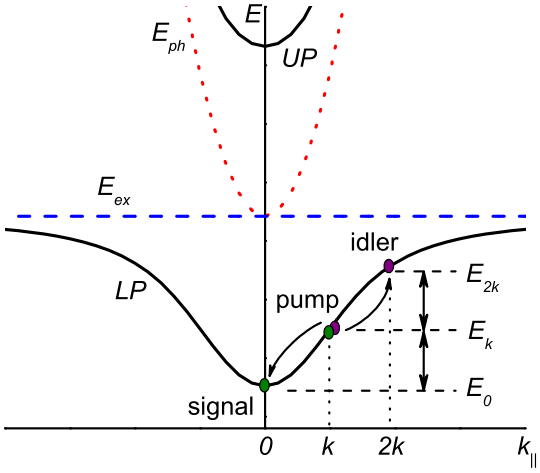

Figure 2.3: Dispersion curve showing optical parametric scattering when pumping resonantly at the magic angle corresponding to $2k$-wavevector.

makes it promising for applications in high-speed microscopic optical switching, and other opto-electronic devices.

There are two experimental schemes involving parametric processes in microcavity polaritons that are being widely studied. The first is called parametric amplification[43], where a resonant laser probes the signal. The probe beam effectively intitiates the parametric process, which subsequently amplifies the signal intensity as the the pump is converted to signal and idler. This behavior can be explained classically[46, 47] as a non-linear four-wave mixing effect satisfying the energy conservation condition

$$2F_p(\omega_p, \vec{k}_p) = F_s(\omega_s, \vec{k}_s) + F_i(\omega_i, \vec{k}_i)\ , \tag{2.11}$$

where F_p, F_s, and F_i correspond to pump, signal, and idler field amplitudes with their respective energies ω_p, ω_s, and ω_i. The phase matching condition, $2\vec{k}_p = \vec{k}_s + \vec{k}_i$, requires the phases to be locked for momentum to be conserved as well. The second scheme is called parametric photoluminescence, where a coherent signal is observed even without a probe beam. This can not be accounted for in strictly classical terms, which dictate that a signal and idler must be present beforehand. Semiclassically, the process is driven by vacuum-field fluctuations of the signal and idler mode[47] which mixes with the pump wave. Some theorists[48] suggest that, in the schemes described above, the signal undergoes spontaneous symmetry breaking or ordering just like BEC. This remains a controverial issue since the

transition cannot be described in terms of spontaneous thermodynamic phase transitions. That is why we avoid magic-angle experiments.

2.2.5 Polariton Spin and Polarization

The exciton ground state in the quantum well is formed by an electron with $\pm\frac{1}{2}$ spin and a heavy hole with $\pm\frac{3}{2}$ spin projection. Hence, heavy hole excitons with total spin of ±1 and ±2 are possible. These spin states are degenerate in energy for a (001)-grown GaAs quantum well whose symmetry is D_{2d}. Note that a photon has spin ±1. Thus, excitons with ±2 spin cannot be optically excited. These are called the optically inactive, "dark" states. The optically active, "bright" state excitons have spin $+1$ and -1 which can be excited by ω^+ and ω^- circularly-polarized light respectively as shown on Fig. 2.4. The exciton-polariton has the same spin profile as the bare exciton. In addition, since only the "bright" exciton states couple to light, only these states are shifted in energy by the Rabi splitting. The "dark" states remain unchanged. This effectively increases the exciton binding energy since the excited states are also not resonant to the cavity mode or does not couple to light.

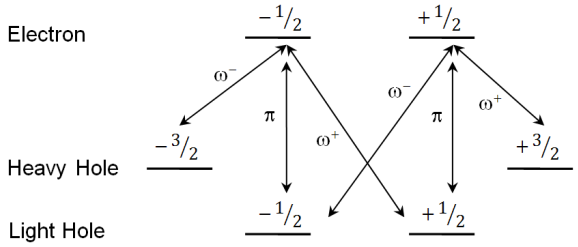

Figure 2.4: Polarization of the optical transitions in GaAs quantum wells. The $\omega^+(\omega^-)$ and π are the right(left) circular and linear polarization respespectively.

Stress shifts both the heavy-hole excitons and light-hole excitons. In the stress-trap geometry used in our GaAs microcavities (discussed in Chap. 4), the light-hole excitons shift in energy more than the heavy-hole excitons. With enough strain, the heavy-hole and light-hole states eventually have an anti-crossing. The resulting eigenstates at the point of anti-crossing,

$$E_+ : \left|\frac{3}{2}\right\rangle - i\left|-\frac{1}{2}\right\rangle, \left|-\frac{3}{2}\right\rangle + i\left|\frac{1}{2}\right\rangle, \tag{2.12}$$

$$E_- : \left|\frac{3}{2}\right\rangle + i\left|-\frac{1}{2}\right\rangle, \left|-\frac{3}{2}\right\rangle - i\left|\frac{1}{2}\right\rangle, \tag{2.13}$$

are linearly polarized. The mixing of the heavy- and light- hole excitons due to stress, coupled with the exchange interaction terms in the quantum well, leads to a fine structure splitting of the quantum well excitons. The splitting of the excitons then leads to a splitting in the observed polariton lines. This effect, seen in our stressed microcavity sample, will be explained in more detail in Chap. 8.

2.3 TRANSFER MATRIX FORMALISM

The transfer matrix method allows one to simulate the reflectivity, absorption, and transmission of periodic structures effectively. A plane wave of wavelength λ incident on a stack of dielectric materials of various thicknesses t_j and indices of reflectivity n_j will have reflected and transmitted components. We can write electric field as a sum of forward and backward moving waves

$$E = E_+ e^{ikx} + E_- e^{-ikx}. \tag{2.14}$$

The field components through an interface and after propagating through a layer can be solved by a transfer matrix equation $E' = T_M E$ where T_M is the effective matrix contribution of all the layers and interfaces. The transfer matrix across an interface is given by

$$T_{int} = \frac{1}{2} \begin{pmatrix} n+1 & -(n-1) \\ -(n-1) & n+1 \end{pmatrix} \tag{2.15}$$

The transfer matrix across a layer is given by

$$T_{layer} = \begin{pmatrix} e^{ik_j t_j} & 0 \\ 0 & e^{-ik_j t_j} \end{pmatrix} \tag{2.16}$$

The T_M resultant product of all the different matrices across the layers and interfaces.

$$T_M = \begin{pmatrix} t_{11} & t_{12} \\ t_{21} & t_{22} \end{pmatrix} = T_1 T_2 T_3 ... T_n \tag{2.17}$$

The layer structure of the microcavity sample used in our experiments is shown in Appendix C. An example of a transfer matrix simulation at room temperature for our microcavity sample is shown in Fig. 2.5. The simulation does not exactly fit the data but it gives a good indication of the thicknesses of the layers and the positions of the cavity modes and resonances. The actual microcavity reflectivity is subject to noise, flat-field correction, instrumental limitations, and absorption of the medium. The primary discrepancy is attributed to the lack of an accurate, continuous absorption data, as a function of temperature and incident wavelength, needed for fitting a huge spectral range. Absorption increase significantly around and above the exciton energy peak where photons have enough energy to create free carriers[49].

The transmitted and reflected electric fields are given by

$$E_{trans} = \frac{\det(T)}{t_{22}} E_{inc} \ , \quad E_{ref} = -\frac{t_{21}}{t_{22}} E_{inc}, \tag{2.18}$$

and the reflectivity is given by

$$R = \frac{E_{ref}^2}{E_{trans}^2}. \tag{2.19}$$

It is important to identify some parts of the reflectivity spectrum which will be pointed out later in this thesis. The flat, high reflective region is often called the stop band. At the middle of the stop band, a dip in reflectivity exists called the cavity mode. At low temperatures, a cavity mode may couple with a QW exciton, creating two dips in the reflectivity stop band which correspond to the upper and lower polariton. The higher energy or shorter wavelength edge of the stop band, often called the stop band edge, is where we often pump the sample with a laser. This has the advantage of high absorption and also provides a source of incoherent excitons since carriers must emit many phonons to cool to the lowest exciton states.

Casting the semiclassical theory of the exciton-photon interaction in the transfer matrix simulations is very useful in empirically measuring parameters such as the oscillator strength of an individual QW, which is used in calculating the splitting of the polariton states and in simulating the shifts in polariton energy across the sample with stress or cavity length variation. A good fit to experiment involves getting realistic models for the dielectric constants

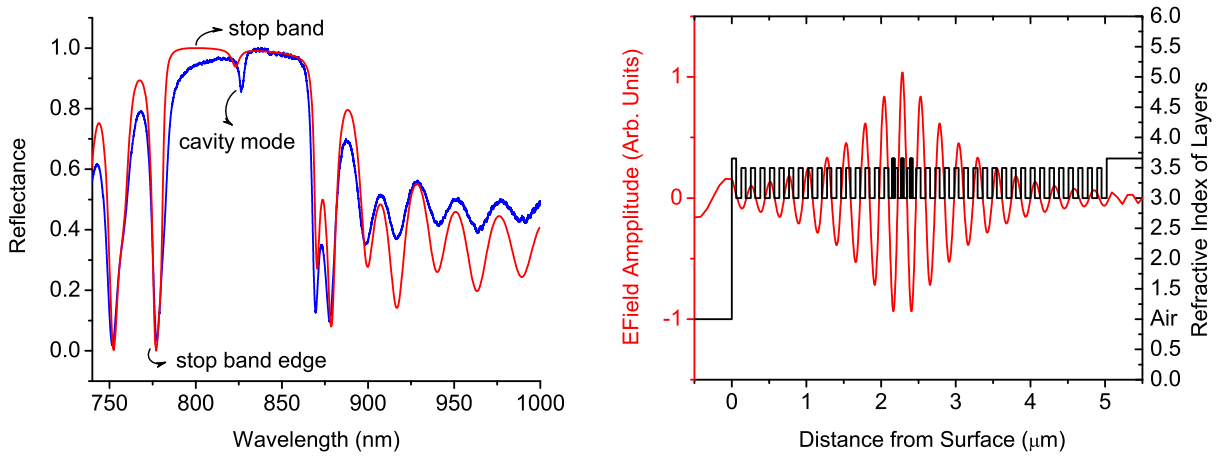

Figure 2.5: Left: Comparison of an actual normal incidence reflectivity and simulation at room temperature of a very similar microcavity used in experiments. The blue line is the actual reflectivity spectrum while the red lines are the result of the transfer matrix simulation. Right: Electric field intensity simulation of a cavity mode on the microcavity structure. The indices of refraction are superimposed with the field amplitude to illustrate the enhancement of the field at the quantum wells. Note that the QW's are placed at the antinoes of the confined mode.

of the different layers (GaAs, AlGaAs, AlAs) as function of incident wavelength and temperature. Ref. [50] and Ref. [51] were used for the simulations involved in this dissertation. For the propagation of light close to the exciton resonance E_0, as with the case of each QW, we consider the model derived from classical linear dispersion theory

$$\epsilon = \epsilon_b + \frac{4\pi\beta_{\mathrm{QW}} E_0^2}{E_0^2 - E^2 - i\gamma E} \tag{2.20}$$

where ϵ_b is the background dielectric constant, $4\pi\beta_{\mathrm{QW}}$ is the oscillator strength or exciton polarizability, E_0 is the zero-momentum exciton energy, γ is the damping term or exciton broadening parameter and E is the energy of the incident light. The effective oscillator strength of the whole cavity $4\pi\beta$ is a result of the confinement factor which takes into account the overlap between the QW's and the light field and the penetration of the field into the DBRs[35]

$$4\pi\beta = 4\pi\beta_{\mathrm{QW}}\Gamma. \tag{2.21}$$

The confinement factor is given by

$$\Gamma \approx \frac{2N_{\mathrm{QW}}d}{z_{\mathrm{eff}}L_c}, \tag{2.22}$$

where N_{QW} is the number of QWs, d is the thickness of each, and z_{eff} is the effective order of the cavity. The penetration of the field in the mirrors is accounted for by the effective order of the cavity[52] is given by

$$z_{\mathrm{eff}} = z + z_0 \tag{2.23}$$

where z is the number of half-wavelengths contained in the cavity. The component of the field penetrating into the mirror gives a contribution $z_0 = n_{\mathrm{low}}/(n_{\mathrm{high}} - n_{\mathrm{low}})$ where $n_{high}(n_{low})$ are the high(low) index of refraction of the DBR. The observed Rabi splitting is given by [3]

$$\Omega = \sqrt{4\pi\beta E_0^2/\epsilon_b} = \sqrt{4\pi\beta_{\mathrm{QW}}\Gamma E_0^2/\epsilon_\infty}. \tag{2.24}$$

Figure 2.6 shows the actual and simulated reflectivity of the stressed microcavity. The parameters used in simulations are shown in Table 2.1. The bare exciton energy as a function of position (X Axis) that goes in the simulation is solved from the actual UP and LP energies of the actual reflectivity. The theoretical caculation of the shift with stress of the bare exciton energy across the sample will be presented in Chap. 4.

2.4 SAMPLE DESIGN AND CHARACTERISTICS

The sample studied consists of three sets of four GaAs/AlAs quantum wells embedded in a AlAs/AlGaAs microcavity (see Appendix C). Each set of quantum wells is placed at an antinode of the confined photon mode, similar to the structure used in previous work[8]. As long as they are located in the antinodes of the cavity photon, more quantum wells is advantageous because it increases the coupling and the phase-space filling density (refer to Chap. 3.4). The microcavity is purposely designed in such a way that it is negatively detuned in the center of the 2-inch diameter wafer, with $\delta \approx -40$ meV ($\delta = E_{\mathrm{ph}} - E_{\mathrm{ex}}$), so that a sample covers a wide range of detuning δ including a resonant region $\delta = 0$ and a region of positive detuning.

[3] See Appendix B for derivation

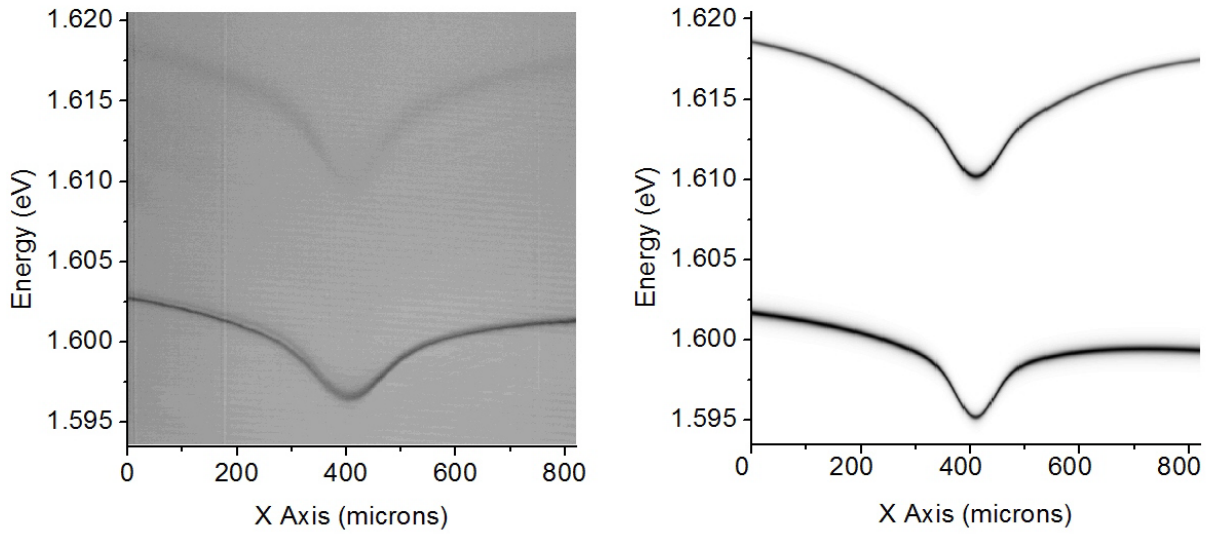

Figure 2.6: Left: Stressed sample showing the anti-crossing of the upper and lower polariton. The Rabi splitting is measured to be 13 meV . Right: Transfer matrix simulations for the same conditions using the measured the QW oscillator strength $4\pi\beta_{\mathrm{QW}}$ as parameter which can be derived from the measured Rabi splitting.

Figure 2.7 shows the reflectivity spectrum as a function of position on the sample and the shift in energy due to the variation layer thicknesses. The cavity length changes due to the thinning of the layer thickness by more than 10% toward the edge of the wafer, which is part of the growth process. The variation of the layer thicknesses can be quantified by comparing the reflectivity data with a transfer matrix simulation (as with Fig. 2.5) using a constant percent change in every layer thickness as fit parameter for each new position in the sample. As the layer thickness changes, the energy of the bare cavity photons and bare excitons shift. The anticrossing of the upper and lower polariton branches when the bare cavity photon and bare exciton reaches resonances can be clearly seen. The strong coupling regime corresponds to the area where the upper and lower polariton branches anticrosses. In this region, one can no longer define the exciton or the cavity photon, as the proper new eigenstates are mixed states of these, which we called the upper and lower polariton states. We can, of course, deduce where the bare exciton and cavity photon energies would be if we turned off the coupling. We can do this in two ways. One way is to fit the uncoupled

Table 2.1: Parameters used for simulations shown in Fig. 2.6

Exciton Energy E_0	1.6123 eV
Exciton Broadening γ	0.2 meV
QW oscillator strength $4\pi\beta_{QW}$	6.25×10^{-3}
$\frac{3}{3}\lambda$-cavity length L_c	130 nm
Number of quantum wells N_{QW}	12
Thickness of the QW	7 nm
Effective order of the cavity $m_{\mathrm{eff}} = m + m_0$	$3 + 6.2435$
Cavity dielectric constant ϵ_∞	12.98

regions (both far end of the region of strong coupling) with a continuous analytic function of the bare exciton and photon energy. Another way is to solve for the bare exciton and cavity photon energy by inverting the polariton equation derived from the two coupled oscillator(refer to Eq. (2.6).

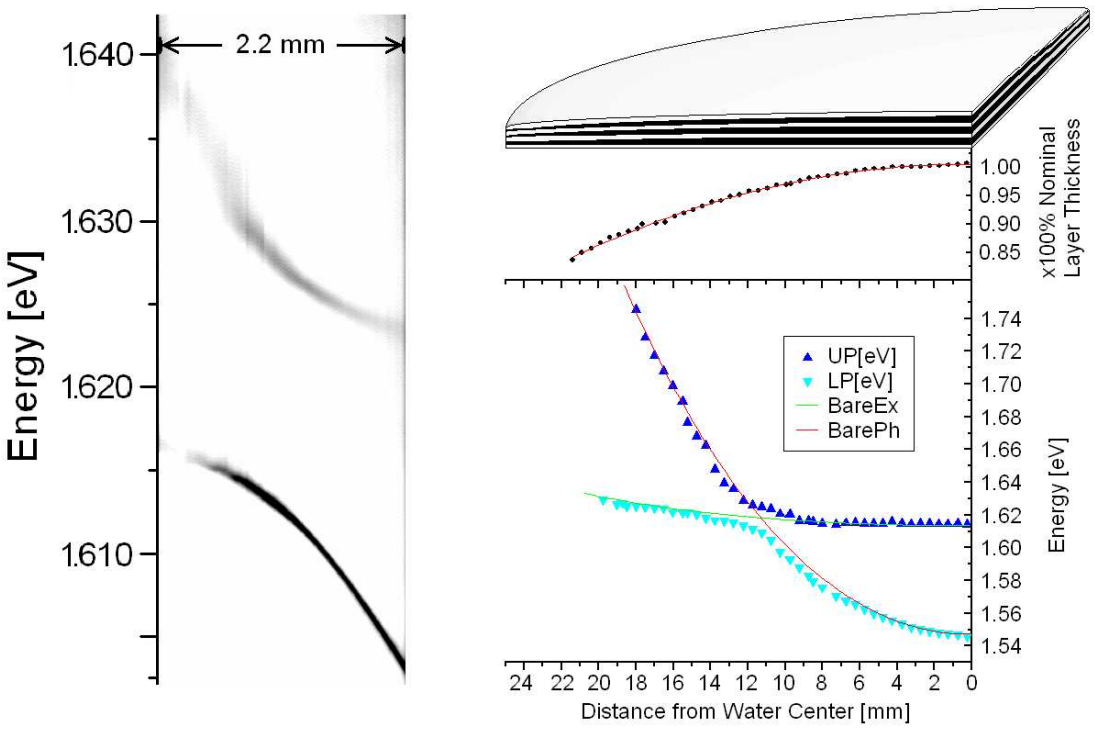

Figure 2.7: Left: Reflectivity spectrum as a function of position, around the resonant region of the sample, for the zero stress case. Right: The polariton energy shifts as the cavity length shifts, due to the thinning of the layers away from the center of the wafer. The bare exciton and cavity photon energies are deduced from the data by fitting the points far away from resonance, which can be safely be assumed as uncoupled, using the analytical form of the exciton and photon energy as a function of well thickness and cavity length respectively.

3.0 MACROSCOPIC QUANTUM PHENOMENA IN POLARITON SYSTEMS

Quantum mechanics has provided us with an understanding of some of the most fascinating aspects of nature. The quantum phenomena we are most familiar with are often in the realm of atomic and subatomic scale. Nevertheless, some of the most interesting quantum effects also happen in bulk properties of matter on a much larger scale. One type of macroscopic quantum phenomenon is Bose-Einstein condensation (BEC). BEC is a thermodynamic transition where particles equilibrate in the same lowest energy quantum state at a critical temperature T_c or critical density n_c. A highly ordered phase arises such that a macroscopic collection of these particles becomes dependent on a single wave function. Thermodynamic observables like heat capacity, viscosity, etc. changes suddenly. Coherence of the wavefunction is maintained over distances much longer than the particle separation. Since all the particles behave in the same manner, quantum nature of an individual particle is spectacularly amplified.

3.1 BEC IN MICROCAVITY POLARITONS

The BEC of non-interacting ideal gas in three dimensions have been presented in previous dissertations (e.g. [38]) and in standard statistical mechanics, solid state, and quantum mechanics textbooks (e.g. [53]). It suffices to say that in the continuum limit we have an upper bound in the total number of excited states or accessible states. Additional particles above the critical density occupies the lowest energy state. The critical density n_c can then

be written simply in this form

$$n_c = \frac{2.612}{\lambda_{dB}^3} \tag{3.1}$$

with

$$\lambda_{dB} = \left(\frac{2\pi\hbar^2}{mk_BT}\right)^{1/2}. \tag{3.2}$$

Because of its lighter mass, $m \approx 10^{-4}\, m_e$, polaritons are expected to condense at a lower density and a higher temperature than their atomic counterparts. Note that at liquid helium temperature ($T = 4\ K$), the thermal de Broglie wavelength is $\lambda_{dB} \approx 4\ \mu$m for polaritons. This means that Bose coherent effects will ocur when the distance between particles $r_s \approx 4\ \mu$m, which corresponds to density $n \approx 1/(4\ \mu\text{m})^2 \approx 10^7\ \text{cm}^{-2}$, which is easily obtainable by standard laser pumping methods. With a lower critical density, the formation of an electron-hole plasma which hinders condensation is avoided (see Chap. 3.4).

However, the MCP we study is not in a three-dimensional system. Confinement of photons in the microcavity and excitons in the quantum wells makes it essentially a two-dimensional system. In two dimensions, the critical density of a Bose-Einstein condensate diverges at any temperature greater than 0 K. For a two-dimensional Bose gas the density of states $g(\epsilon)$ is a constant:

$$g(\epsilon) = \frac{m}{2\pi\hbar^2}, \tag{3.3}$$

which implies

$$n = \int_0^\infty \frac{1}{e^{\beta(\epsilon-\mu)} - 1} g(\epsilon) d\epsilon = \frac{m}{2\pi\hbar^2} \int_0^\infty \frac{1}{e^{\beta(\epsilon-\mu)} - 1} d\epsilon. \tag{3.4}$$

Doing the integral gives

$$\begin{aligned} n &= -\frac{mk_BT}{2\pi\hbar^2} \ln(1 - e^{\beta\mu}) \\ \mu &= k_BT \ln\left(1 - e^{-2\pi\hbar^2 n/mk_BT}\right) \end{aligned} \tag{3.5}$$

Therefore, at finite temperatures, we see, from Eq. 3.5, that μ never goes to zero. In two dimensions, there is no upper bound in the density of excited states. Hence, there is no true Bose condensate. In fact, spontaneous symmetry breaking is prohibited in 2D.

Nevertheless, a transition to a superfluid state can take place as predicted by Berezinskii[54] and independently by Kosterlitz and Thouless[55]. This will be discussed in the next section.

The situation changes dramatically if we consider potential traps or confinement in a region of finite size[56, 57]. If we create a harmonic trap for a two-dimensional system, the density of states becomes proportional to energy, creating an upper bound in the density of excited states. This allows a finize-size BEC to occur. This is the main motivation for applying traps in our system. For a two-dimensional system with a harmonic trap $V(r) = \alpha r^2$, the density of states $g(\epsilon)$ is given by

$$g(\epsilon) = \frac{2m\pi^2}{h^2\alpha}\epsilon \tag{3.6}$$

where m is the mass of the ideal non-interacting boson and h is Planck's constant (For more details of the derivation of density of states in a d-dimensional power law trap $V(r) = \alpha r^n$, see Appendix D). In our experiments, typical quantum level spacing is orders of magnitude smaller than the thermal energy (see Chapter 4). We can therefore treat the possible k's a continuum. Hence,

$$N = \frac{2m\pi^2}{h^2\alpha}\int_0^\infty \frac{\epsilon}{e^{\beta(\epsilon-\mu)}-1}d\epsilon. \tag{3.7}$$

As μ approaches zero, the integral can be solved easily, and equals a constant $\pi^2/6$. Therefore, the critical number of particles N_c for two dimensions in a harmonic trap is given by

$$N_c = \frac{m\pi^4}{3h^2\alpha}(k_B T_c)^2. \tag{3.8}$$

For experimental conditions, where $\alpha = 75$ eV/cm^2, $m = 7 \times 10^{-5}\, m_0$, and $T = 16$ K, the critical number of polaritons $N_c = 1,920$.

For polaritons in a trapped potential, the condensate density $n_0(r) = n - n'(r)$ is estimated to be[58, 59]

$$n'(r) = -\frac{mk_BT}{2\pi\hbar^2}\log\left(1 - \exp\left[-\frac{1}{k_BT}\sqrt{\left(\frac{1}{2}\gamma_{\text{eff}}r^2 + 2U_{\text{eff}}^{(0)}n - \mu\right)^2 - |U_{\text{eff}}^{(0)}|^2 n_0^2}\right]\right) \tag{3.9}$$

where n is the total polariton density, γ_{eff} is the effective spring constant of the bare excitons, $\mu = 2U_{\text{eff}}^{(0)}n - U_{\text{eff}}^{(0)}n_0$ is the chemical potential, and $U_{\text{eff}}^{(0)}$ is the effective polariton-polariton

repulsion potential. Using parameters from our results [37] and Eq. (3.9), the condensate size is expected to have a size of 25 μm FWHM [59]. The number of condensate particles is estimated to be $\sim 10^4$, which is an order of magnitude higher than the ideal case, Eq. (3.8), using the same parameters from our experiments, Refs. [37, 59].

It is important to realize that the statistical description of BEC invokes the thermodnamic limit, $N, V \to \infty$, such that possible k-states become continuous. Strictly speaking, there is no "true" BEC in any finite system. In the 3D case (e.g. Ref. [5, 6]), the total number of particles can be large, $\sim 10^6$, but still finite, making the critical transitions in T_c or n_c sharper than the 2D trapped case. But the 2D trapped case is fundamentally the same as 3D trapped case. Both can have macroscopic occupation of the ground state and both will not have a delta function occupation number in energy.

3.2 POLARITON SUPERFLUIDITY

The condensate is described as a macroscopic occupation of the zero-momentum state. We can further assign a wavefunction $\Psi_0(\mathbf{r})$ corresponding to that condensate such that $|\Psi_0(\mathbf{r})|^2 = n_0$ where n_0 is the density of particles. In terms of phase transition, $\Psi_0(\mathbf{r})$ is the order parameter which becomes non-zero below a critical temperature T_c. In general, the complex wave function can be written as

$$\Psi(\mathbf{r}) = \sqrt{n_0(\mathbf{r})} e^{i\theta(\mathbf{r})} \tag{3.10}$$

where $\theta(\mathbf{r})$ is the phase. It is important to note that the phase is undefined if there is no condensate $n_0 = 0$. The phase of a condensate can be any arbitrary constant. When that phase varies in space however, the condensate flows with zero viscosity. To show that this is true, recall the quantum mechanical formula for particle flow

$$\mathbf{J}_0 = \frac{\hbar}{2mi} \left[\Psi_0^*(\mathbf{r}) \nabla \Psi_0(\mathbf{r}) - \Psi_0(\mathbf{r}) \nabla \Psi_0^*(\mathbf{r})\right] \tag{3.11}$$

where $\mathbf{J}_0$ is the number of particles flowing per unit area per second. Substituting the wave function we get

$$\mathbf{J}_0 = \frac{\hbar}{m} n_0 \nabla\theta(\mathbf{r}) \tag{3.12}$$

or

$$\mathbf{v}_s = \frac{\hbar}{m} \nabla\theta(\mathbf{r}) \tag{3.13}$$

This relation defines the velocity for superfluid flow. It is necessary to distinguish between the condensate density n_0 and the superfluid density n_s. The superfluid density corresponds to the number of particles that participate in superflow $J_s = n_s v_s \propto n_s \nabla\theta$ which may not be the same as the condensate density. In superfluid helium for example, at $T = 0$, $n_s = n$ while $n_0 \approx 0.1n$.

In the previous paragraph, it is implied that BEC is not the same as superfluidity. Rightly so, since BEC is a macroscopic occuption of a groundstate which directly implies phase locking. Albeit, BEC is not sufficient for superfluidity, as shown, for example, by a condensate pinned by disorder[60]. Superfluidity, on the other hand, is a consequence of phase locking alone. The phase $\theta(\mathbf{r})$ of the wave function can be modeled by a system of two-dimensional unit vectors

$$\hat{\mathbf{n}}(\mathbf{r}) = (\cos\theta(\mathbf{r}), \sin\theta(\mathbf{r})) \tag{3.14}$$

at all points in space. This system of unit vectors can be described successfully by a theory in thermodynamic phase transitions called the XY-Model[61]. Properties of the superfluid helium has been predicted by the three-dimensional version of the XY-Model in perfect agreement with experiment.

In two dimensions, there is no true BEC. However, the XY-model predicts an existence of a superfluid transition called the Berezinskii-Kosterlitz-Thouless superfluid transition[54, 55, 62]. It is a sort of semi-macroscopic coherence where the correlation, which is the measure of phase locking, goes as an inverse power law

$$g(r) = \frac{1}{r^{\eta(T)}}, \quad \text{where} \quad \eta(\mathrm{T}) = \frac{\mathrm{T}}{4\mathrm{T_c}} \tag{3.15}$$

at $T < T_c$ instead of a constant for a true condensate and an exponential decay for a incoherent medium.

For polaritons in a harmonic trap in two dimensions, superfluids and condensates can coexist. A recent paper[59] showed that the normal fluid density in a 2D trap would be

$$n_n(r) = \frac{3.606 k_B^3 T^3}{\hbar^2 c_s^4[n_0(r)] M_{\text{eff}}} \tag{3.16}$$

where the condensate density is $n_0(r) = n - n'(r)$. The noncondensate polariton density $n'(r)$ is given in Eq. (3.9).

3.3 STABILITY OF THE CONDENSATE

What prevents a condensate of particles from breaking into several degenerate states or at least different states that are close in energy that they are practically identical in the thermodynamic limit? It turns out this phenomenon cannot be explained by invoking the ideal gas model. BEC is an effect of the particles' exchange interaction. The ideal non-interacting particle is in fact a pathological case. For example, a cavity photon has an effective mass (see Eq. (2.1)). Yet, by itself, photons do not condense even at high density. It turns out interaction is essential to stabilize the condensate.

Consider a more realistic case where a simple scalar interaction term is introduced to a system of structureless bosons.

$$V = \frac{1}{2} \sum_{p,q,k} V_k b_{p+k}^\dagger b_{q-k}^\dagger b_p b_q \tag{3.17}$$

The interaction describes a pair of bosons scattering from initial states $\mathbf{p}$ and $\mathbf{q}$ to final states $\mathbf{p}+\mathbf{k}$ and $\mathbf{p}-\mathbf{k}$, where $\mathbf{k}$ is the momentum transfered and $\mathbf{V_k}$ is the matrix element of that transition. As will be shown later, the interaction energy for particles all occupying the lowest state is extensively much lower than if the particles are split into states with the same energy.

Particles occupying the ground state can be described by

$$|\Psi_0\rangle = \frac{1}{\sqrt{N!}}(b_0^\dagger)^N|\text{vac}\rangle. \tag{3.18}$$

The corresponding interaction energy is given by [1]

$$E_0 = \frac{1}{2}V_0\langle\Psi_0|b_0^\dagger b_0^\dagger b_0 b_0|\Psi_0\rangle \approx \frac{1}{2}V_0N^2. \tag{3.19}$$

Now, let us consider the case where the particles are split between two states, $N = N_1 + N_2$, that are degenerate. The ground state can be written as

$$|\Psi_0\rangle = \frac{1}{\sqrt{N_1!N_2!}}(b_1^\dagger)^{N_1}(b_2^\dagger)^{N_2}|\text{vac}\rangle. \tag{3.20}$$

The fragmented interaction energy is given by

$$\begin{aligned}
E_{12} &= \frac{1}{2}V_0\langle\Psi_0|\sum_{p,q=1,2} b_p^\dagger b_q^\dagger b_p b_q|\Psi_0\rangle \\
&= \frac{1}{2}V_0\langle b_1^\dagger b_1^\dagger b_1 b_1 + b_2^\dagger b_2^\dagger b_2 b_2 + b_1^\dagger b_2^\dagger b_1 b_2 + b_2^\dagger b_1^\dagger b_2 b_1 + b_1^\dagger b_2^\dagger b_2 b_1 + b_2^\dagger b_1^\dagger b_1 b_2\rangle \\
&= \frac{1}{2}V_0[N_1(N_1-1) + N_2(N_2-1) + 4N_1N_2] \\
&\approx \frac{1}{2}V_0N^2 + V_0N_1N_2.
\end{aligned}$$

Comparing this with having the condensate in one single states shows that fragmenting the condensate has a huge energy penalty[2]. This is due to the exchange V_{1-2} terms in the interaction. This is one argument to explain the stability of a condensate of structureless bosons. The treatment of composite bosons such as polaritons are much more complicated but the basic physics is the same. Instead of a constant scattering potential V_0, the formalism involves an effective scattering matrix to consider additional direct and exchange terms between the individual components (fermions). For composite bosons, the reader is advised to look up a recent paper by Combescot and Snoke[63].

[1] Since we are talking about macroscopic occupation of the ground state, $N \pm 1 \approx N$.

[2] It is necessary that V_0 is be positive corresponding to a repulsive interaction or else the particles would spontaneously collapse.

3.4 PHASE-SPACE FILLING AND TRANSITION TO WEAK COUPLING

Atomic physicists often think of BEC transition in terms of phase transition across a critical temperature T_c. One can equally think of achieving BEC across a critical density n_c at constant temperature T (refer to illustration in Fig. 1.1). This is what we do in our experiments. The density of polaritons is increased by increasing the carrier population, in the electron-hole continuuum, with the pump laser intensity. The temperature is fixed by the balance of excess energy from input and cooling of the cryogenic bath. That temperature is difficult to measure experimentally but the bath temperature of 4 K is maintained (see Chap. 5 for experimental details). The characteristic polariton temperature is deduced by fitting the polariton occupancy with a Maxwell-Boltzmann distribution (e.g. Fig. 6.5).

In condensed matter systems as well as atomic systems, there are limits to which you can increase density. One such limit is the the density n when the particle spacing becomes comparable to particle size a_{bohr}, i.e. $n \approx 1/a_{bohr}^d$ where d is the dimension of the system. In this limit, the particles start seeing each fermionic contituents rather than as individual bosons[64], an effect known as phase-space filling. At this point, the carriers can be treated as a conducting plasma. The carriers are frozen by the Pauli exclusion principle leading to a charateristic Fermi level [65, 53]. Moreover, the system also becomes transparent as the electrons can no longer be excited to states below that Fermi level. This results in a renormalization of the index of refraction inside the cavity [66].

However, we do not have to got that far, for there is a thermodynamic insulator-conductor transition[65, 53, 67] with a critical density that is typically an order of magnitude lower than the phase-filling density. This temperature dependent transition is sometimes called Mott transition or ionization catastrophe[67]. This transition is due to the screening of excitons by free carriers, reducing its binding energy thus ionizing more carriers leading to further ionization. In three-dimensional systems, the critical density n for this transition is approximated by [65]

$$n = \left(\frac{\epsilon k_B T}{a^2 e^2}\right)^2 \frac{\mathrm{e}^{Ry/k_B T}}{n_Q} \tag{3.21}$$

where a is the Bohr radius of the bound exciton, Ry is the hydrogenic Rydberg, and n_Q is the effective density of state factors of the electrons, holes, and excitons.

The effects described above must be avoided if one wants to remain in the strong coupling regime (if one wants to keep the polaritons). The insulator-conductor transition is basically a bleaching of the oscillator strength because it destroys the population of oscillators N_{osc} (excitons). One can gauge the strength of coupling from the Rabi splitting Ω of the UP and LP, where $\Omega \propto \sqrt{f} \propto \sqrt{N_{\text{osc}}}$. As the oscillator strength is bleached, the UP-LP gap closes, observed experimentally as the blue shift of the LP and red shift of the UP, indicating a transition to weak coupling. In order to avoid this, multiple QWs are placed inside the microcavity so that the density of excitons per QW remains below the Mott transition density[68] even if the total density goes above the critical density for BEC. In addition, more quantum wells means more oscillators, which means the coupling strength also increases[69]. However, one cannot insert an indefinite number of QWs in the microcavity. Other than running into technological limitations, the quantum wells cannot all be at placed at the maximum photon field antinode. Hence, the Rabi splitting grows much more slowly than square root of the number of quantum wells. In the design of our microcavity sample, a set of four QWs are placed in each of the three antinodes in the cavity, for a total of 12 QWs (see Appendix C). This effectively gives us a Rabi splitting of 15 meV.

3.5 POLARITON LASER

The particular properties of microcavity polaritons spurred many experiments and papers searching for BEC effects [8, 9, 10, 14, 15, 16, 18, 17, 12, 13, 70, 71, 72]. The observation of bosonic behavior and stimulated scattering[15] in MCPs have inspired speculations of creating new opto-electronic devices, namely the "polariton laser". The concept of the polariton laser takes advantage of pumping strongly-coupled light and excitons in the microcavity. The polaritons created then relax, presumably condensing in the ground state, emitting coherent, monochromatic light. Polariton lasing is polariton BEC which can also be called "lasing in strong coupling". This new generation of lasers does not require population inversion to take

place and can have very low thresholds (e.g. [73]).

In conventional atomic BEC, the particle lifetime is much longer than the time it takes to establish equilibrium with itself and with its surroundings. This means that thermal equilibrium to has set in as the condensate is formed. The temperature is well defined and is equal to the surrounding temperature. Thermal equilibrium in microcavity polaritons means exactly the same thing, but only that we take the surrounding temperature to mean the lattice temperature not the bath temperature. On the opposite end of the scale, there is the non-equilibrium condition where the polariton population decays, emitting photons that leak out of the cavity, before equilibration with itself and the lattice takes place. In that case, temperature of polaritons cannot be defined. The regime in between is called quasi-equilibrium of polaritons, where, though the lifetime may not be long enough to establish thermal equilibrium with the lattice, the particles live long enough to equilibrate with each other. Here, the polariton temperature can be defined and is expected to be greater than the lattice temperature.

Because of the short lifetime of the photonic component of MCPs, the polariton lifetime is not necessarily long enough for the polaritons even to come to a complete quasiequilibrium. However, the low-energy range polariton states may have a definable temperature[38]. This process is often called non-equilibrium condensation or dynamic condensation of polaritons. Formation of the non-equilibrium polariton condensate is possible because of bosonic stimulated scattering[29, 30, 31, 8, 9, 43, 44, 45]. Stimulated scattering is a basic property of Bose-Einstein statistics which implies that the scattering rate to a k-state is proportional to $(1 + N_k)$, where N_k is the population of that state. The stimulated scattering effect is a sure sign that quantum degeneracy is achieved in the system, since the criterion for this to happen is that $N_0 \geq 1$ where N_0 is the lowest energy population. Once a condensate is formed in the ground state, coherent light emission can be observed. This is the principle behind polariton lasers. Population inversion is not required.

There is some confusion about the term "polariton laser". As will be discused in Chapter 6.5, standard lasing is sharply distinguishable from the polariton condensate, even though both emit coherent light. Some people prefer to reserve the word "condensate" only for a true equilibrium or quasiequilibrium state, and thus assign the term "polariton laser" to the

state we are calling a non-equilibrium condensate. The term "laser", however, stands for stimulated emission of radiation, and in the polariton condensate, there is no stimulated emission of the radiation, only stimulated scattering of the polaritons.

Experiments [8, 9, 10] have shown that dynamic polariton condensation at low polariton densities, manifested by MCP lasing, can result from nearly resonant excitation, just above the bottleneck region. Polaritons were injected by a pulsed laser pumping at an energy resonant with the LP but with large incident wavenumber $k_{||}$, so that macroscopic occupation at the lowest state is not coherently driven by optical parametric amplification or four-wave mixing effect. The polaritons relax mainly by phonon emission at large $k_{||}$. Around the "bottleneck", relaxation is achieved by scattering of two polaritons with each other, one towards a lower energy state and the other towards the higher energy state such that momentum is also conserved. Both conventional and polariton lasers show nonlinear increase in emission intensity at $k_{||} = 0$. The polariton laser, on the other hand, has a lower threshold than the photon laser by about two orders of magnitude. These groups [8, 9, 10] also claimed that the carrier density was orders of magnitude smaller than the Mott transition density, the density limit where polaritons no longer exist. The onset of the nonlinear increase in the emission intensity indicates bosonic final state ($k_{||} \approx 0$) stimulated scattering. As explained in the Chap. 2, measuring various aspects of the emission provides the characteristics of the condensate since emitted photons have a one to one correspondence with the internal polariton states. The same group [8, 9, 10] has further shown that beyond the polariton lasing threshold, the population at $k_{||} > 0$ near the groundstate follows a Bose-Einstein distribution and a non-equilibrium condensation at $k_{||} \approx 0$.

The transition to polariton lasing in these experiments comes with a nonlinear increase of the emission intensity at $k_{||} = 0$, acceleration of emission buildup and decay, spatial concentration of LP, slow spatial expansion of LP, and increase in the degree of circular polarization of emitted photons. Numerical calculations [11] also confirm that the polariton lasing is a signature of non-equilibrium bosonic condensation. A good qualitative agreement is seen when comparing polariton "lasing" intensity $I(t)$ from previously shown experimental results with the theoretical condensate kinetics $n_0(t)$ ($I(t)$ is proportional to $n_0(t)$). Theory shows that for nearly resonant excitation, LP-LP scattering is reponsible for the low threshold

lasing effect where it plays a crucial role in cooling the hot excitons into the lowest energy state.

Our experiments with a trap and nonresonant excitation are complementary to earlier experiments. It is important to note that the recent results described[8, 9, 10, 11] and the results that will be presented in this thesis are in a non-equilibrium condition, where the polariton population decays before long-range order is achieved. Hence, "true" BEC is not yet formed. Nevertheless, coherence is built up due to the boson statistics.

3.6 SIGNATURES OF BEC

Although theory is well established and there have been many claims, evidence presented for condensation in electronic composite-boson systems has often been hard to distinguish from photon lasing. To have a reasonable claim of condensation [74], one has to demonstrate that the critical density as a function of temperature, the spatial distribution of the condensate in a trap, the excitation spectrum, and the particle density as function of k-wavevector fit well with theory. Also, the spontaneous macroscopic coherence of the system, which is what BEC is all about, has to be demonstrated. Effects such as standard lasing and driven coherence by resonant pumping have been misconstrued to be signs of condensation. It is particularly important to prove that the spectral narrowing observed is not the result of photon lasing. Also, the ballistic expansion of particles may only be due to the "blowing" of hot phonons created during pumping and not due to superfluidity. Such pitfalls have to be avoided if the clear signature of BEC is to be shown.

Careful attention must be given to the subtle differences between photon lasing and BEC transition. In a recent paper by J. Bloch et. al. [66], it was shown that a photon lasing may easily be misinterpreted as BEC transition. Previously, groups claimed to have observed BEC transistion on the grounds that the emission line corresponds to an energy lower than the bare cavity photon and close to the lower polariton energy. Naively, this meant that it remained in the strong coupling regime and that the "lasing" effect was due to polaritons and not photons. Bloch, however, argued that this is also what happens in photon lasing

since above threshold the energy is actually red-shifted as a result of the renormalization of the dielectric constants. Bloch suggested that an unambiguous proof of BEC therefore would be to see both transitions as one goes through a range of temperature or density. This means two thresholds must be observed, one for the BEC transition and a higher threshold for the photon lasing transition. In our trapped configuration, this two threshold phenomenon can be observed, as will be presented in the experimental results in Chap. 6.5. It has also recently been observed by Bloch's group in micropillar experiments with very high-Q cavities[75].

4.0 TRAPPING POLARITONS

4.1 TUNING TO RESONANCE AND TRAPPING

Potential traps in a semiconductor microcavity can be created by applying electric field, varying well width[76], varying cavity length, varying mirror reflectivity, or subjecting it to stress. Using electric field to tune the resonance[70] has the drawback that the oscillator strength of the exciton changes strongly with electric field. Varying well-widths while growing a sample is not easy to control, making it difficult to ensure a harmonic potential profile. Also, in standard growth processes, it is unavoidable to form a gradient of the layer thicknesses across the center to the edge of the wafer. As a result, only a tiny region of a wafer is in the strong coupling regime.

In our experiments, we used stress to tune the quantum wells. The energy of the excitons shift in energy with strain on the quantum wells. The energy shifts as a function of stresses is given by the Pikus-Bir deformation Hamiltonian[77]:

$$H_{PB} = a(\epsilon_{xx} + \epsilon_{yy} + \epsilon_{zz}) + b[(J_x^2 - J^2/3)\epsilon_{xx} + c.p.] + \frac{2d}{\sqrt{3}}\left[\frac{1}{2}(J_xJ_y + J_yJ_x)\epsilon_{xy} + c.p.\right] \quad (4.1)$$

where a, b, and d are deformation potentials, ϵ_{ij}'s are stress-tensor components, J's are angular momentum operators acting on the spin states of the valence band ($m = 3/2$, $1/2$, $-1/2$, and $-3/2$), and $c.p.$'s correspond to cyclic permutations with respect to x, y, z. Relevant material properties, e.g. deformation potentials and elastic constants, used in our simulations (refer to Appendix E, F, and G) are found in Refs. [78, 49, 79]. For stress along the growth direction (z-axis), $E_{PB} = 3a\epsilon_{hydro} - 3b_{shear}$, where $\epsilon_{hydro} = \frac{1}{3}(\epsilon_{xx} + \epsilon_{yy} + \epsilon_{zz})$, and $\epsilon_{shear} = (\epsilon_{zz} - \frac{1}{2}\epsilon_{xx} - \frac{1}{2}\epsilon_{yy})$. The shear term changes the symmetry of the crystal which leads to the splitting of the bands. Shear stress can be used in microcavities to

produce a potential minimum. The hydrostatic strain does not change the symmetry of the crystal, but if a hydrostatic expansion is in effect, it can also contribute in creating a potential minimum. This can happen given the right geometry such that application of stress leads to a hydrostatic expansion. Fig. 4.1 shows one such geometry which has been developed previously in our group [80]. Stress allows one to tune quantum wells into

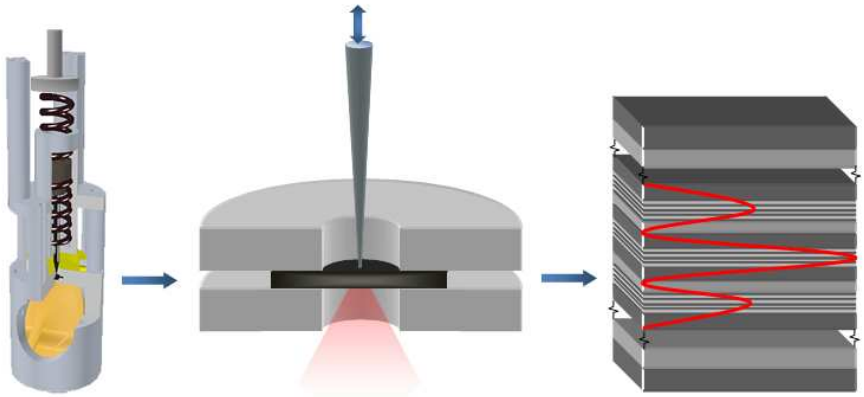

Figure 4.1: Geometry of the stress technique and the structure of the microcavity

resonance with the cavity photon. Figure 4.2 illustrates how the upper and lower polariton dispersion, Eq. (2.6), when the bare exciton energy is shifted through the cavity resonance. A more detailed presentation of how the Pikus-Bir deformation and other relevant terms (e.g. exchange) affect the bands, including computational methods used in our simulations, will be presented in Appendix E. Fits from simulations of exciton band shifts applied to cavity polartons will be discussed further in Chap. 8.

The method described above gives us the freedom to use nearly any part of the wafer and to tune the exciton bands into the region of strong coupling. At the same time, when stressed, a potential minimum is created for the polaritons, which is a necessary requirement to observe true BEC as discussed in Chap. 3. The point of high stress becomes a confining point for carriers. In previous experiments[8], the polaritons were diffusing freely with energy shifts which depended on the local density[17].

Stress may also be varied to control the amount of coupling between the excitons and the cavity mode. Varying the amount of stress can make the polaritons more more photon-like

or more exciton-like, as shown in Figure 4.2. As discussed earlier, controlling the amount of coupling allows one to increase or decrease the lifetime of polaritons at will. Applying the

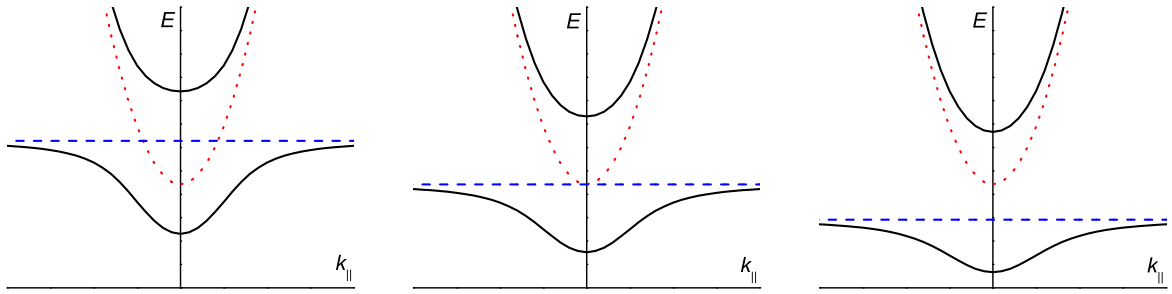

Figure 4.2: Different possible tunings with increasing stress. Left to Right: Negative, Zero, and Positive detunings. Upper and Lower Polariton (Black Solid), Bare Exciton (Blue Dashed), Bare Cavity (Red Dotted). Stress shifts the exciton state down while the cavity photon is essentially unchanged.

technique in practice is illustrated in Figure 4.1. The spring constant is inversely proportional to the thickness of the sample. The thinner the sample the deeper and smaller the trap is. While a deep and small profile is often desirable, there is a greater risk of breaking the sample during handling. In Chap. 7, results are generated from a sample with 40 μm thickness. The rest of the samples used in experiments have a 150 μm thickness . In Fig. 4.3, the sample is stressed until the bare exciton energy is as close to the microcavity resonance as possible. A force is applied on the back side of a 40 μm substrate with a rounded-tip pin with 50 μm or less tip radius. Figure 4.3 shows a typical profile of the the lower polariton potential well created by stress. Directly under the stressor, the lower polariton branch has an energy minimum which can be well fit by a harmonic potential [80, 37] $U = \frac{1}{2}\gamma r^2$ where r is the distance from the center of the trap and $\gamma = 150$ eV/cm^2. This corresponds to a quantum level spacing in the harmonic potential of $\hbar\omega_0 = 0.037\,\text{meV}$ where $\omega_0 = \sqrt{\gamma/m}$ is the natural frequency and m is the effective mass equal to $8 \times 10^{-5} m_e$. The continuum approximation for the polariton states in the trap is valid here since this level spacing is much less than $k_B T = 0.345\,\text{meV}$ at 4 K. Stress trapping allows theory to treat a quasi-equilibrium gas with a known confining potential. This method opens a variety of possibilities and promise in the area of microcavity research and BEC of polaritons.

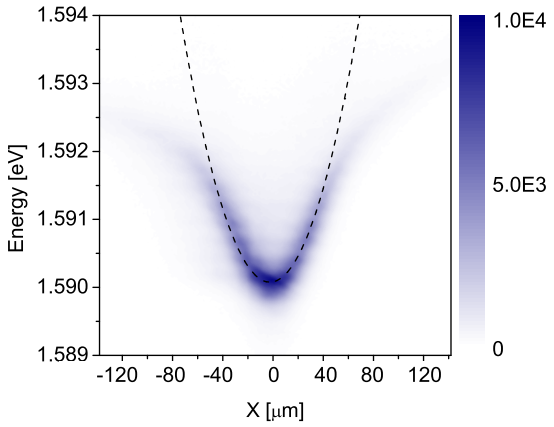

Figure 4.3: Profile of the stress well created by 1.5 N of force on the pin stressor. Sample excited with laser defocused laser (722 nm $\approx$ 1.72 eV, 2.3 mW Pump Power, $\sim$ 2 mm diameter) to view the whole stress well profile. Dashed line: Fit to a harmonic potential.

4.2 CHARACTERISTICS OF A MICROCAVITY WITH A STRESS TRAP

We have already achieved active tuning of the polariton resonance of QW excitons in a semiconductor microcavity using applied stress. Starting with a QW exciton energy higher than the cavity photon mode, we used stress to reduce the exciton energy and bring it into resonance with the photon mode. At the point of zero detuning, line narrowing and strong increase of the photoluminescence are seen. By the same means, we create an in-plane harmonic potential to trap the polaritons. In Chapter 7, we discuss drift of the polaritons into this trap.

4.2.1 Photoluminescence and Reflectivity

Figures 4.4 and 4.5 show photoluminescence and reflectivity data for a sequence of increasing stresses applied to this sample. The huge slope in energy of the lower polariton is due to the spatial variation of the cavity length across the sample (see discussion in Chap. 2.4). The pin stress point is chosen several millimeters to the right of the point of strongest coupling, where the exciton energy is ~ 20 meV higher than the photon energy. For the photoluminescence, a helium-neon laser source (633 nm) is used to excite the sample off-resonantly, well above the band gap, at $\theta = 12^\circ$ incidence, and defocused to a spot size of several millimeters to cover the entire region of observation. Photoluminescence emission collected normal to the

sample is directed to a spectrometer and captured with a Photometrics back-illuminated CCD camera. For the sample reflectivity, a collimated light beam (750 nm−1000 nm) is directed normal to the sample. The reflected light is also collected normal to the sample. A mirror placed in the same plane as the sample is used to normalize the sample reflectance. For all the experiments, the sample was maintained at the temperature of 4 K. At this low temperature, no photoluminescence is seen from the upper polariton, as the polaritons scatter to a lower energy state before recombination. Upper polariton emission for this sample starts to appear at about 40 K.

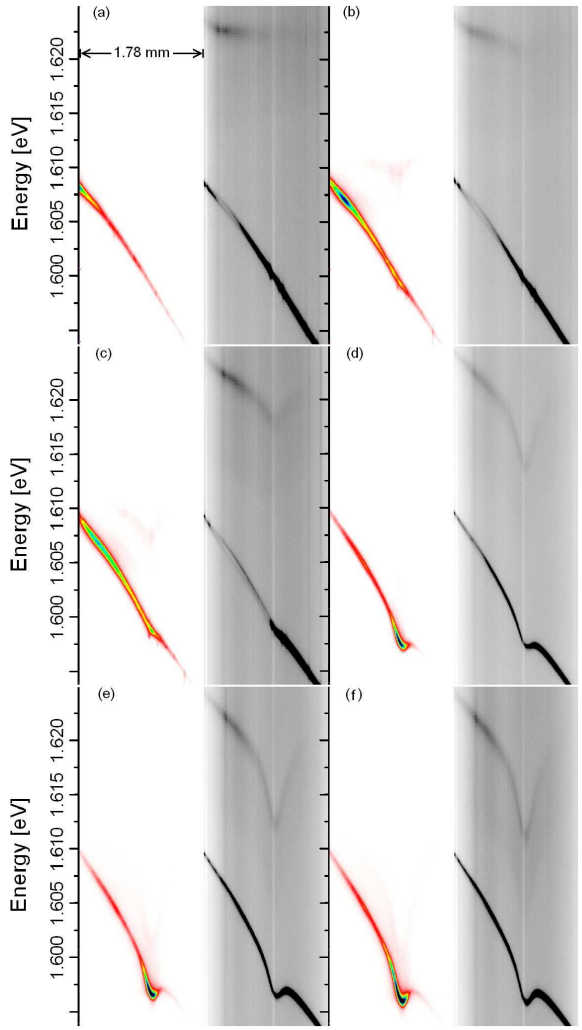

Figure 4.4: Left: Luminescence spectrum as a function of position on the sample, for various levels of force on the pin stressor, (a) unstressed, (b) 0.75 N, (c) 1.50 N, (d) 2.25N, (e) 2.63 N, (f) 2.85 N (white: minimum; black: maximum intensity). These images were created by illuminating the entire observed region (2.2 mm diameter) with a 5 mW HeNe laser. Right: The corresponding reflectivity (black: 0.0; white: 1.0). A harmonic potential is clearly seen in both upper and lower polariton branches.

In addition to the energy shift of the bands, a striking increase of the photoluminescence occurs, as seen in Figure 4.5. This is similar to the increase of photoluminescence at reso-

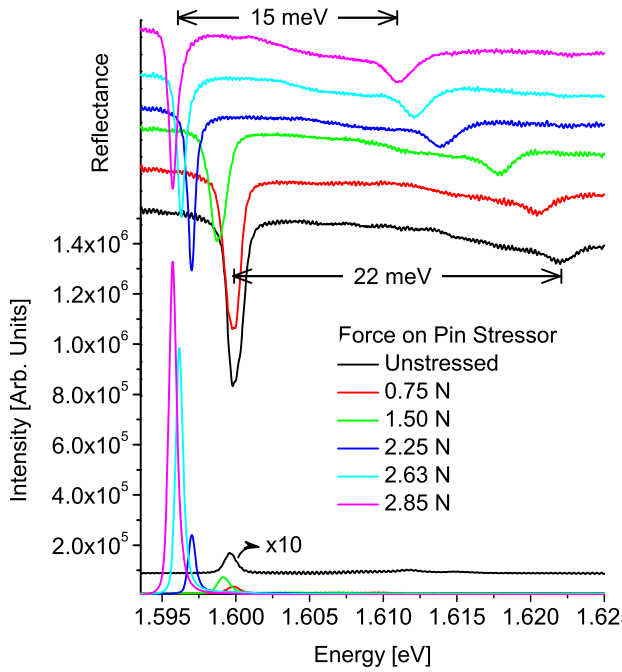

Figure 4.5: Top: Reflectivity at the bottom of the stress well, for a series of applied forces. Bottom: Photoluminescence emission of the lower polariton, taken with the HeNe excitation source (900 μW) focused (75 μm) at the bottom of the stress well.

nance seen by tuning of the resonance using a wedge of varying cavity thickness,[71] but the increase in the present case is dramatic, a factor of about 100. The increase of the total photoluminescence emitted from the front surface is consistent with an increase of the coupling constant at resonance[71]. Consistent with the strong coupling, one can see in Figure 4.5 the narrowing of the reflectivity spectra as the bare excitons and bare photon modes approach resonance[23] during stress tuning.

4.2.2 Drift

Since there is an energy gradient for the polaritons, one expects that they will undergo drift. Figure 4.6 shows spatially resolved photoluminescence when the laser is tightly focused and moved to one side of the potential minimum in the lower polariton branch. Some polaritons clearly live long enough to be observed over a distance of more than 100 μm, similar to what was seen in earlier drift experiments[72] where an energy gradient is created by a wedge of the cavity thickness. By determining the center of mass shift of the polariton luminescence from Fig. 4.6, we measure the drift length l_d to be 18 μm. From the measured drift length,

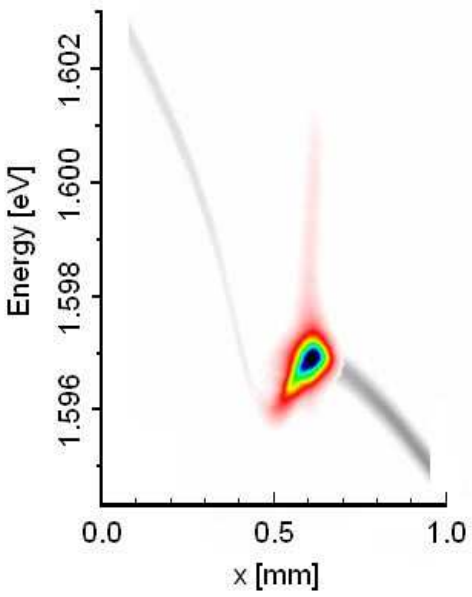

Figure 4.6: Spatially resolved photoluminescence for 2.85 N applied force (white: minimum, black: maximum intensity) with the laser focused (75 μm FWHM) and shifted 100 μm away from the center of the stress well. The photoluminescence is superposed on the reflectivity spectrum (gray) for the same conditions, to show the location of the well.

we can estimate the relevant scattering time constant τ_{sc}. From classical gas kinetics, the distance travelled by a particle due to a force is

$$l_d = \bar{v}_d \, \tau_0 \tag{4.2}$$

$$\text{where} \quad \bar{\text{v}}_\text{d} = \left(\frac{F}{m}\right) \tau_{sc}. \tag{4.3}$$

From Fig. 4.6, $F \approx \Delta U/\Delta x = 100$ meV/cm. Using a polariton lifetime $\tau_0 = 30$ ps and polariton mass $m = 7 \times 10^{-5}\, m_0$, Eq. (4.2) gives 24 ps for the relevant scattering time τ_{sc}. This, however, is a shallow trap. In our experiments, the typical spring constant of the trapping potential is around 150 eV/cm^2 (refer to Fig. 4.3). Drift length can be an order of magnitude longer, e.g. see Fig. 7.1.

From the deduced scattering time $\tau_{sc} = 24$ ps, we can also calculate the diffusion length l_D. In two dimensions, the diffusion length is written as

$$l_D = \sqrt{D\tau_0} \tag{4.4}$$

$$\text{where} \quad \text{D} = \bar{v}_D^2 \tau_{sc} = \frac{2k_B T}{m} \tau_{sc}. \tag{4.5}$$

At $T = 16$ K, the estimated diffusion length is equal to 70 μm. Normally, without a gradient in energy, polaritons diffuse away from the excitation spot. With the stress potential,

polaritons drift toward the center of the trap where they remain concentrated. The increase of the PL intensity seen in Figure 4.5 may be partly related to this feature. This is an important feature of our system, since we can generate the polaritons with a laser that is focused far from the center of the trap and watch them accumulate where there is no laser excitation. This technique removes the ambiguity in determining if the pump laser is causing the coherent effects. Later in Chap. 7, I shall present effects associated with spontaneous Bose coherence in the trap with the pump on the side.

4.2.3 Evaporative Cooling Effect

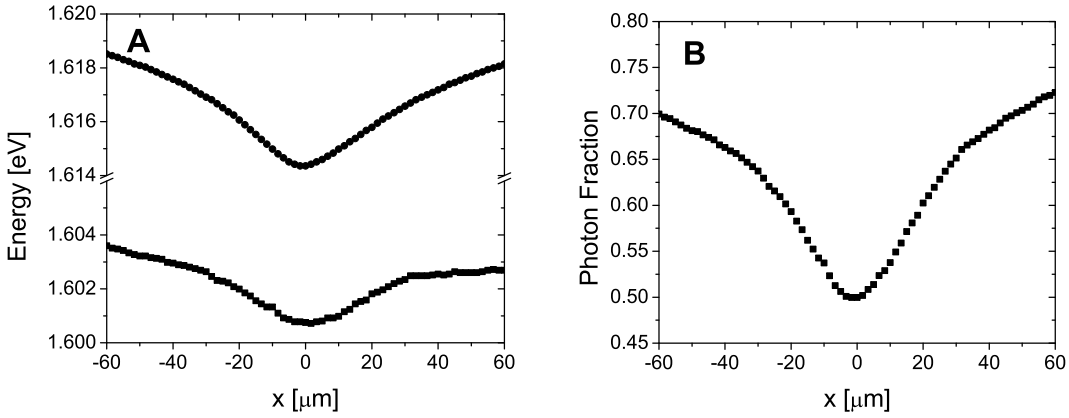

Figure 4.7: (**A**) Upper and lower polariton energies from photoluminescence and reflectivity spectra, when a force of 1.5 N on the pin stressor is applied to the sample. (**B**) Photon fraction of the lower polariton branch as a function of position in the trap, calculated from the polariton energies shown in (A) and the standard Hopfield coefficients, Eq. (2.5).

In real space, the exciton energy gets shifted down more where the center of the pin is. In the center of the trap, the cavity photon states and the exciton states are strongly coupled. Figure 4.7 shows that the polariton photon fraction increases as one moves away from the center. The lower polariton photon fraction is much smaller in the center of the well compared to the the regions away from it. This is good because at higher energies, far from the center, the polariton is actually more photon-like and does not stay long in the well. The mixing with the photon states leads to a decreased lifetime for high-energy states, effectively leaving the cooler polariton gas in the trap [81] similar to an evaporative cooling

effect in trapped atomic gases[82, 83]. Naturally, this effect would only work if the polaritons have long enough diffusion length to move through the whole trap. This is the case in our experiments, where in some cases the polaritons move more than 50 μm. In principle, this effect can be increased by the use of larger stress to positively detune the cavity so that the polaritons are more than 50% exciton like at the center and become completely photon-like away from the center. Unfortunately, no quantitative measurement of the lifetimes across the stress well has yet been made.

5.0 OPTICAL METHODS

5.1 IMAGING AND SPECTROSCOPIC TECHNIQUES

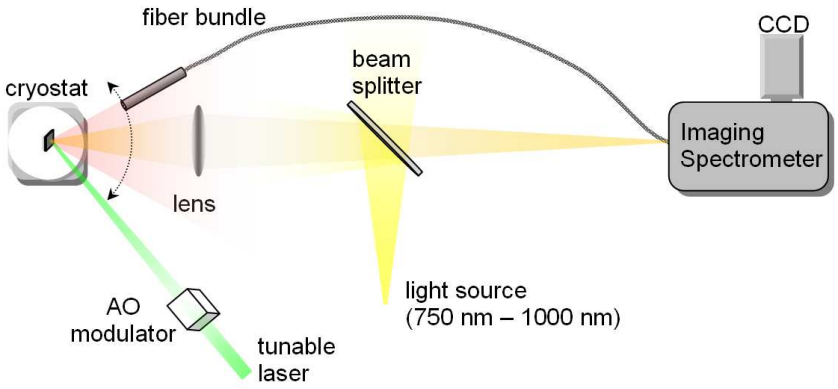

Figure 5.1: Experimental setup for spectral and spatial imaging

The nature of the microcavity samples having distinct properties (e.g. coupling) at different regions, and the technique of stressing requiring a precise knowledge of the stressor point, necessitated a permanent imaging set-up to be in place for all measurements. Imaging can be done normally using a lens to see the spatial profile of the polariton stress well. One may also look at the luminescence at different energies and wave vectors using a fiber optic. Signals are sent to a Photometrics Cascade512B back-illuminated CCD camera via an Acton SpectraPro2300i spectrometer. The setup for doing imaging and spectral measurements is shown on Figure 5.1. When taking images, the front slit is opened and the grating is rotated to its zeroth order so that it is simply working as a mirror. The imaging spectrometer has a grating with 1800 grooves/mm. The grating, in its zeroth order, is a poor mirror but our

samples emit more than enough light to compensate. The maximum spatial resolution of the imaging setup is 8 μm, measured using an EdmundOptics USAF SQ Negative resolution target. When taking spectral measurements, the spectrometer is set at its maximum spectral resolution of 0.06 nm with the front slit opened to 40 μm. The light source used for calibrating the spectral resolution was the diffuse reflection of a single-mode CW Ti-Sapphire laser at 771 nm which is around the spectral region of our polariton luminescence.

The sample is held inside a continuous helium-flow cryostat where it is kept at a low temperature, usually around 4 K. For lower temperatures, a liquid helium immersion cryostat maybe used. The sample may be excited using different sources. A continuous spectrum of light from 750-1000 nm is used to take the reflectivity of the sample. A tunable laser may be also used to pump the sample resonantly or non-resonantly at different angles. The measurements presented were made with a MIRA 900 Ti-Saphire laser from Coherent. Quasi-CW excitation was achieved using a NEOS acousto-optic modulator.

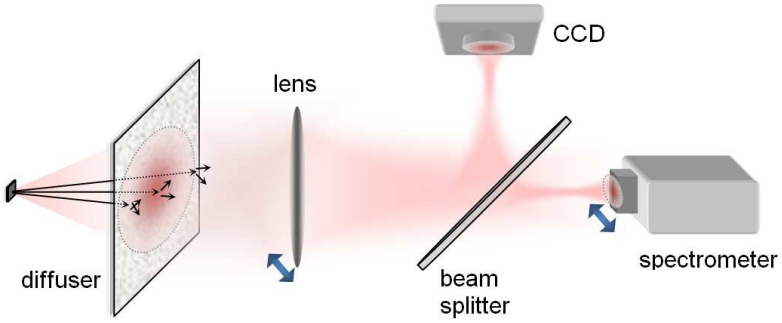

Figure 5.2: Experimental setup for angle-resolved measurements with a diffuser plate

Several techniques were developed for angle-resolved spectroscopy. One technique, utilized particularly for low signal or low pump intensities, was collecting light emission from the sample at different angles with a fiber bundle, as shown in Figure 5.1. For high-intensity signals, a convenient method of taking angle-resolved measurements is by placing a diffuser plate in front of the sample(see Fig. 5.2). The diffused light is then imaged on a spectrometer for quantitative analysis. The advantage of the diffuser is that it provides information simultaneously for both the horizontal and vertical components of the angle dependent PL

emission.

5.2 MEASURING COHERENCE WITH A MICHELSON INTERFEROMETER

In BEC, coherence of the wave-like state extends over the whole extent of the condensed entity. Coherence is measured by the correlation or the ability of two spatially and temporally separated points of the wave to interfere.

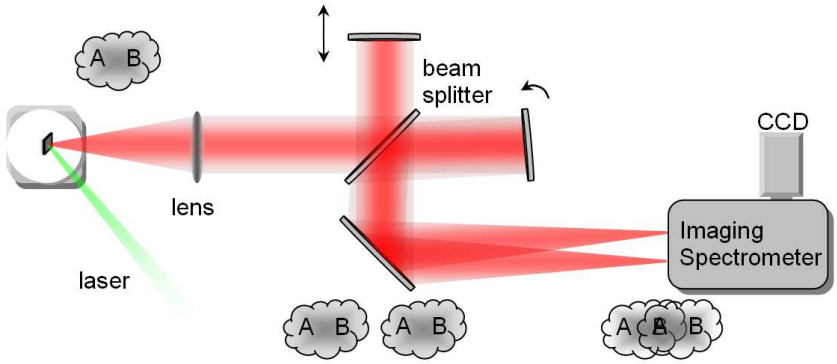

Figure 5.3: Michelson interferometer setup for first order coherence measurements

To measure the first-order coherence of the polariton condensate, a Michelson interferometer was setup (See Fig. 5.3). Using a beam splitter, two arms of the interferometer get identical copies of the polariton emission. Copies of the real image are projected onto a CCD camera. The images can be overlapped spatially by tilting the mirror for one path and temporally by changing the relative delays of the two paths. In effect, one end of the condensate (A) is correlated with another end (B). The classical first-order correlation can be written as

$$g^{(1)} = \frac{\langle E^*(\mathbf{x},t)E(\mathbf{x}',t')\rangle}{\langle E^*(\mathbf{x},t)\rangle\langle E(\mathbf{x}',t')\rangle} \tag{5.1}$$

where $E(\mathbf{x})$ is the electric field at $\mathbf{x}$. The degree of coherence is measured by this average correlation. Spatial coherence is oftentimes described in terms of visibility or the degree of contrast of the interference pattern. Visibility is defined as (e.g. Ref. [84])

$$V = \frac{\langle I(\mathbf{x},t)\rangle_{max} - \langle I(\mathbf{x},t)\rangle_{min}}{\langle I(\mathbf{x},t)\rangle_{max} + \langle I(\mathbf{x},t)\rangle_{min}} \tag{5.2}$$

The extremum intensity of the resulting overlapped signal can be written as

$$\langle I(\mathbf{x},t)\rangle_{max} = \langle I_1\rangle + \langle I_2\rangle + 2\sqrt{\langle I_1\rangle\langle I_2\rangle}|g_{12}^{(1)}| \tag{5.3}$$

and

$$\langle I(\mathbf{x},t)\rangle_{min} = \langle I_1\rangle + \langle I_2\rangle - 2\sqrt{\langle I_1\rangle\langle I_2\rangle}|g_{12}^{(1)}| \tag{5.4}$$

Hence,

$$V = \frac{2\sqrt{\langle I_1\rangle\langle I_2\rangle}}{\langle I_1\rangle + \langle I_2\rangle}|g_{12}^{(1)}| \tag{5.5}$$

We see that, if the intensity of the two fields are equal, the visibility of the interference pattern determines the first-order coherence. For infinitely coherent fields, the visibility $V = 1$, and $V = 0$ for a totally incoherent source.

6.0 EXPERIMENTAL RESULTS WITH CW LASER PUMPING

Our earliest experiments with microcavity polaritons began with continuous-wave (CW) laser pumping. It was a convenient setting to use being the default, stable operation of our laser system, and was a natural choice after using CW mode in characterizing stressed microcavities. With the CW mode, we can tune our laser for a wide range of energy (> 300 meV), necessary for pumping different frequencies of the polariton spectrum, while being able maintaining pump intensities an order of magnitude greater than pump power thresholds for BEC or photon lasing. More importantly it was necessary to be able see steady state properties of the polariton systems. Later on, we realized that CW lasing introduces local heating of the lattice leading to reduced drift, self-trapping and localization (see Chap. 6.3). Quasi-CW pumping was later used to avoid this situation (see Chap. 7). Then, again, the stability and power requirements needed to observe the two threshold behavior, attributed to BEC and photon lasing threshold (see Chap. 6.5), prompted us to return to CW experiments.

6.1 STRESS AND POLARIZATION POWER SERIES

One reason why it is difficult to distinguish between photon lasing and BEC is that the total carrier density in the case of the trapped polaritons in our experiments is not so much different from the total carrier density in the case of weak coupling. Fig. 6.1 shows the gain curves in our microcavity samples for four different conditions. Here the pump beam photon energy is tuned to the edge of the stop band and is focused to 65 μm. The $k_{\|} = 0$ emission is collected using a fiber and directed to the spectrometer and CCD camera. The blue inverted triangles show the gain curve for the case when stress is applied to create a spatial trap for

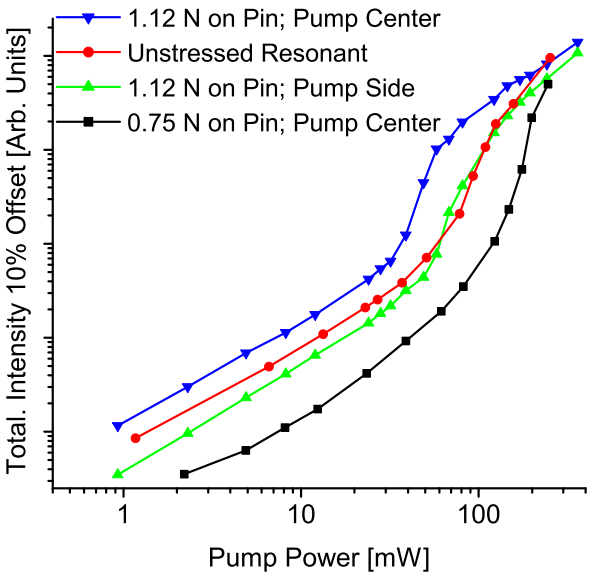

Figure 6.1: Photoluminescence intensity at $k_{\|} = 0$ versus pump power at different amounts of force on the pin stressors leading closer to a resonant state and at different positions of the sample. The plots are offset with respect to each other along the y-axis by 10%.

polaritons. At this stress point, the exciton and photon states are much closer to resonance than before it was stressed. When the stress is relieved (black squares) the threshold for the nonlinear gain, which corresponds to the onset of coherent behavior, increases dramatically. There are two reasons for this. One is the decreased trapping, and the second is the fact that releasing the stress takes the system farther from resonance, making the lower state even more photon-like. To truly see the effect of the trap, one can move the excitation spot to a region on the sample where the exciton and photon states are already in resonance without need for stress tuning. This case is shown as the red circles in Fig. 6.1. This case is comparable to the case of when the sample is excited on the side, far from the center of a stress trap shown as the green triangles in Fig. 6.1. Clearly, the trap is playing a role, since the threshold intensity for nonlinear gain with a stress trap close to resonance is less than for the case of resonance with no stress trap. The threshold decreases further with increasing stress. However, the difference in threshold is not more than a factor of three or four. Also, small changes in the laser focus spot size and the absorption of the pump laser due to the shift of the cavity reflectivity spectrum in the different cases of Fig. 6.1 lead to an uncertainty in the ratios of the densities by around 50%. The argument can be made that if the carrier densities are comparable, the physics cannot be much different. On first principles, of course, this need not be true. Many phase transitions occur which have

sensitive dependence on the total particle density. A Mott transition [65] from a system with mostly excitons to one dominated by free-carrier plasma has been shown can occur with a very sharply defined density[85]. Nevertheless, as will be shown in Chap. 6.5, we can directly test whether the behavior of the coherent emission is different in the trapped and untrapped case.

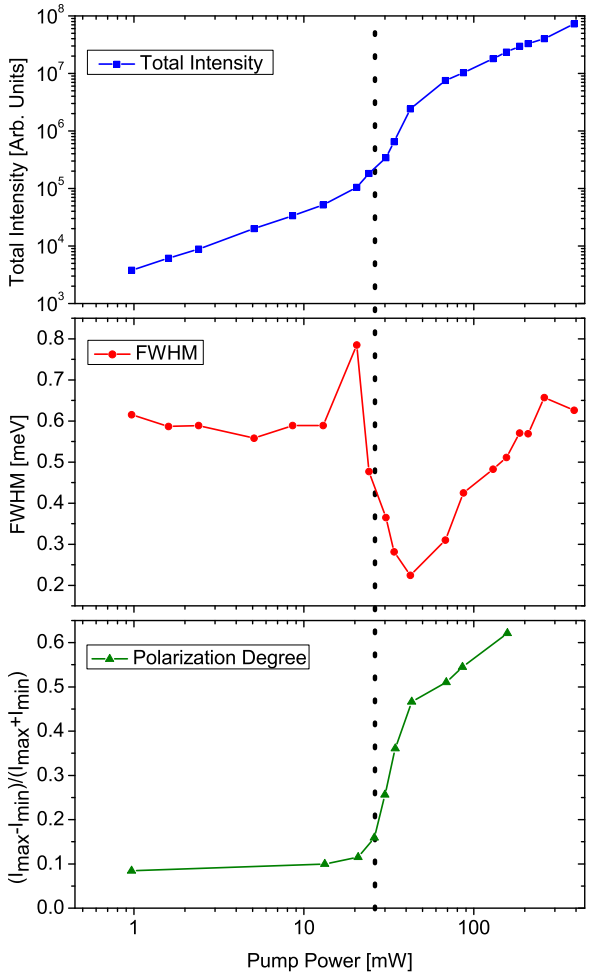

Figure 6.2: Top: Total intensity, Middle: Full width at half maximum of the spectral intensity, and Bottom: degree of polarization as a function of pump power the stressor setting that gives the lowest threshold

Figure 6.2 shows the total intensity at different pump powers with the corresponding spectral width and for the case where the sample is pumped at the bottom of the stress well, the degree of linear polarization of the polariton emission at $k_{\parallel} = 0$ was also measured. The nonlinear threshold is defined as the pump power at the largest spectral width just before it starts decreasing again. This coincides with the onset of nonlinear PL intensity and build up of linear polarization. Above 30 mW pump power, one can observe a nonlinear increase of intensity which becomes linear again at much higher pump power. Accordingly, there

is a dramatic narrowing of the spectral line width at the non-linear region, as shown by the middle plot. Other groups [8, 14] have observed similar results. Note that in our case, the pump beam is at the stop band edge with energy more than 120 meV higher than the trapped lower polaritons. The point of exciting the polaritons at much higher energy is to allow the polaritons to scatter and lose their coherence long before it accumulates in the ground state, so that the coherence that occurs is not driven but spontaneous.

Below the nonlinear threshold, the photoluminescence emission appears to be completely unpolarized. Above the threshold, one can observe build up of linear polarization. This is an intriguing phenomenon because phase transitions such as BEC should be accompanied by a form of ordering of the particles. If the polaritons are condensed in the ground state, it should be described by a single wave function. One therefore expects a build-up of the polarization of light. To make sure that the build up of polarization at the onset of the threshold is not due to the laser's polarization, the center of the stress well is pumped with a circularly polarized laser. Figure 6.3 clearly shows that the polarization is not due to the laser

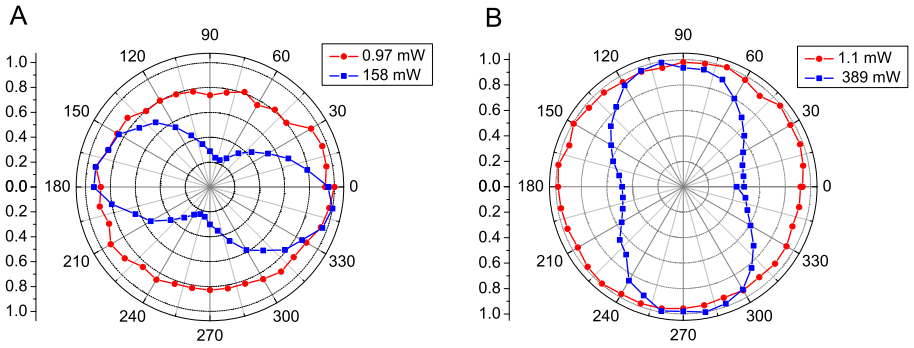

Figure 6.3: Polarization below (red) and above (blue) threshold for different sample orientations.

because of the dramatic difference in polarization below and above threshold. In addition, it is observed that the linear polarization follows approximately the general direction of the [110] axis of the crystal. It may be deduced that the direction of polarization follows some crystal axis, but the direction of polarization is not exactly fixed, it deviates around the [110] axis from day to day. Analysis of the LP fine structure in Chap. 8 reveal that this maybe due to the mixing of the light-hole and heavy-hole states with stress.

6.2 ANGLE-RESOLVED MEASUREMENTS

6.2.1 Angle-Resolved Power Series

At a given stress setting (see Fig. 4.3), the photoluminescence is collected for a set of angles ($-19°$ to $19°$) with respect to the normal of the sample for every power in a series of powers. Below threshold, the PL is spectrally broad with minimal intensity. Above the excitation threshold, one can clearly observe a distribution featured by a spectrally sharp and intense peak formed at the center of the emission distribution. A blue shift and flattening in momentum space is also observed. The blue shift is caused by renormalization due to scattering between particles. The flattening in momentum space has been explained as due to self-trapping [86] or localization of polaritons (see Chap. 6.3) resulting to the uncertainty broadening ($\Delta k \Delta x \geq 1$).

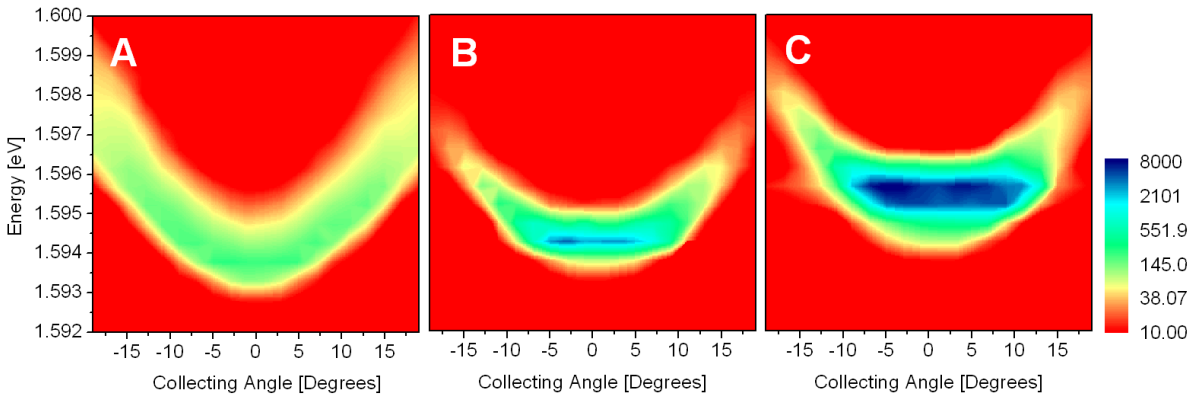

Figure 6.4: Angle resolved measurement below (2.3 mW), around (60 mW), and above threshold (139 mW) pump power

Angle-resolved measurements of the photoluminescence intensity (Fig. 6.4) demonstrate accumulation of particles in the ground state. In order to quantify that, we take representative samples of angle-resolved photoluminescence spectra and plot the relative occupation number versus the peak energy for a given k-wavevector or angle (see Fig. 6.5). The relative occupation number is derived from the angular intensity distribution while taking into account the lower polariton life time correction as a function of k (see Sec. 2.2.2). Below 12 mW pump power, the scattering mechanisms does not allow for particles to have enough

time to scatter to the ground state. Hence, neither a Maxwell-Boltzmann (MB) function nor a Bose-Einstein (BE) function fits well to the angular intensity distribution. However, just below the threshold (e.g. 37 mW), polaritons are able to thermalize possibly via polariton-polariton scattering mechanisms. At this power, the occupation as a function of peak energy at a given k-wavevector nicely fits the MB distribution with up to 98 percent confidence. The temperature of the cloud measure from this distribution is about 16 K. At the threshold (60 mW) the occupation fits the BE function by about 93 percent where temperature is fixed to 16 K with as the fit parameter. For the BE fit at 60 mW, the chemical potential μ is at -0.4 meV.

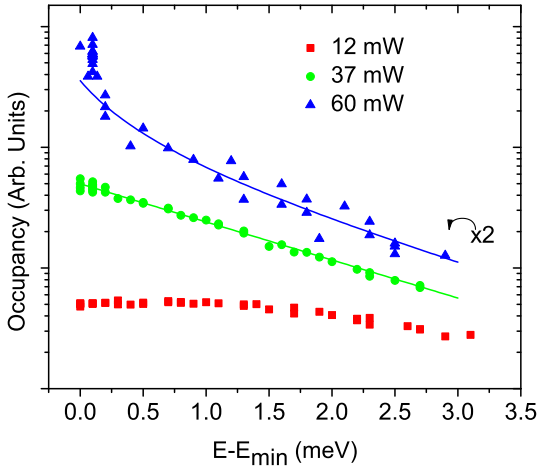

Figure 6.5: Occupation number from angle resolved measurement at three different powers: low pump power (12 mW), just below threshold (37 mW), at threshold (60 mW). The occupation just below threshold (green circles) is well fit with a MB distribution with temperature at 16 K. The occupation at threshold (blue triangles) gives a 93% confidence for a BE fit with $T = 16$ K and $\mu = -0.4$ meV.

6.2.2 Occupation at Different Detuning and Stress

It is important to point out one other role that the stress trap is playing in these experiments. As mentioned in a previous section, the bottleneck region is one of the features of the microcavity that prevents scattering to the center of the trap. For an unstressed microcavity (Fig. 6.6), one can see that the polaritons accumulate in the bottleneck region, corresponding to the maxima of the hump in the occupation plot, since the lowest polariton state is mostly photonic in character. In the stressed case, however, this hump or bottleneck accumulation goes away, as shown by the upturn in occupation as the bottom of the stress well becomes more excitonic. It could be argued that the more excitonic the polariton, the more gradual

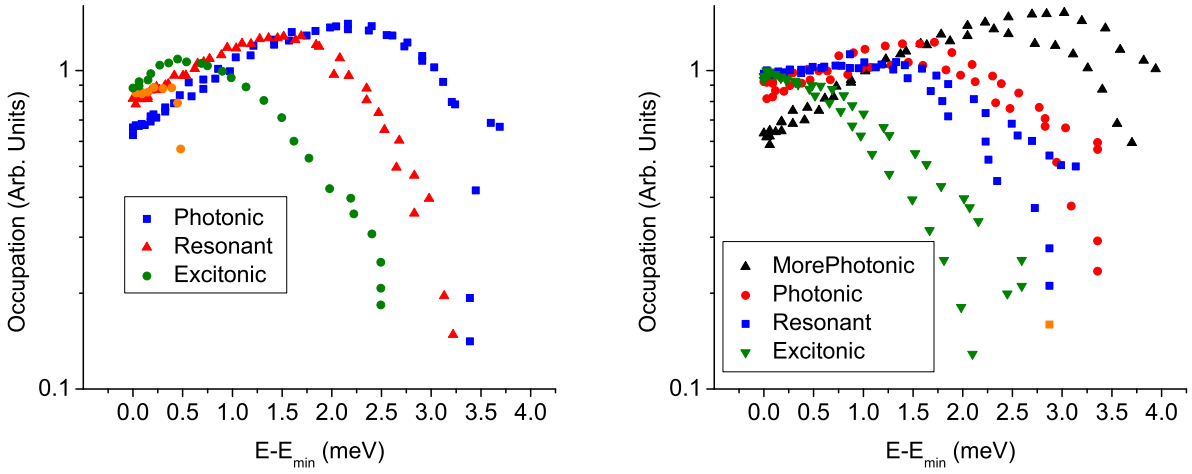

Figure 6.6: Comparison of the occupation at different detuning for the nonstressed and stressed case. Left: Occupation at different detuning as one moves across an unstressed sample through resonance Right: Occupation at different detuning as one stresses the sample through resonance

the energy dispersion curves, making the bottleneck effect less of an issue.

To single out the effect of the trap from the polariton character (exciton-like $\leftrightarrow$ photon-like), one could move the stressor point to different regions away from resonance, regions of negative detuning ($\delta = E_{ph} - E_{ex} < 0$). If a position is more negatively detuned, more stress is required to bring it into resonance with the cavity photon. Figure 6.7 is a series of occupation from less negatively detuned to a more negatively detuned region of the sample correspodingly increasing stress to bring it into resonance. This figure shows that at resonance, increased stress helps populate the low energy states more efficiently. This suggest that stress introduces a mechanism that helps polaritons overcome the bottleneck region such that they are able to scatter to the ground state. Numerical models [38] indicate that the applied stress may also play an indirect role in creating free carriers via ionization of impurities due to the piezoelectric effect induced by stress. These free carriers may help thermalize the polaritons to the lattice temperature.

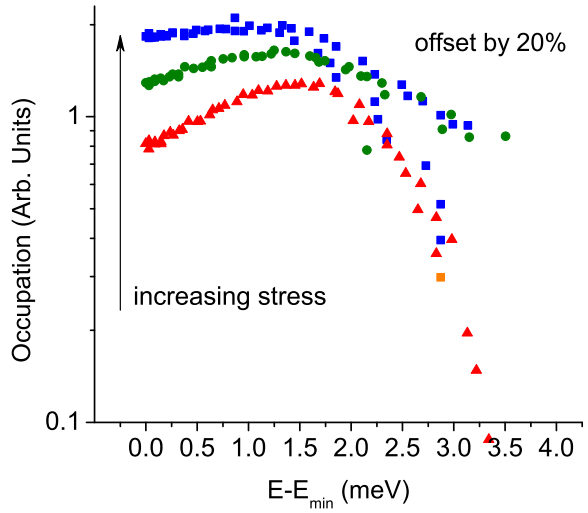

Figure 6.7: Stressed to resonance with different amounts of stress corresponding to different trap frequencies $\omega_0 = \sqrt{\gamma/m}$

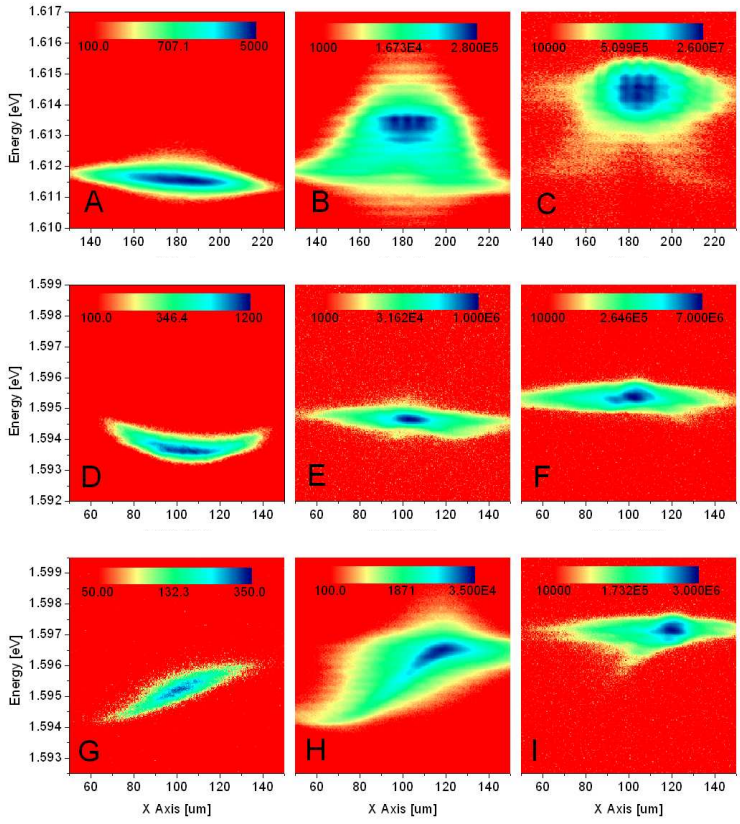

Figure 6.8: Series of spectral profiles at different pump powers Top Row: Pumping the unstressed resonant sample (a) 1.17 mW, (b) 51 mW, (c) 125 mW, Middle Row: Pumping the bottom of the stress well (d) 2.3 mW, (e) 49 mW, (f) 122 mW Bottom Row: Pumping the side of the stress well (g) 2.3 mW, (h) 49 mW, (i) 122 mW

6.3 REAL-SPACE DISTRIBUTION

Figure 6.8 shows real-space distribution of the energy profile for CW pumping at different conditions. This series of images presents a comparison of the unstressed case in a region of the sample with zero detuning of the exciton states relative to the cavity polariton states, and in the case where there is a stress trap. In the nonstressed case, polaritons diffuse freely from the excitation spot (see Fig. 6.8a-b). The spectrum is much wider and the spatial size of the emission peak is significantly larger when there is no trapping. At higher pump power, however, self trapping begins to dominate. One possible explanation[86] is that lattice is heating creates a local minimum that traps the polaritons since increasing lattice temperature red shifts the band gap[51, 50, 49]. High lattice temperatures at high pump power may also explain the low diffusion constant, spatial narrowing, and spectral broadening. This is one reason why we moved to the chopped-cw pump(see Chap. 7). In addition, we find no evidence of build-up in linear polarization of the light emission in the non-trapped case.

These figures (Fig. 6.8d-f) also show that the renormalization of the polariton energy due to polariton-polariton repulsive interactions has the effect of flattening out the trap. Since more polaritons accumulate in the center of the trap, the blue shift there will be largest, tending to cancel out the effect of the external trapping potential. Therefore in the trap, the potential felt by the polaritons is actually nearly flat. In the case of no trap, the polariton-polariton repulsive interactions actually will tend to lead to a potential maximum at the center of the laser excitation spot, which will have the effect of a pressure gradient causing fast expansion of the polariton cloud. The relatively large effect of renormalization due to particle-particle interactions in this system is the most significant way in which the theory differs from that of trapped atoms.

Another interesting effect observed is the dramatic spatial narrowing of the as one increases the pump power to create polaritons in the stress trap (see Fig. 6.9). The pump spot has an average FWHM of about 65 μm. Intuitively, one might think that with more particles and additional heating due to increased pump power that polaritons should fly apart but instead they condense. This is consitent with the theory of BEC in a trap [87] that the

condensate should occupy the ground state of the trap, which is spacially compact. Above the critical threshold, the spatial emission narrows to about 15 μm. This result is similar to a thoeretical estimate[59] of the size condensate using our experimental parameters.

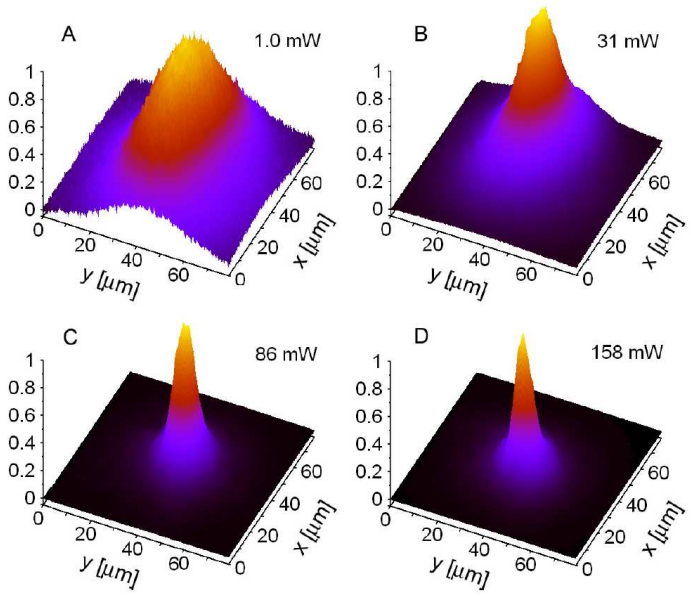

Figure 6.9: Two dimensional spatial profiles for a series of powers

6.4 MEASUREMENT OF SPATIAL COHERENCE

We can also see direct evidence of coherence in the first-order correlation of the photoluminescence, which is also seen in the work in CdTe structures [88]. Figure 6.10 shows images produced by sending the spatially resolved photoluminescence through two arms of a Michelson interferometer, when the interferometer is slightly misaligned to create a double image in which the left side of the image from one arm overlaps with the right side of the image from the other arm[1]. Below the critical excitation density threshold, we cannot see any interference fringes for any path difference of the two arms of the interferometer (Fig. 6.10A). Above the critical density, fringes appear (Fig. 6.10B) across the two polariton condensates. The faint fringes seen far away are not from the condensate but tails of a point spread function due to the response of the imaging system to the condensate emission which is acting like a point source. Figure 6.10C plots the visibility of the fringes, $(I_{max} - I_{min})/(I_{max} + I_{min})$,

[1]See Sect. 5.2 for a review of coherence measurement using a Michelson interferometer

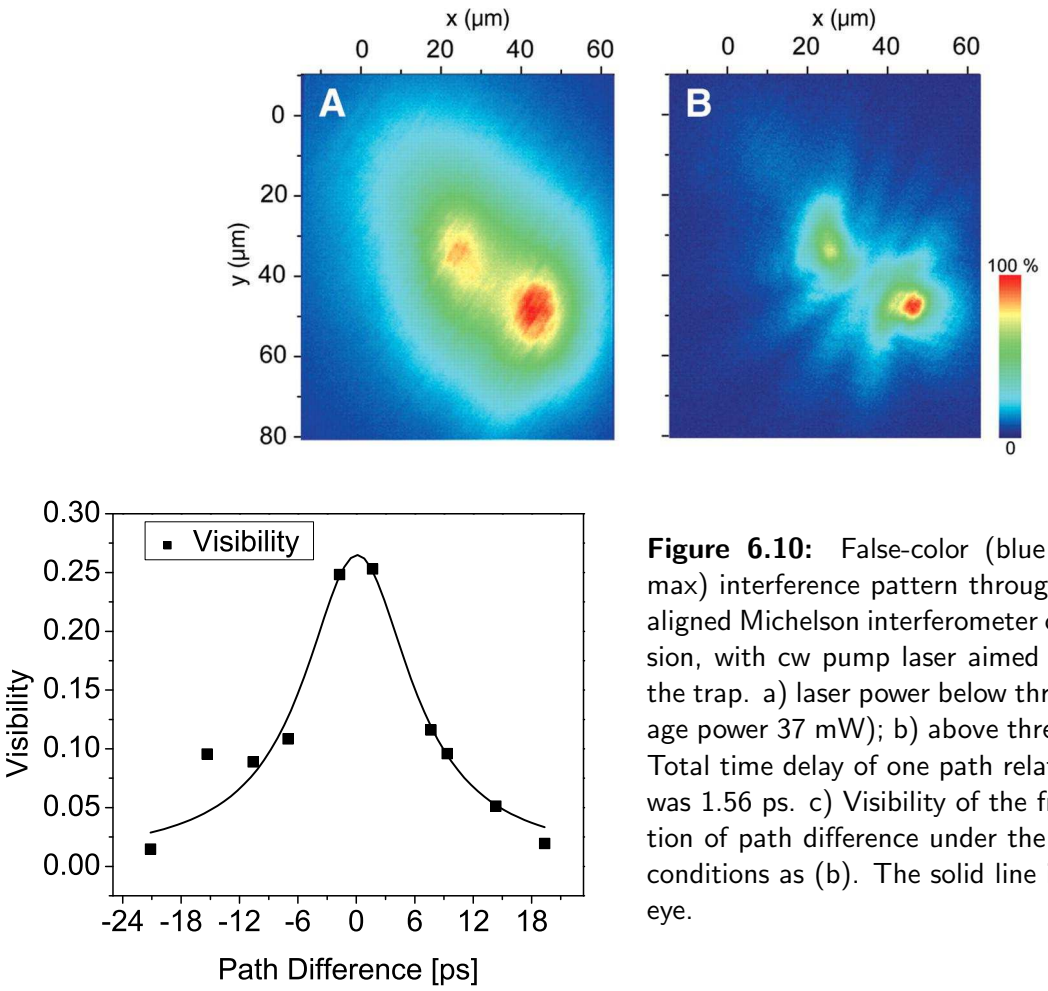

Figure 6.10: False-color (blue = min, red = max) interference pattern through a slightly misaligned Michelson interferometer of the light emission, with cw pump laser aimed at the center of the trap. a) laser power below threshold (cw average power 37 mW); b) above threshold (73 mW). Total time delay of one path relative to the other was 1.56 ps. c) Visibility of the fringes as a function of path difference under the same excitation conditions as (b). The solid line is a guide to the eye.

where I_{max} and I_{min} are the maximum and minimum intensity, respectively, as the path length is varied under the same excitation conditions as in Fig. 6.10B. The visibility is never 100%, which is consistent with recent theoretical predictions [89] that the condensate fraction of the polariton gas should be less than 50%. The coherence time increases from less than 1 ps below the critical threshold to 8 to 10 ps above the critical threshold, which is longer than the nominal lifetime of the polaritons in these structures of around 4 ps [9].

6.5 COMPARISON OF TRAPPED AND UNTRAPPED CASE

In earlier experiments showing nonlinearity of PL intensity, it was initially believed that it is enough to show weak coupling if the emission line lies midway between the UP and LP energy. Yet, even if that is not observed, photon lasing could still occur because of the change in refraction index when increasing the carrier density so that the photon mode is lower than midway between the UP and LP. This happens for most cases in untrapped polaritons. Due to the refractive index change, lasing regime can actually occur at a much lower energy than the uncoupled cavity or exciton mode[66]. This same effect also happens in trapped polaritons but, as will be later shown, the BEC transition occurs at lower density than the lasing transition. In this section we show the difference between the trapped and untrapped case. Recent results[90] prove that stress traps play an important role in the polariton quasiequilibrium condensation in GaAs microcavities.

To determine the point of strongest coupling and gauge the behavior of the polaritons away from that point, it is necessary to monitor the shift of the lines relative to resonance. Figure 6.11a shows the positions of the lines as a function of detuning across the sample. The lines are well fit with a simple three-state coupling model (see Appendix A). The fit functions correspond to the eigenvalues of the Hamiltonian matrix

$$\begin{pmatrix} E_{HH1} & 0 & \Omega_1 \\ 0 & E_{LH1} & \Omega_2 \\ \Omega_1 & \Omega_2 & E_{Phot} \end{pmatrix} \tag{6.1}$$

with $\Omega_1 = 7.55$ meV, $\Omega_2 = 6.0$ meV, $E_{HH1} = 1.616$ eV, $E_{LH1} = 1.646$ eV, and E_{phot} shifting with the wedge of the cavity as shown in Fig. 6.11.

The characteristics of the PL as a function of pump power in the nonstressed case, shown in Fig. 6.12, clearly show only one transition occurring. Furthermore, the shift in peak energy ≈ 4 meV is very close to the Ω_1 Rabi Splitting of 7.55 meV. Recall that the peak energy shift does not have to be equal to the Rabi Splitting Ω_1 since the cavity photon emission actually red shifts as the cavity index of refraction changes with PL intensity [66]. It is reasonable to claim that, with this amount of energy shift, the system is already in weak coupling. Therefore, the transition can be associated with a standard photon lasing transition.

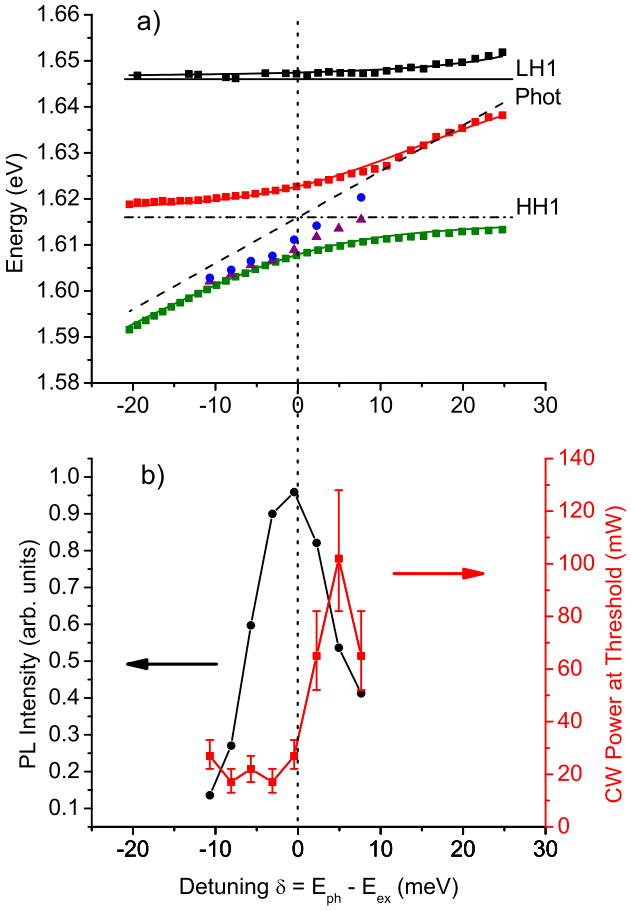

Figure 6.11: a) Squares: energy of the reflection maxima of the cavity as a function of detuning as the cavity and exciton energy changes in energy due to the gradient of the thickness in the sample. The data fits well to the model of coupled states discussed in the text, using the exciton energies (HH1, HH2) and cavity photon energy (Phot) shown. Triangles: the photon emission energy as a function of detuning when a laser excites the sample, with power at the threshold for coherent effects. The threshold is defined as the point of maximum spectral line width before spectral narrowing occurs. Circles: the photon emission energy when the laser excitation power is increased by a factor of 1.6 beyond the threshold power. Circles, left axis: Photoluminescence intensity of the lower polariton line as a function of detuning, for laser excitation density well below threshold (1.8 mW, with spot size 35 microns). The intensity is maximum at resonance, $\delta = 0$. Squares, right axis: The laser power needed to reach the threshold for coherent behavior (corresponding to the power used for the triangles in (a).) Laser spot size was 25 μm; laser photon energy was 714 nm, at the absorption at the top edge of the microcavity stop band.

To directly test whether the behavior of the coherent emission is different in the trapped case, we can look at the behavior of the system as the detuning is varied, not by varying the cavity length, as in Fig. 6.11, but by varying the exciton energy with stress. Figure 6.13a shows the energy of the states as the stress is increased to change the detuning. The point of resonance, i.e. the point of crossing of the bare cavity mode and the exciton mode, can be identified in two ways. First, we fit the shifts of the lines with stress to the simple model of coupled states as before. The parameters that coincide with the data or eigenvalues of the Hamiltonian matrix are $\Omega_1 = 7.5$ meV, $\Omega_2 = 6.0$ meV, $E_{phot} = 1.609$ eV, and with E_{HH1} and E_{LH1} shifting with stress. The result is shown as the solid lines in Fig. 6.13a. Second, we monitor the total photoluminescence intensity at very low pump intensity, as shown in Fig. 6.13b. As in Fig. 6.11b, the photoluminescence has a maximum at the point of resonance

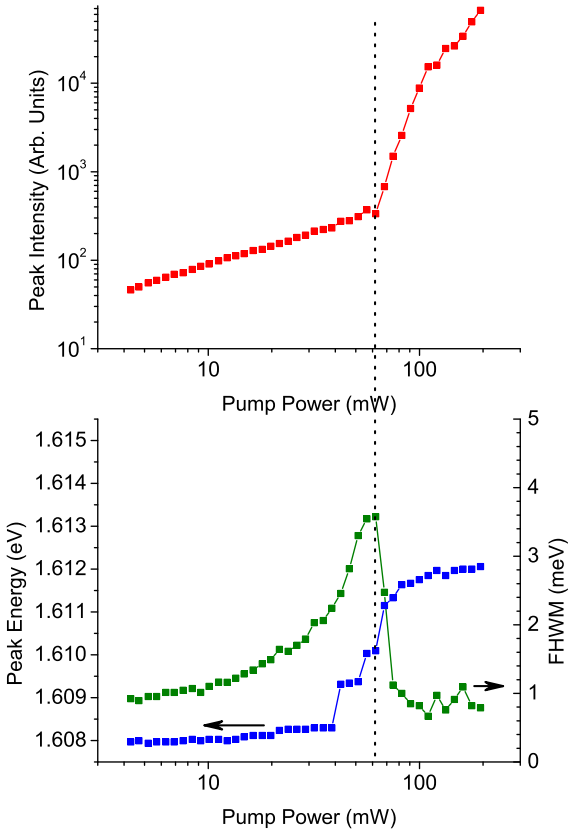

Figure 6.12: a) Peak intensity of the emission from the lower polariton as a function of pump power when the system is at zero detuning, when there is no stress trap - a location is chosen such that the exciton and cavity photon states are in resonance. b) Dots, left axis: peak photon energy of the emission for the same conditions as (a). Solid line, right axis: the full width at half maximum of the emission spectrum under the same conditions. The vertical dashed line is placed at the threshold pump power defined as the power at maximum FWHM just before nonlinearity in PL occurs.

(though it has been shown that there is a fine structure very near to the resonance point [71]). The FWHM of the PL intensity resonance around $\delta = 0$ is about 10 meV in both cases of Fig. 6.11b and Fig. 6.13b. As seen in Fig. 6.13a, when the pump power is increased to the threshold for coherent effects, the energy of the emission shifts upward slightly, around 0.5 meV, but follows the lower polariton energy as it shifts lower with increasing stress, until the detuning is around 4 meV. This clearly shows that the emission is still in the strong coupling regime, since it follows the exciton shift very closely with stress detuning. For detuning greater than 4 meV, the energy of the emission shifts up to near the bare cavity photon energy (indicated by the dashed line in Fig. 6.13a). At this point it is reasonable to assume that the system is no longer in strong coupling and the transition is a standard lasing transition, red shifted relative to the bare cavity mode, as in Fig. 6.11a and in Ref. [66]. As shown in Fig. 6.13b, to reach the standard lasing transition when the system is strongly

detuned, higher pump power, about a factor of two, must be used. This indicates that two different transitions, polariton lasing (nonequilibrium polariton BEC) and standard lasing, are occurring in the same sample. We therefore look to see both of these transitions occuring at the same point in the microcavity sample by changing the pump intensity. Figure 6.14 shows that this indeed is the case.

Fig. 6.14a shows the intensity of the emission at different pump powers. The spectral width is narrow, consistent with the low density and temperature of the polaritons. When the density is increased, the spectral width first broadens (Fig. 6.14b), as expected for collision broadening when the polaritons are at high enough density for substantial polariton-polariton scattering. At the critical threshold for coherence, the spectrum narrows (Fig. 6.14b). Love et al. [91] have recently argued that the intrinsic line width is much narrower, and the observed spectral width here is primarily due to intensity fluctuations of the pump laser, which is multimode in this case. This causes a fluctuating shift of the line position which is recorded by a time-integrating detection system as a broadened line. In the experiments of Love et al. [91], when an intensity-stabilized laser is used, very narrow line widths ($\sim$ 0.05 meV) and long coherence times ($\sim$ 150 ps) are recorded for this type of polaritonic transition. In addition, the shift in peak energy is less than 2 meV which is much smaller compared to the Rabi Splitting of $\Omega_1 = 7.5$ meV. When the pump power is increased even further (Fig. 6.14b), the emission broadens strongly and shifts strongly upward. This is consistent with high-density effects such as phase-space filling and strong polariton-polariton interaction, leading to breakdown of the pure polariton picture and onset of weak coupling as discussed in Chap. 3.4 Finally, a second line narrowing is seen at the same spot in the sample. This corresponds to standard lasing. At this point the shift in peak energy is more than 4 meV comparable to the weak coupling regime in the unstressed case. There are therefore two distinct transitions. The lower-power threshold can be identified with Bose condensation of polaritons in the strong coupling limit, which occurs only when the trap exists, while the higher threshold can be identified with standard lasing in the weak coupling regime, and occurs in the unstressed sample as well as in the stressed sample when it is detuned away from resonance. The trap plays an essential role in making the polariton condensate transition possible. If there is no trap, only the lasing transition can be seen in

these samples. If there is a trap, both transitions can occur. Work in microcavities with very high-quality reflection has also given indications of two distinct thresholds [92]. In that case, the condensation is aided by longer lifetime of the polaritons, while in our case, the condensation is aided by the trapping.

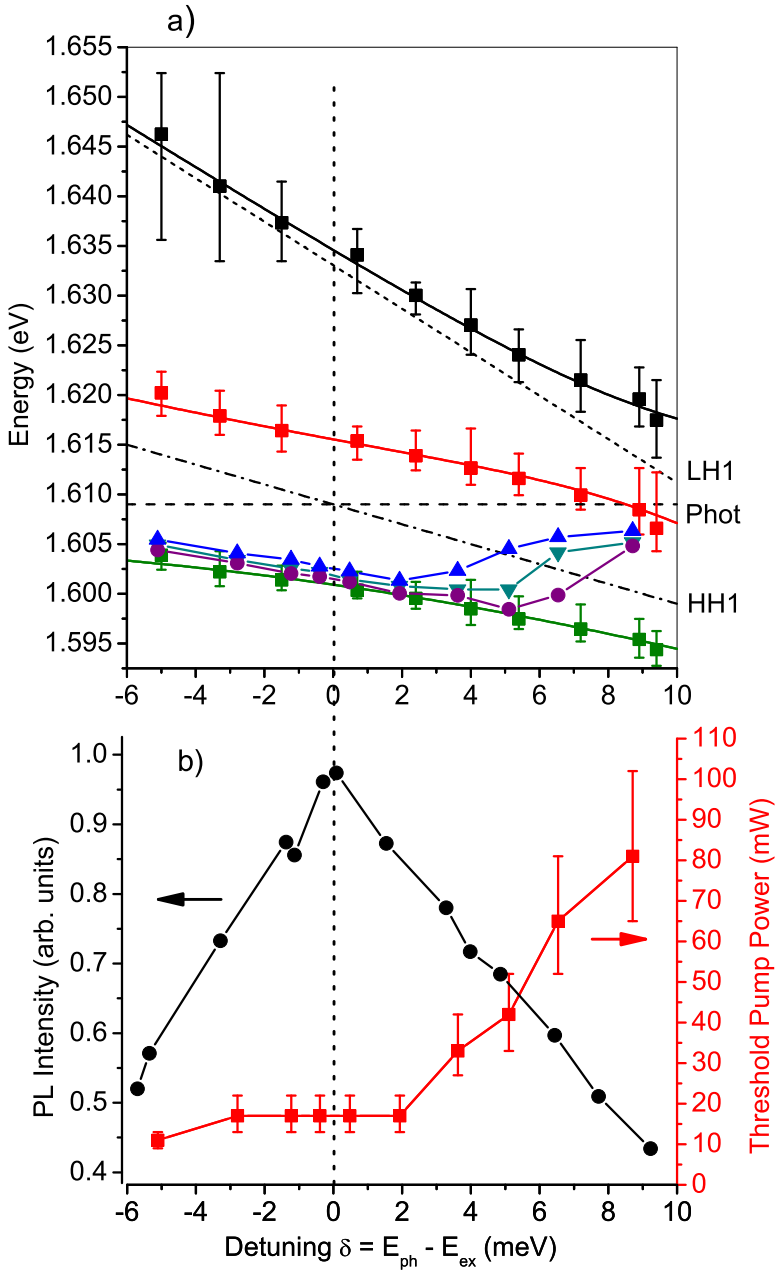

Figure 6.13: a) Squares: energy of the reflection maxima of the cavity as a function of detuning, when stress is applied to vary the exciton energy while leaving the cavity photon energy unchanged. The data are fits well to the model of coupled states discussed in the text, using the exciton energies (HH1, LH1) and cavity photon energy (Phot) shown. Circles: the photon emission energy as a function of detuning when a laser excites the sample, with power at the threshold for spectral narrowing. Inverted triangles: the photon emission energy when the laser excitation power is increased by a factor of 1.7 beyond the threshold. Upright triangles: the photon emission energy when the laser excition power is increased by a factor of 2.5 beyond the threshold. b) Circles, left axis: Photoluminescence intensity of the lower polariton line as a function of detuning, for laser excitation density well below threshold (9 mW, with spot size 85 microns). Squares, right axis: The laser power needed to reach the threshold for coherent behavior (corresponding to the power used for the circles in (a).) Laser spot size was 25 μm; laser photon energy was 716 nm, at the absorption at the top edge of the microcavity stop band.

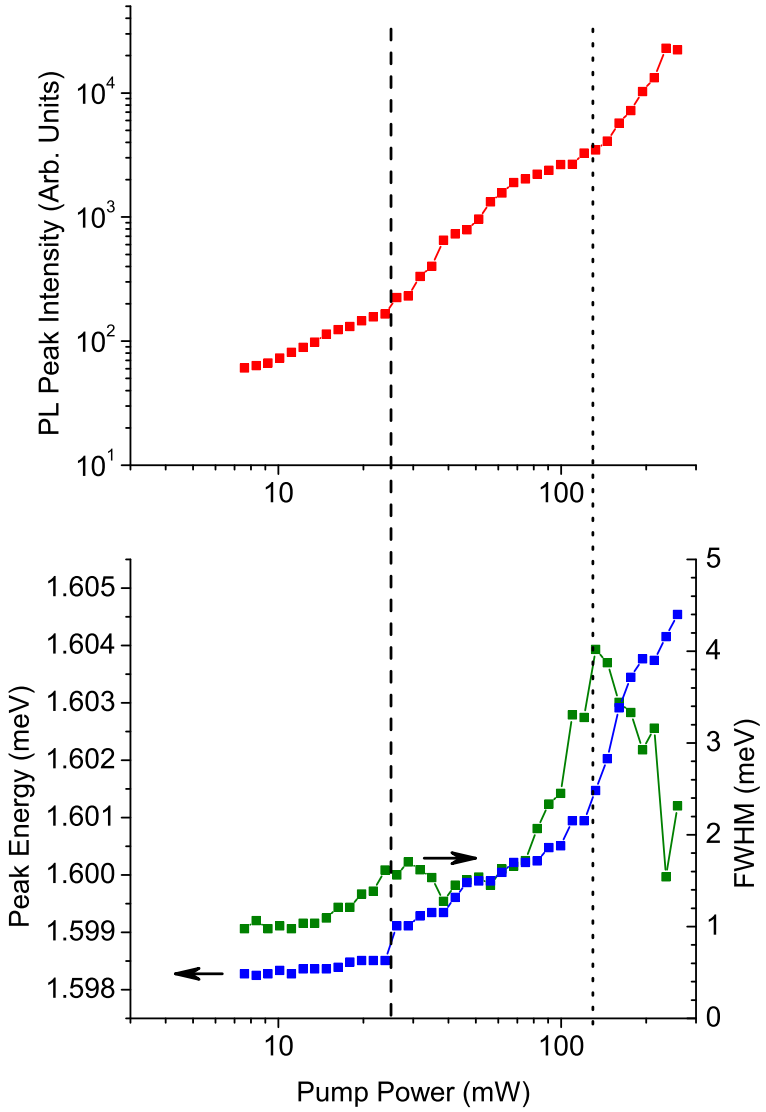

Figure 6.14: a) Peak intensity of the emission from the lower polariton as a function of pump power when the system is at zero detuning, when the polaritons are generated in a stress trap under the same conditions as those for Fig. 6.13. b) Dots, left axis: peak photon energy of the emission for the same conditions as (a). Solid line, right axis: the full width at half maximum of the emission spectrum under the same conditions. The acceptance angle for the PL detection was $0 \pm 3^\circ$. A different region of the sample was used, so that the lower polariton energy at zero detuning in this case is around 1.5984 eV, as compared to 1.600 eV in Fig. 6.13. The acceptance angle for the PL detection was the same as for Fig. 6.12. The vertical dashed (dotted) line is placed at the threshold pump power defined as the power at maximum FWHM just before nonlinearity in PL occurs corresponding to a BEC (lasing) density threshold.

7.0 EXPERIMENTAL RESULTS WITH MODULATED QUASI-CW PUMPING

While most of the experminents have been done with CW pumping, quasi-CW pumping has its advantages. With a CW laser, the lattice is heated and the diffusion length of the polaritons is much shorter (since polariton-phonon scattering is much faster). This means that to get polaritons in the center of the trap in significant number, we need to focus the laser on the center of the trap. However, there is an objection to pumping the center of the well with the laser in that it raises the possibility that the most intense part of the laser causes the effects that we see. With a modulated pump, less overall heating is going on in the lattice. This turns out to be essential to allow long range motion of the polariton gas. The disadvantage is that chopping the pump beam with an acousto-optic modulator for quasi-CW output is not an efficient process. Given our present system, we are not able to reach high enough density to observe the second threshold associated with ordinary photon lasing.

7.1 DIFFUSION AND TRAPPING AT THE CENTER OF THE WELL

Figure 7.1 is a series of images of the polariton luminescence as the laser spot is moved across the stress well. These polariton images are created by a pumping the edge of the stop band (718 nm) with pump power above the threshold. One can clearly see that self-trapping does not occur, but diffusion of polaritons gas to the center of the well. At very high pump powers, self-trapping due to local lattice heating will eventually dominate. For these images, the average laser power was 2.4 mW, for a circularly polarized, quasi-cw excitation with

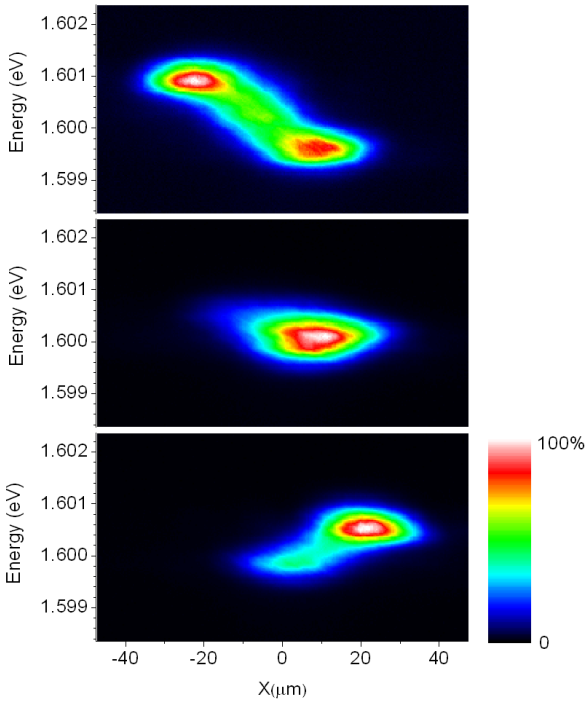

Figure 7.1: Spatially-resolved spectra of the light emission (external angle $\theta = 0 \pm 5.2°$) from polaritons in the microcavity structure, for three different positions of the laser. In (a), the polaritons area created on the left and flow to the right, in (b) they are created in the trap, while in (c) they are created on the right and flow to the left.

2.4% duty cycle at 1 kHz.

7.2 SIDE PUMPING POWER SERIES

In order to avoid ambiguity in regard to the possibility that the laser is causing the coherence at the center of the well, we pumped the side of the well. What is shown in Figure 7.2 is a series of images of polariton luminescence as the laser power is increased. Clearly, we see diffusion then trapping at the center of the stress well.

If we pump the side of the well, and look at the luminescence normal to the sample or at $k_{||} = 0$ just at the center of the well, we see still see the same nonlinear behavior above a density threshold similar to what we have seen with CW pumping. We also see the same spectral line narrowing. With pumping to the side, we have shown that the well has a huge contribution to these effects. Below the threshold line (dashed line), the spectral width of the photoluminescence emitted normal to the surface broadens with increasing density. Just above the threshold line, the width of the photoluminescence spectrum drops sharply. At

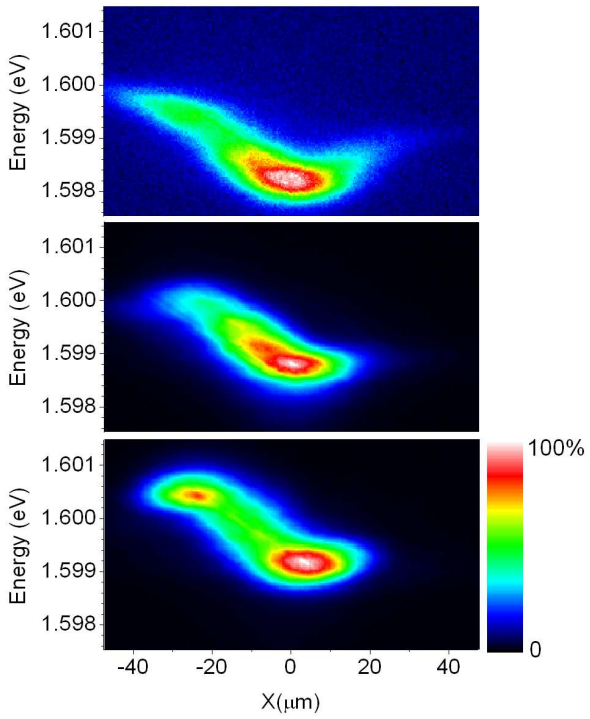

Figure 7.2: Spatially-resolved spectra of the light emission at (external angle $\theta = 0 \pm 5.2°$) from polaritons in the microcavity structure when the laser generates the polaritons on the left side of the trap, for three different laser powers (top t0 bottom): 0.4 mW, 1.4 mW, and 2.4 mW.

the same time, we observe spatial contraction (Fig. 7.3b) of the polariton cloud by a factor of three, down to the limit of our spatial imaging resolution (8 μm). As discussed in Chap. 6, spatial contraction is also a telltale sign for condensation in a trap because the condensate seeks the ground state of the system, which (in the case of a trapped gas) is a compact state at the bottom of the trap. Below the critical density, in the normal state, the size of the cloud is determined by a steady-state balance of the pumping by the exciting laser and thermal diffusion; above the critical density, the size of the cloud is given by the size of the ground state of the many-particle system. If interactions are neglected, the standard solution of a harmonic oscillator gives a ground-state wave function with extent[1] $\sigma = 3.8$ μm for our parameters.. As discussed in Chap. 6.3, in the presence of particle-particle repulsion, the size of the ground state will expand [87], but its size is still expected to be small compared to the size of the cloud of thermal particles. This is a major difference between experiments with

[1]Note that the normalized ground state wavefunction for the harmonic oscillator is given by

$$\Psi_0 = \left(\frac{m\omega_0}{\hbar\pi}\right)^{\frac{1}{4}} e^{-\frac{m\omega_0 x^2/\hbar}{2}}. \tag{7.1}$$

It is easy to see that the wavefunction is a Gaussian function with standard deviation $\sigma = \sqrt{\hbar/mw_0}$.

and without traps: In a translationally invariant geometry, a superfluid will flow outward; whereas, in a trap, it will flow inward.

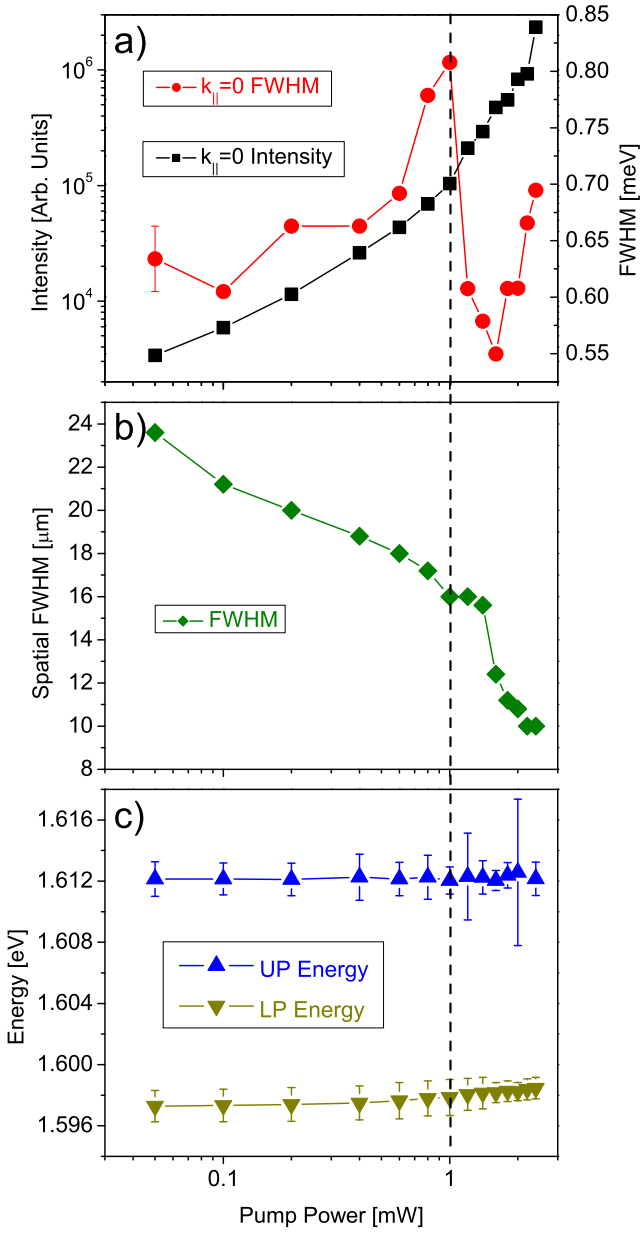

Figure 7.3: Data for polaritons in the center of the trap when the laser creates the polaritons on the side of the trap, far from the center, similar to the conditions of Figs. 7.1 and 7.2. a) Solid black squares: total photoluminescence intensity at $k_{||} = 0$ (external angle $\theta = 0 \pm 1.0°$) as a function of average excitation power, for quasi-cw excitation with 2.4% duty cycle. Red dots: Full width at half maximum of the emission spectrum at $k_{||} = 0$ under the same conditions. b) Full width at half maximum of the spatial profile of the photoluminescence collected for external angle $\theta = 0 \pm 5.2°$ from the center of the trap under the same conditions. c) Upper and lower polariton energies deduced from photoluminescence (lower polariton) and reflectivity (upper polariton) under the same conditions. The vertical dashed line is placed at the threshold pump power defined as the power at maximum FWHM just before nonlinearity in PL occurs.

Monitoring the shift of both the upper and lower polariton states (Fig. 7.3) shows that the system remains in the strong coupling regime during this transition. This is for the same experimental conditions as Figs. 7.1 and 7.2. The red and blue curves correspond to the upper and lower polariton lines at the center of the well. The LP shift in energy is only about an meV at the nonlinear regime (dashed line) compared to a Rabi splitting of 7 meV.

7.3 SIDE-PUMPING REAL SPACE DISTRIBUTION

Figure 7.4 shows the spatial profile of the polariton cloud with the laser focused to one side of the trap. The image of the profiles were obtained by projecting the PL emission of the cloud onto a CCD camera. Although the polaritons are created on the side, the polariton cloud drifts and remains centered on the bottom of the trap. As seen in Fig. 7.4A, at low pump power, the cloud is centered approximately $x = 50\,\mu$m, $y = 35\,\mu$m. As the power is increased, some of the polaritons remain in the region of the laser focus (Fig. 7.4B), at approximately approximately $x = 70\ \mu$m, $y = 35\ \mu$m, due to the decreased diffusion constant. At the critical threshold, Fig. 7.4C, a narrow peak appears at the trap center, much smaller than the thermal size of the cloud at low density, while another peak remains at the excitation laser spot. The peak the trap bottom continues to become sharper as the density is increased. At even higher pump power, nonlinearity caused by the laser spot dominates, seen as the most intense peaks in Fig. 7.4C and Fig. 7.4D. At these powers, 1.8 mW and 2.4 mW, normal lasing is probably occuring at the laser spot. These results prove that the spatial narrowing seen at the center of the trap can not come about simply by nonlinear gain of the laser profile; the peak is due the collection of the polaritons in the ground state of the harmonic potential of the trap.

7.4 ANGLE-RESOLVED MEASUREMENTS

A signature for BEC is evidenced by a bi-modal momentum distribution [93, 94, 95] of the particles, which can be measured for polaritons by resolving the angular distribution of the photoemission. This was seen in Fig. 6.5 for CW pumping at the center of the trap. Pumping on the side of the well, however, creates a problem when taking angle-resolved data. If one takes a spectra of the emission when pumping on the side, two distinct lines of emissions will register in the spectrometer, one coming from where the sample is pumped and another coming from the trapped polaritons at the center of the well. Due to this technical difficulty, we had to pump the bottom of the well directly for angle-resolved measurements.

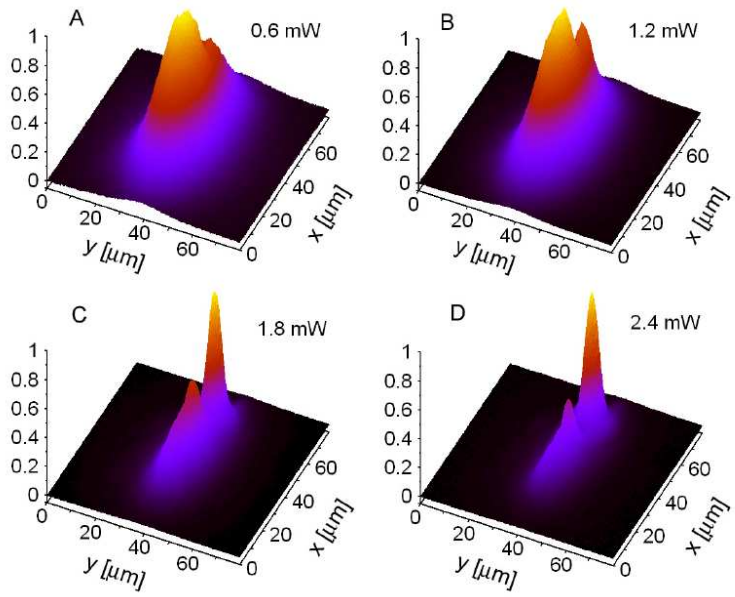

Figure 7.4: Two-dimensional spatial profile of the emission at $k_{||} = 0 \pm 5.2°$ for the average laser excitation powers given, under the same conditions as Figs. 7.1 and 7.2. The profiles are normalized in intensity

Figure 7.5 shows a series of angle-resolved spectra under the same conditions as in Fig. 7.3, but with the laser aimed at the center of the trap. A massive occupation in the ground state is clearly seen as we go above the luminescence nonlinear threshold. This is seen as a dramatic narrowing of both the in-plane momentum $k_{||}$ and energy of the polaritons above the critical threshold, while the blue shift due to interactions of the polaritons remains very low. The contraction in momentum space that is simultaneous with contraction in real space (Fig. 7.3B) does not contradict the uncertainty principle because both the spatial cloud size and the momentum distribution are determined by thermal scattering when the polariton gas is in the normal state, below the critical density threshold. Therefore, the total uncertainty in the normal state $\Delta k_{||} \Delta x$ (where $\Delta k_{||}$ is the uncertainty in the in-plane momentum and Δx is the uncertainty in the in-plane position) is much larger than unity. The spatial size of the condensate does imply a minimum width of the momentum peak at $k_{||} = 0$, which is consistent with our data within our spatial (8 μm) and spectral resolution (0.12 eV) limits. In the condensed state, $\Delta k \Delta x = (0.7 \times 10^4 \text{ cm}^{-1})(15 \times 10^{-4} \text{ cm}) = 10 > 1$, which is consistent

with the uncertainty principle.

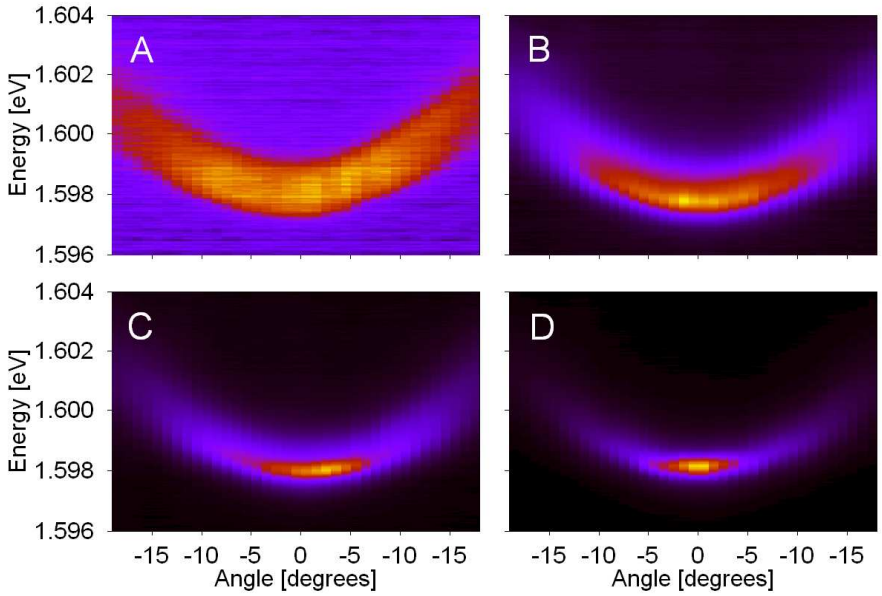

Figure 7.5: Angle-resolved light emission, for four different powers, under the same conditions as Fig. 7.3 but with the laser aimed at the center of the trap. a) 0.05 mW (far below the threshold excitation density), b) 0.4 mW (just below the threshold); c) 0.6 mW (at the threshold); d) 0.8 mW (above the threshold). The false color scale is linear, with yellow=high and black = low.

Recall that these images give the dispersion relation of our lower polaritons (A fit to Fig. 7.5 with a prabola gives the effective mass $7 \times 10^{-5} m_0$ we have used). From these measurements and the power correction factor (see Sect. 2.2.2), one can calculate the occupation number. Figure 7.6 shows the relative number of polaritons per $k_{||}$ state deduced from the same data. The energy for each $k_{||}$ is determined by the maximum of the measured spectrum at each $k_{||}$, in the same way as in Ref. [88]. Far below the critical density threshold, the polariton distribution is completely nonthermal. Just below the critical density threshold, at 0.4 mW , the distribution is well fit by a Maxwell-Boltzmann distribution $N(E_k) \propto e^{-E_k/k_B T}$ (where E_k is the particle energy, and $N(E_k)$ is the number of particles per state at that energy), which corresponds to a straight line on this plot. Using the temperature T as a fitting parameter we find that the effective temperature at equilibrium at around 97 K. This is much higher than $T = 16$ K found for CW pumping. It is consitent with numerical models[38] that show the polaritons are much more strongly coupled to the lattice when the temperature is

higher.

Above the critical threshold, there is a sharp increase in the number of polaritons near $k_{||} = 0$. The high temperature of the Maxwell-Boltzmann fit below the critical density, which is mirrored in the high-energy tails of the higher density $N(E_k)$, indicates that the polariton gas is not completely thermalized. As shown in recent theoretical works [93, 94, 95], the lack of complete equilibrium does not prevent the polariton gas from undergoing a phase transition to spontaneous coherence. The buildup of the particles at $k_{||} = 0$ is truly an effect of the Bose statistics, but the entire range of energy cannot be fit to an equilibrium Bose-Einstein distribution because the high kinetic energy particles ($E_k > 1.5$ meV) are constantly heated by hot polaritons generated by the laser. This is also true of the occupation number data of Ref. [88]. Steady-state quasiequilibrium theory [93, 94, 95] predicts a bimodal distribution function $N(E_k)$ (with a peak at $k_{||} = 0$ like that seen in Fig. 7.6, which corresponds to a condensate) even when the system is not in complete equilibrium.

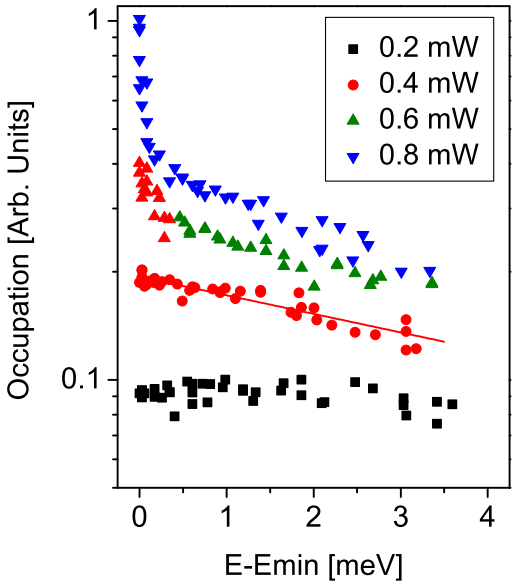

Figure 7.6: Number of polaritons per k-state, deduced from the light emission intensity as a function of angle, for the same conditions as Fig. 7.5, for four laser powers as labeled. The straight line is a fit to a Maxwell-Boltzmann distribution with T = 97 K.

7.5 POLARIZATION MEASUREMENTS

Similar to Ref. [88], we also see spontaneous buildup of linear polarization above the critical density threshold (Fig. 7.7) as in the cw-pumping case. Also, the threshold intensity are the

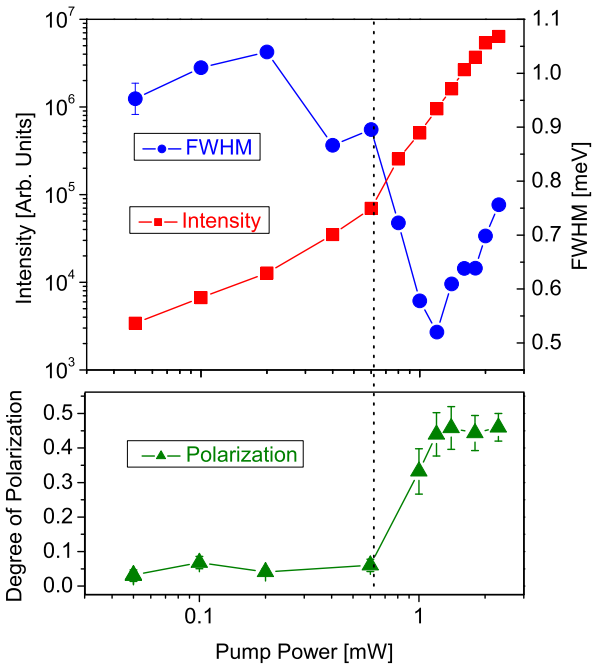

Figure 7.7: a) Red squares: Total photoluminescence intensity at $k_{||} = 0$ (external angle $\theta = 0 \pm 1.0°$) as a function of average excitation power, for the same conditions as Fig. 7.5. Blue dots: Full width at half maximum of the emission spectrum at $k_{||} = 0$ under the same conditions. b) Degree of polarization $(I_{max} - I_{min})/(I_{max} + I_{min})$ under the same conditions.

same as the cw case if duty cycle is accounted for. Below the threshold, the light emission is essentially unpolarized, which is not surprising because the pump light is circularly polarized and the generated carriers must emit numerous phonons. Above the critical threshold, the light becomes linearly polarized. We checked that this polarization is not related to the excitation polarization or to the detection system by rotating the sample relative to the system. We found that the linear polarization follows the sample orientation and is nearly aligned with the [110] axis of the crystal, as in the CdTe experiments [88]. The polarization angle also appears to depend weakly on the applied stress. Linear polarization has been predicted [96] to be a direct result of spontaneous symmetry breaking in the polariton condensate system; more recent theoretical work has shown that pinning along a crystal symmetry direction is expected[97]. In Chap. 8, we will discuss this splitting of the linear polarization in more detail. In general, when there is a condensate, any small term in the Hamiltonian that breaks the degeneracy of the ground state will cause the condensate to jump into the lowest energy state, even if the splitting is much less than $k_B T$ (refer to Chap. 3.3 for review).

8.0 EXPERIMENTAL MEASUREMENTS OF STRESS INDUCED SPLITTING

A state splitting of up to 700 μeV is observed in the lower and upper polariton branches of a stressed semiconductor microcavity polariton. The split states are linearly polarized and orthogonal to each other. In addition, it is important to note that one of the state couples to light better than the other, as seen by the difference in the Rabi splitting of the upper and lower polaritons. A sample spectra is shown in Fig. 8.1.

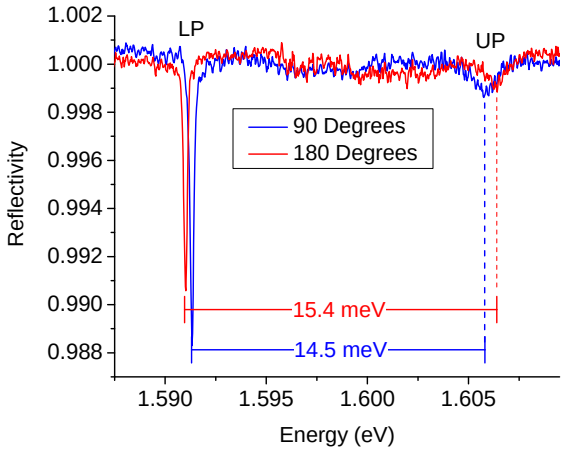

Figure 8.1: An example of the reflectivity spectra of the polariton through a 90° and a 180° polarizer orientation. The spectra are taken 150 μm away from the center of the stress well.

An example of the splitting of the lower polariton state in a line across the stress trap is shown in Fig. 8.2(a). The difference in energy between two bright states is extracted from photoluminescence measurements taken normal to the sample, and is plotted in Fig. 8.2(b). The range of stress for the data of Fig. 8.2(b) are taken from close to zero detuning to positive detuning ($\delta = E_{ph} - E_{ex}$). Normal to the sample, the transverse electric (TE) and transverse magnetic (TM) modes in the cavity are equivalent. Hence, the longitudinal-transverse splitting of polaritons does not contribute to the splitting. The splitting could arise from two possibilities. One is that it could be a direct effect of an energy splitting in the

degenerate bright exciton states (spin ± 1) into two orthogonaly polarized radiative states. Another possibility is that it could be due to a stress-induced birefringence in the microcavity resulting to a splitting of the bare photon mode into two polarized states. However, the photonic character is not enhanced in our case since the polariton becomes more exciton-like with increasing stress[90, 81]. It is safe to assume that the splitting caused by a small birefringence in the mirrors and cavity is not the dominant cause.

Exciton splitting due to exchange anisotropy is well studied in GaAs quantum wells and microcavities[98, 99, 100, 101, 102, 103, 104]. However, known energy splittings of excitons in quantum wells are typically only at most 200 μeV [99, 104, 101]. The mixing between heavy-hole and light-hole excitons is negligible in the unstressed case since they are far apart in energy ($\sim$ 30 meV difference for 7 nm quantum wells). In our experiments [40], the stress shifts the light-hole energy close to the heavy-hole energy making the mixing between the two states an important parameter to consider.

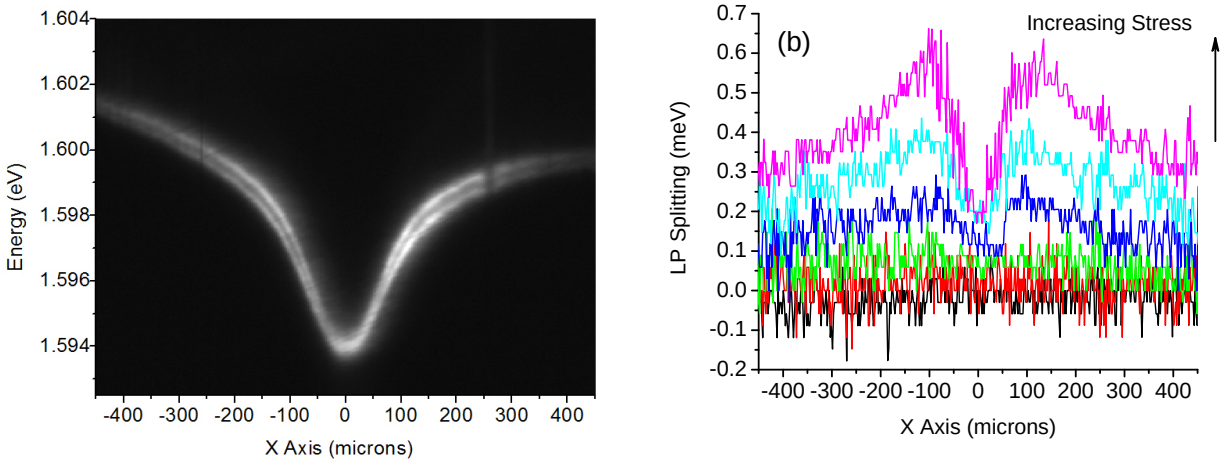

Figure 8.2: (a) An example of a lower polariton luminescence showing the splitting of the two bright states across a stressed microcavity sample (4.3 N force on the pin stressor, see Refs. [37, 40] for the stressor geometry). The colored lines traces the points of maximum intensity. (b) Measured splitting of the between the lower polariton states with increasing force on the pin stressor (0 N, 0.2 N, 1.0 N, 2.1 N, 3.2 N, and 4.3 N). The highest stress splitting corresponds to the difference (blue - red) of the curves in (a).

The breaking of the degeneracy of the two bright excitonic states is the result of a lowering of confinement symmetry that can be induced by external strain, piezoelectric fields inherent

and induced, and/or interface roughness possibly linked to the growth procedures[104, 105, 101]. This would mean a reduction of the symmetry of the QW from D_{2d} to C_{2v} [104]. Therefore, the [110] and [1$\bar{1}$0] are no longer degenerate, splitting the exciton states into orthogonal linearly polarized states. In D_{2d} symmetry group, both the conduction spin $s = 1/2$ states and valence $j = \pm 3/2$ states are represented by Γ_6. The product gives

$$\Gamma_6 \otimes \Gamma_6 = \Gamma_1 \oplus \Gamma_2 \oplus \Gamma_5.$$

The representations Γ_1 and Γ_2 correspond to the dipole-inactive $J = \pm 2$ states and the Γ_5 corresponds to the dipole-active $J = \pm 1$ states. When the symmetry is lowered to C_{2v}, the Γ_5 becomes $\Gamma_2 \oplus \Gamma_4$ which are optically-active x and y singlet states.

When the symmetry is lowered, it is natural to expect the exciton oscillator strength to also be different along the two crystal axis orientations [104]. Each polarization would then have a different Rabi splitting. In fact, the change in oscillator strength is a big factor in creating these huge polariton splittings, up to 700 μeV seen in our experiments, since the polariton splitting amplifies the spin splitting. The polariton energies for a given exciton state is found by diagonalizing the matrix,

$$\begin{pmatrix} E_i & \Omega_i \\ \Omega_i & E_{ph} \end{pmatrix}, \tag{8.1}$$

where Ω_i is the radiative coupling for exciton eigenstate i, which depends on the relative fraction of light-hole and heavy-hole exciton in the eigenstate.

The Hamiltonian that can split the degeneracy of the two bright states is the short-range electron-hole exchange interaction between a hole with spin S_h and an electron with spin S_h[106],

$$H_{exch} = -\sum_{i=x,y,z} a_i S_{h,i} S_{e,i}\ , \tag{8.2}$$

where the a's are the coupling constants. Anisotropy in the exchange interaction is enough to split the degeneracy of the exciton states but it is not a necessary condition if there is a strong mixing between the light- and heavy-hole excitons which is the case of our stressed microcavity sample. Adding the Pikus-Bir deformation Hamiltonian, which determines the

shift of the bands with stress, to the exchange term and diagonalizing the resulting Hamiltonian matrix leads to a splitting of the exciton energy and a difference in the coupling strength of the new states (see details in Appendix E). From the resulting exciton eigenstates and their corresponding coupling strength to the cavity photon, we can solve for the energy of new lower polariton states. For our fits to the data, we assume that the oscillator strength of the pure $J = \pm 1$ heavy-hole exciton and the pure $J = \pm 1$ light-hole exciton remain constant, but as the stress changes the relative fraction of eavy-hole and light-hole states in each of the two new exciton eigenstates, the oscillator strength of each exciton state must be recomputed.

The splitting in energies of the bright states using the Pikus-Bir plus exchange Hamiltonian for the exciton eigenstates, and then the polariton energy splitting using the calculated light-hole and heavy-hole fractions, is compared to the data in Fig. 8.3(b). The data is well fit using strain values, ε_{xx}, ε_{yy}, *etc.*, for a line across the sample 25 μm off the center of the pin stressor and in the direction of the [100] axis. The relevant parameteres used are listed in Table 8.1. The Rabi splitting Ω is proportional to the square root of the calculated oscillator strength $|\langle f|M|i\rangle|^2$, where the final states are the ± 1 spin photons and the inital states are the new eigenstates.

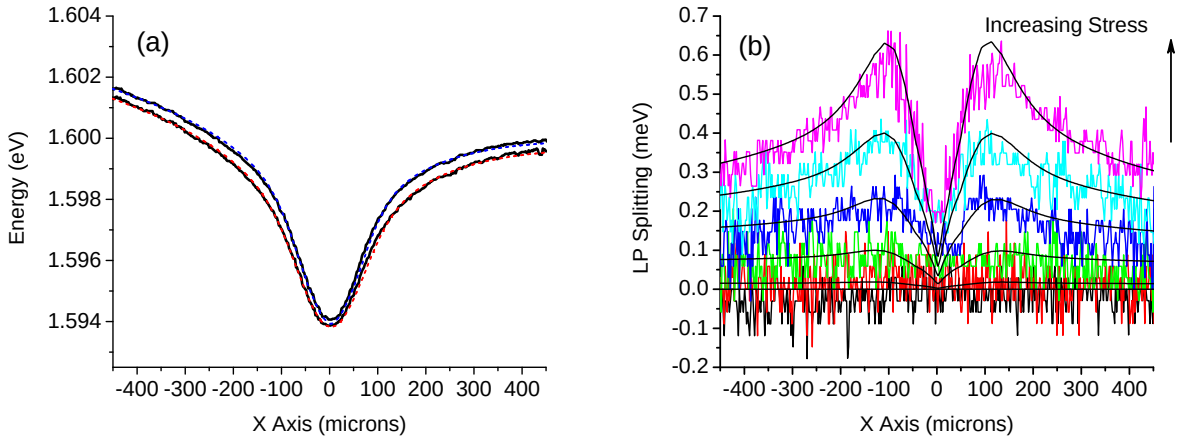

Figure 8.3: Splitting of the lower polariton with stress by adding the first exchange term to the Pikus-Bir Hamiltonian. (a) Colored lines show a sample fit to the photoluminescence of a stressed microcavity lower polariton from Fig. 8.2a (b) Fits to a series of stress splittings from Fig. 8.2b.

Table 8.1: Relevant parameters used for the Pikus-Bir and exchange term simulations shown in Fig. 8.3.

Hole diameter	1.25 mm
Pin diameter	25 μm
Relevant material parameters for GaAs/AlGaAs	Ref. [78, 79]
Exchange coupling terms $a_x = a_y$	1.14 meV
a_z	0.84 meV
Bare heavy-hole radiative coupling Ω_{hh}	7.55 meV
Bare light-hole radiative coupling Ω_{lh}	6.0 meV

From the eigenvectors of the effective hamiltonian (Pikus-Bir plus exchange), we can determine the direction of polarization of the exciton. One can write a general representation of the exciton polarization as

$$\mathbf{P}(\mathbf{x}) = \left(A_+\omega^+ + A_-\omega^-\right), \tag{8.3}$$

where $A_+(A_-)$ are the amplitudes of right(left) circularly polarized light $\omega_+(\omega_-)$ corresponding to the sum of eigenvector elements with +1(-1) spin. If the magnitude of the amplitudes are equal, $r = |A_-|/|A_+| = 1$, then the polarization is a 100% linear. For circular components with equal amplitude, it is easy to show that

$$\tan\theta = \frac{A_-\omega^-}{A_+\omega^+} = \frac{\omega^-}{\omega^+} \tag{8.4}$$

$$\theta = \frac{\alpha}{2} \tag{8.5}$$

where the circular polarization as a superposition of linear polarizations along the [100] and [010] axes, $\omega_\pm = \frac{1}{\sqrt{2}}(\epsilon_1 \pm i\epsilon_2)$, α is the phase difference between the amplitudes, $A_-/A_+ \propto e^{i\alpha}$, and θ is the direction of polarization with respect to the [100] axis. Calculating r and θ from our simulations show that the polarization is nearly 100% linear and points effectively in the [110] and the $[1\bar{1}0]$ directions, for lower polaritons near the center of the trap. In our earlier paper [37], we presented evidence of optical anisotropy in which the emission is

linearly polarized and pinned to one of the [110] crystallographic axis above threshold. We believe that this effect can be attributed to the anisotropy explained in this chapter.

These experiments provide an unusual degree of accuracy for the electron-hole exchange parameters, because the microcavity makes the spin splitting of the different eigenstates much larger than their line-widths. The sensitive dependence of the spin splitting on stress also makes this a tool for measuring stress optically that does not depend on the intensity of the lines. In addition, the splitting due to the stress trap removes the degeneracy of the ground state. This may be a crucial factor in the reported observation of a Bose-Einstein condensate in microcavity polaritons [19, 90], as compared to unstressed systems [92]. If the ground state is degenerate, the total number of particles in the ground state is divided equally among the degenerate states. This effectively increases the critical density threshold for BEC.

9.0 CONCLUSION

From the beginning, this research sought to experimentally show proof of BEC in MCPs. The first part consisted mainly of laying the ground work to make a polariton BEC theoretically possible. That task included designing a MC sample that can support strong coupling between excitons and photons such that an ensemble of stable polaritons could be studied. It took several simulations, design, characterization (mostly reflectivity measurements), and regrowing, which later on ended with the samples used in the experiments. The next task was to create a potential trap for the polaritons that does not significantly alter its properties. Stressing the sample, already having been tested and proven in the technique originally for DQWs, was the reasonable choice and was ultimately convenient in effectively producing the desired trap. After laying the ground work, the rest of the study proceeded in the search for the signatures of polariton BEC.

Preliminary investigations have shown that the polaritons truly acted as a delocalized gas, as demonstrated by its drift towards the stress-well minimum especially when a chopped laser is used to avoid lattice heating. Further experiments have produced several compelling evidence of Bose-Einstein condensation of polaritons. At the bottom of the trap, line narrowing and non-linear increase of photoluminescence intensity were observed. Also a single, spatially compact condensate gas of polaritons was formed in the trap analogous to the case of atoms in a three-dimensional harmonic potential. Above critical density, we observed massive occupation of polaritons in the ground state, spontaneous build-up of linear polarization and macroscopic coherence of the condensate as seen in interference fringes all in agreement with predictions. The dramatic transition of the system to a linearly polarized, compact, coherent, and beamlike source is consistent with the picture of quasiequilibrium condensation of polaritons.

Similar effects, however, were also observed in similar MC systems without traps. This raised the question whether traps play a significant role at all in producing these effects. Our experimental results prove that it does. Stressed samples showed a more efficient equilibration to the ground state. There are several aspects of the trap that have uniquely contributed to the observation of BEC in our experments, namely: confinement of polaritons even when created away from the trap center, change of the density of states, breaking of ground state degeneracy, and the possibility of electron-polariton scattering due to free carriers by stress-induced piezo-electric effect. More importantly, the use of stress traps has allowed us to demonstrate a distinction between BEC and lasing. Comparison of the trapped and untrapped MCPs showed that the trapped case has two distinguishable transitions which can be associated with pure photon lasing and BEC. For an identical sample, the untrapped case showed only the photon lasing transition. The presence of two thresholds, one for BEC and one for photon lasing, in the same trapped polariton system has so far been the most incontrovertible evidence for achieving BEC in MCPs.

10.0 FUTURE DIRECTIONS

The study of Bose-Einstein condensation of polaritons is very much alive today, with a flurry of exciting developments[107] that have been recently published. The most recent of these is the demonstration of superfluid flow of a polariton condensates at long distances while maintaining the population of these short-lived particles via parametric scattering[108]. Quantum vortices[109], another feature of superfluidity, have also been seen before that. In addition, evidence of a condensed phase in the form of a Bogoliubov-like spectrum of polariton condensates, as predicted by N. Bogoliubov for weakly interacting bosons[110], has been presented[111]. Transition to a single macroscopic coherent state was also shown over spatially delocalized disorder or potential traps[112]. Finally, some progress has been made with room temperature polariton lasing using GaN microcavities[113], an encouraging step toward the realization of polariton lasers as a new source of coherent light.

The results presented in this dissertation and elsewhere[37, 40, 90] have been a valuable contribution to the study of BEC of polaritons and macroscopic quantum phenomena in general. Our experiments have allowed theory [81, 59, 38] to treat a quasi-equilibrium gas with a known confining potential. Nevertheless, further manifestations of BEC may be examined and fitted to theory. A key test is comparing the two-dimensional (k_x and k_y) k-distribution of the polariton cloud below and above the condensate critical density. As the trapping potential has some anisotropy to it, above threshold equilibration of the polariton cloud should lead to an isotropic k-distribution of the condensate. By contrast, above threshold, the condensate's k-distribution must reflect the anisotropy of the trap. Such a test has been started by my junior colleague and will be presented in a separate dissertation. In addition, knowledge could be further gained in studying its dynamics. Ultrafast time-resolved measurements will have to be made to understand the scattering mechanisms,

thermalization times, and evolution of the polaritons to completely understand the process behind thermodynamic transitions that may occur. The system should be checked for a critical density threshold with its exact measure, its temperature dependence, and its agreement to predictions of thermodynamic theories of weakly-interacting bosonic gases. The spectral and spatial time-resolved distributions of the polaritons in the trap should be checked for spectral and spatial peaks. Macroscopic coherence of polaritons in second order as well as first order may also be investigated.

APPENDIX A

DEFINITION OF POLARITON HAMILTONIAN MATRIX

For two coupled quantum mechanical oscillators, we can write the Hamiltonian of the system as

$$H = E_{ph} a_k^\dagger a_k + E_{ex} b_k^\dagger b_k + \Omega(a_k^\dagger b_k + b_k^\dagger a_k) \tag{A.1}$$

where $a_k^\dagger$ and $b_k^\dagger$ are the photon and exciton creation operators. The interaction term Ω is called the Rabi splitting which determines the strength of dipole interaction between the exciton and the light field. Note that

$$\begin{aligned} a_k^\dagger|0\rangle \equiv |ph\rangle \quad &, \quad \langle 0|a_k \equiv \langle ph| \\ b_k^\dagger|0\rangle \equiv |ex\rangle \quad &, \quad \langle 0|b_k \equiv \langle ex|. \end{aligned}$$

Hence,

$$H = E_{ph}|ph\rangle\langle ph| + E_{ex}|ex\rangle\langle ex| + \Omega(|ph\rangle\langle ex| + |ex\rangle\langle ph|) \tag{A.2}$$

and the matrix Hamiltonian is given by

$$\begin{aligned} H &= \begin{pmatrix} \langle ex| H |ex\rangle & \langle ex| H |ph\rangle \\ \langle ph| H |ex\rangle & \langle ph| H |ph\rangle \end{pmatrix} \\ &= \begin{pmatrix} E_{ex} & \Omega \\ \Omega & E_{ph} \end{pmatrix}. \end{aligned} \tag{A.3}$$

For the three state coupling mode,

$$H = E_{ph} a_k^\dagger a_k + E_{HH1} b_k^\dagger b_k + E_{LH1} c_k^\dagger c_k + \Omega_1(a_k^\dagger b_k + b_k^\dagger a_k) + \Omega_2(a_k^\dagger c_k + c_k^\dagger a_k) \tag{A.4}$$

where $a_k^\dagger$, $b_k^\dagger$, and $c_k^\dagger$ are the photon, heavy-hole exciton, and light-hole exciton creation operators. The interaction term Ω_1 (Ω_2) are the coupling terms for the strength of dipole interaction between the heavy-hole exciton (light-hole exciton) and the light field. Following the same procedure used earlier for the two coupled quantum mechanical oscillators, we get Hamiltonian matrix for the three state state coupling as

$$\begin{pmatrix} E_{HH1} & 0 & \Omega_1 \\ 0 & E_{LH1} & \Omega_2 \\ \Omega_1 & \Omega_2 & E_{ph} \end{pmatrix}. \tag{A.5}$$

APPENDIX B

QUANTUM THEORY OF EXCITON-POLARITONS

The theory of exciton-polaritons was introduced by J.J. Hopfield [20] in 1958. From that time until the present, it has been refined and applied to various systems. The goal of this appendix is to provide sufficient details for the reader to have a substantial understanding of the theory. Here, I will follow and unify the work done by Hopfield [20], Kittel [114], and Quattropani et. al. [115] using details that can be looked-up from well-known physics texts by Jackson [116] and Klingshirn [117]. The reader may also follow derivations provided for by D.W. Snoke in his recent book, see Ref. [53], which discusses closely related topics.

I will begin by solving a simple model for the dielectric function $\epsilon(\omega)$. The model is of an electron attached to a spring. Here, I will ignore the damping term and spatial dispersion to have a simple but pedagogical illustration of polaritons. The equation of motion of the oscillator is given by Newton's second law.

$$\begin{aligned} m(\ddot{\mathbf{x}} + \omega_0'^2\mathbf{x}) &= -e\mathbf{E}(x,t) \\ \ddot{\mathbf{x}} + \omega_0'^2\mathbf{x} &= -\frac{e}{m}\mathbf{E} \\ \ddot{\mathbf{p}} + \omega_0'^2\mathbf{p} &= -\frac{e^2}{m}\mathbf{E} \end{aligned} \tag{B.1}$$

where $\mathbf{p}$ is the dipole moment, $\mathbf{E}$ is the driving field, and ω_0' is the resonant frequency. The solution to this single electron oscillator is given by

$$\mathbf{p} = \frac{e^2}{m}(\omega_0'^2 - \omega^2)^{-1}\mathbf{E} \tag{B.2}$$

The prefactor e^2/m gives the coupling of the electromagnetic field to the oscillator in our simple model. The prime in ω_0' indicates corrections due to local fields and quantum mechanics which I will later take into account.

For simplicity let us take N uncoupled oscillators. We then have the macroscopic polarization given by

$$\mathbf{P} = N\mathbf{p} = \frac{Ne^2}{m}(\omega_0'^2 - \omega^2)^{-1}\mathbf{E} \tag{B.3}$$

Recall that

$$\mathbf{P} = \epsilon_0\chi\mathbf{E} \text{ and } \frac{\epsilon(\omega)}{\epsilon_0} = 1 + \chi. \tag{B.4}$$

Hence,

$$\frac{\epsilon(\omega)}{\epsilon_0} = 1 + \frac{Ne^2}{\epsilon_0 m}(\omega_0'^2 - \omega^2)^{-1} \tag{B.5}$$

For dense materials such as GaAs, the local field $\mathbf{E}_{loc}$ acting on the oscillators consists of the external field $\mathbf{E}$ and the internal field $\mathbf{E}_i$ created by other dipoles. For a set N of same kinds of molecules, $\mathbf{P} = N\langle\mathbf{p}_{mol}\rangle$ or in general $\mathbf{P}(x) = \sum N_i\langle\mathbf{p}_i\rangle$ where $\mathbf{p}_i$ is the dipole moment of the ith type of molecule in the medium. Again for the same molecules

$$\begin{aligned} \mathbf{P} &= N\langle\mathbf{p}_{mol}\rangle \\ \langle\mathbf{p}_{mol}\rangle &= \epsilon_0\gamma_{mol}\mathbf{E}_{loc} \\ \mathbf{P} &= N\epsilon_0\gamma_{mol}\mathbf{E}_{loc} \end{aligned} \tag{B.6}$$

The molecular susceptibility γ_{mol} is given by the *Clausius-Mossotti* equation (see Jackson [116])

$$\begin{aligned} \gamma_{mol} &= \frac{3}{N}\left(\frac{\epsilon(\omega)/\epsilon_0 - 1}{\epsilon(\omega)/\epsilon_0 + 2}\right) \\ &\text{or} \\ \chi_e &= \frac{\gamma_{mol}}{1 - \frac{1}{3}N\gamma_{mol}} \end{aligned} \tag{B.7}$$

The *Clausius-Mossotti* equation holds true for dense materials with large dielectric constants such as GaAs. Plugging γ_{mol} from our derivation previously,

$$\begin{aligned} N\epsilon_0\gamma_{mol} &= \frac{Ne^2/m}{(\omega_0'^2-\omega^2)} \\ N\epsilon_0\frac{3}{N}\left(\frac{\epsilon(\omega)/\epsilon_0-1}{\epsilon(\omega)/\epsilon_0+2}\right) &= \frac{Ne^2/m}{(\omega_0'^2-\omega^2)} \\ \frac{\epsilon(\omega)/\epsilon_0-1}{\epsilon(\omega)/\epsilon_0+2} &= \frac{Ne^2/3\varepsilon_0 m}{(\omega_0'^2-\omega^2)} \end{aligned} \tag{B.8}$$

One can recover the original form of the dielectric function if we rewrite the resonant frequency as a shifted eigenfrequency.

$$\omega_0^2 = \omega_0'^2 - \frac{Ne^2}{3m\epsilon_0}$$

Hence,

$$\begin{aligned} \frac{\epsilon(\omega)/\epsilon_0-1}{\epsilon(\omega)/\epsilon_0+2} &= \frac{Ne^2/3\varepsilon_0 m}{(\omega_0^2+Ne^2/3\varepsilon_0 m-\omega^2)} \\ \frac{\epsilon(\omega)}{\epsilon_0} &= 1+\frac{Ne^2}{\epsilon_0 m}(\omega_0^2-\omega^2)^{-1} \end{aligned} \tag{B.9}$$

The resonant frequency ω_0 is the observable quantity.

In quantum mechanics, the coupling term is given by the square of the allowed dipole transition matrix element

$$\left|H_{if}^D\right|^2 = \left|\langle f|\, H^D\, |i\rangle\right|^2$$

where i is the initial state, f is the final state and H^D is the dipole operator $e\mathbf{x}$. There are various conventions for introducing the transition matrix element into the dielectric function. I shall use use the convention as Klingshirn [117] used in his book. The a dimenstionless quantity $\hat{f} = \frac{2m\omega_0'}{\hbar e^2}|H_{ij}^D|^2$ will be used to multiply the term $Ne^2m^{-1}\epsilon_0^{-1}$. The product is often called the oscillator strength f i.e.

$$f = \frac{2N\omega_0'}{\epsilon_0\hbar}|H_{ij}^D|^2$$

The dielectric function, in this notation, can then be written as

$$\frac{\epsilon(\omega)}{\epsilon_0} = 1 + \frac{f}{\omega_0^2 - \omega^2}. \tag{B.10}$$

We shall see later that this oscillator strength f will show up in the coupling constant of the interaction Hamiltonian of the polarization field and the photon field. Hopfield [20] in his seminal paper on polaritons rewrites this dielectric function in this form

$$\frac{\epsilon(\omega)}{\epsilon_0} = 1 + \frac{\omega_0^2\beta}{\omega_0^2 - \omega^2}$$

where $f = \omega_0^2\beta$. One can also arrive at this form of the dielectric function if we rewrite the general equation of motion of the macroscopic polarization density $\mathbf{P}$ in the presence of a driving electric field $\mathbf{E}$ as

$$\ddot{\mathbf{P}} + \omega_0^2\mathbf{P} = \epsilon_0\omega_0^2\beta\mathbf{E}(x,t) \tag{B.11}$$

From this equation of motion, we could deduce the Lagrangian density for the polarization field of this equation of motion. The Lagrangian can be written in two ways which are equivalent and of course leads to the same equation of motion.

$$\mathcal{L}_P = \frac{1}{2\epsilon_0\omega_0^2\beta}(\dot{\mathbf{P}}^2 - \omega_0^2\mathbf{P}^2) + \mathbf{E}\cdot\mathbf{P} \tag{B.12}$$

$$\mathcal{L}_P = \frac{1}{2\epsilon_0\omega_0^2\beta}(\dot{\mathbf{P}}^2 - \omega_0^2\mathbf{P}^2) + \mathbf{A}\cdot\dot{\mathbf{P}} \tag{B.13}$$

Note that we can write $\mathbf{E} = -\nabla\phi - \dot{\mathbf{A}}$, $\mathbf{B} = \nabla\times\mathbf{A}$ and that $\nabla\cdot\mathbf{A} = 0$ in the Coulomb gauge. Also for no source charge present, $\phi = 0$. It is also important to keep in mind that only the transverse modes couple with the photons. The longitudinal fields do not. Hence, we can write $\mathbf{A} = \mathbf{A}_T + \mathbf{A}_L = \mathbf{A}_T$. I will use the first form of the polarization Lagrangian, Eq. (B.12), so that we could write the total Lagrangian for the photon field, polarization field, and photon-polarization interaction as

$$\mathcal{L}_{tot} = \frac{\epsilon_0}{2}\dot{\mathbf{A}}^2 - \frac{1}{2\mu_0}(\nabla\times\mathbf{A})^2 + \frac{1}{2\epsilon_0\omega_0^2\beta}(\dot{\mathbf{P}}^2 - \omega_0^2\mathbf{P}^2) - \dot{\mathbf{A}}\cdot\mathbf{P} \tag{B.14}$$

The dots in the vector fields represent partial derivatives in time. From the Lagrangian, the total Hamiltonian density is written as,

$$\begin{aligned}\mathcal{H}_{tot} &= \sum_{l=1}^{3}\left(\frac{\partial\mathcal{L}_T}{\partial\dot{A}_l}\dot{A}_l + \frac{\partial\mathcal{L}_T}{\partial\dot{P}_l}\dot{P}_l\right) - \mathcal{L}_T \\ \text{where} \\ M_l &= \frac{\partial\mathcal{L}_T}{\partial\dot{A}_l} = \epsilon_0\dot{A}_l - P_l \\ \Pi_l &= \frac{\partial\mathcal{L}_T}{\partial\dot{P}_l} = \frac{\dot{P}}{\epsilon_0\omega_0^2\beta}\end{aligned} \tag{B.15}$$

$$\mathcal{H}_{tot} = \frac{1}{2\epsilon_0}\mathbf{M}^2 + \frac{1}{2\mu_0}(\nabla\times\mathbf{A})^2 + \frac{\epsilon_0\omega_0^2\beta}{2}\Pi^2 + \frac{1}{2\epsilon_0}(1+\frac{1}{\beta})\mathbf{P}^2 + \frac{\mathbf{M}\cdot\mathbf{P}}{\epsilon_0} \tag{B.16}$$

The vector field $\mathbf{A}$ is given by

$$\mathbf{A} = \left(\frac{\hbar}{\epsilon_0 V}\right)^{1/2}\sum_{k\lambda}\frac{\varepsilon_\lambda(k)}{\sqrt{2\omega_k}}\left\{\mathbf{a}_{k\lambda}^\dagger e^{-i\mathbf{k}\cdot\mathbf{x}} + \mathbf{a}_{k\lambda}e^{i\mathbf{k}\cdot\mathbf{x}}\right\} \tag{B.17}$$

and the canonical conjugate is given by $\mathbf{M}$ such that $[\mathbf{A},\mathbf{M}] = i\hbar$.

$$\mathbf{M} = i\left(\frac{\hbar\epsilon_0}{V}\right)^{1/2}\sum_{k\lambda}\varepsilon_\lambda(k)\sqrt{\frac{\omega_k}{2}}\left\{\mathbf{a}_{k\lambda}^\dagger e^{-i\mathbf{k}\cdot\mathbf{x}} - \mathbf{a}_{k\lambda}e^{i\mathbf{k}\cdot\mathbf{x}}\right\} \tag{B.18}$$

The first two terms of the total hamiltonian $\mathcal{H}_{tot}$ gives the quantized photon energy.

$$\begin{aligned}H_{photon} &= \int_V \mathcal{H}_{photon} = \int_V \frac{1}{2\epsilon_0}\mathbf{M}^2 + \frac{1}{2\mu_0}(\nabla\times\mathbf{A})^2 \\ &= \hbar\sum_{k\lambda}\omega_k\left(\mathbf{a}_{k\lambda}^\dagger\mathbf{a}_{k\lambda} + \frac{1}{2}\right)\end{aligned} \tag{B.19}$$

To get the equation above, we used the identity $|\nabla\times\mathbf{A}|^2 = \sum_\alpha|\nabla\mathbf{A}^\alpha|^2 - \nabla\cdot[(\mathbf{A}\cdot\nabla)\mathbf{A}] - (\mathbf{A}\cdot\nabla)(\nabla\cdot\mathbf{A})$. The second term does not contribute to the integral and the last term is zero in the Coulomb gauge.

The polarization term is less straightforward. There are two ways from where one can define the field operators. One way is defining Π and $\mathbf{P}$ from

$$\mathcal{H}_{pol} = \frac{\epsilon_0\omega_0^2\beta}{2}\Pi^2 + \frac{1}{2\epsilon_0\beta}\mathbf{P}^2 \tag{B.20}$$

so that

$$H = \hbar\omega_0 \sum_{k\lambda} \left(\mathbf{b}^\dagger_{k\lambda} \mathbf{b}_{k\lambda} + \frac{1}{2} \right). \tag{B.21}$$

From this form of H we can deduce that

$$\mathbf{P} = \left(\frac{\hbar\epsilon_0\beta\omega_0}{2V} \right)^{1/2} \sum_{k\lambda} \varepsilon_\lambda(k) \left\{ \mathbf{b}^\dagger_{k\lambda} e^{-i\mathbf{k}\cdot\mathbf{x}} + \mathbf{b}_{k\lambda} e^{i\mathbf{k}\cdot\mathbf{x}} \right\} \tag{B.22}$$

$$\Pi = i \left(\frac{\hbar}{2\epsilon_0\beta\omega_0 V} \right)^{1/2} \sum_{k\lambda} \varepsilon_\lambda(k) \left\{ \mathbf{b}^\dagger_{k\lambda} e^{-i\mathbf{k}\cdot\mathbf{x}} - \mathbf{b}_{k\lambda} e^{i\mathbf{k}\cdot\mathbf{x}} \right\}. \tag{B.23}$$

It is easy to show that $[\mathbf{P}, \Pi] = i\hbar$. Note that we neglected spatial dispersion so that the oscillators are uncoupled and resonate at frequency ω_0. This is the path followed by Hopfield [20] and Quattropani [115]. The extra term $\frac{1}{2\epsilon_0}\mathbf{P}^2$ from Eq. (B.15) will then have the form

$$\begin{aligned} H_{extra} &= \int_V \mathcal{H}_{extra} = \int_V \frac{1}{2\epsilon_0} \mathbf{P}^2 \\ &= \frac{\hbar\beta\omega_0}{4} \sum_{k\lambda} \left(\mathbf{b}^\dagger_{k\lambda} \mathbf{b}_{k\lambda} + \mathbf{b}_{k\lambda} \mathbf{b}^\dagger_{k\lambda} + \mathbf{b}^\dagger_{k\lambda} \mathbf{b}^\dagger_{-k\lambda} + \mathbf{b}_{k\lambda} \mathbf{b}_{-k\lambda} \right). \end{aligned} \tag{B.24}$$

The second way of defining $\mathbf{P}$ and Π is by following the procedure[1] used by Kittel [114]. Kittel derived the polarization field operators using this term of the Hamiltonian density as a whole.

$$\mathcal{H}_{pol} = \frac{\epsilon_0\omega_0^2\beta}{2} \Pi^2 + \frac{1}{2\epsilon_0\beta} (1+\beta) \mathbf{P}^2 \tag{B.25}$$

Thus our canonical polarization field operators $\mathbf{P}$ and Π become

$$\mathbf{P} = \left(\frac{\hbar\omega_0\epsilon_0\beta}{2(1+\beta)^2 V} \right)^{1/2} \sum_{k\lambda} \varepsilon_\lambda(k) \left\{ \mathbf{b}^\dagger_{k\lambda} e^{-i\mathbf{k}\cdot\mathbf{x}} + \mathbf{b}_{k\lambda} e^{i\mathbf{k}\cdot\mathbf{x}} \right\} \tag{B.26}$$

$$\Pi = i \left(\frac{\hbar(1+\beta)^{1/2}}{2\epsilon_0\beta\omega_0 V} \right)^{1/2} \sum_{k\lambda} \varepsilon_\lambda(k) \left\{ \mathbf{b}^\dagger_{k\lambda} e^{-i\mathbf{k}\cdot\mathbf{x}} - \mathbf{b}_{k\lambda} e^{i\mathbf{k}\cdot\mathbf{x}} \right\} \tag{B.27}$$

[1] This is a more intuitive form and is easier when solving the eigenvalue problem. Another reason for following Kittel is to get the total Hamiltonian in the usual form we often use for coupled two level systems given by

$$H_{tot} = \sum E_{ph} \mathbf{a}^\dagger \mathbf{a} + \sum E_{pol} \mathbf{b}^\dagger \mathbf{b} + i\hbar \sum \Omega (\mathbf{b}^\dagger \mathbf{a} + h.c).$$

which gives

$$H_{pol} = \hbar\omega_0(1+\beta)^{1/2}\sum_{k\lambda}\left(\mathbf{b}^\dagger_{k\lambda}\mathbf{b}_{k\lambda}+\frac{1}{2}\right) \tag{B.28}$$

Finally, we have the interaction term given by

$$H_{inter} \;=\; \int_V \frac{\mathbf{M}\cdot\mathbf{P}}{\epsilon_0} \tag{B.29}$$

Again, following Kittel's notation, we change

$$\left(\sum_{k\lambda}\varepsilon_\lambda(k)\mathbf{a}_{k\lambda}e^{ik\cdot x}\right)\left(\sum_{k'\lambda'}\varepsilon_{\lambda'}(k')\mathbf{b}_{k'\lambda'}e^{ik'\cdot x}\right)\Rightarrow\left(\sum_{k\lambda}\mathbf{a}_{-k\lambda}\mathbf{b}_{k\lambda}\right). \tag{B.30}$$

Naturally, we also do the same for the complex conjugate. What happened here is that we change k of the photon creation operators to $-k$ and $\varepsilon_\lambda(k)\cdot\varepsilon_{\lambda'}(k') = \varepsilon_\lambda(-k)\cdot\varepsilon_{\lambda'}(k') = \delta_{kk'}\delta_{\lambda\lambda'}$ (Note that the summation is from $-k$ to k). Hence, we get the interaction term as

$$H_{inter} = i\sum_{k\lambda}\frac{\hbar\sqrt{\omega_k\omega_0}}{2}\left(\frac{\beta}{(1+\beta)^{1/2}}\right)^{1/2}\left(\mathbf{a}^\dagger_{k\lambda}\mathbf{b}_{k\lambda}-\mathbf{a}_{k\lambda}\mathbf{b}^\dagger_{k\lambda}+\mathbf{a}^\dagger_{-k\lambda}\mathbf{b}^\dagger_{k\lambda}-\mathbf{a}_{-k\lambda}\mathbf{b}_{k\lambda}\right) \tag{B.31}$$

Therefore, the total Hamiltonian becomes,

$$\begin{aligned} H_{tot} = \hbar\sum_{k\lambda}\{&\omega_k\left(\mathbf{a}^\dagger_{k\lambda}\mathbf{a}_{k\lambda}+\frac{1}{2}\right)+\omega_0(1+\beta)^{1/2}\left(\mathbf{b}^\dagger_{k\lambda}\mathbf{b}_{k\lambda}+\frac{1}{2}\right)\\ +i\frac{\sqrt{\omega_k\omega_0}}{2}&\left(\frac{\beta}{(1+\beta)^{1/2}}\right)^{1/2}\left(\mathbf{a}^\dagger_{k\lambda}\mathbf{b}_{k\lambda}-\mathbf{a}_{k\lambda}\mathbf{b}^\dagger_{k\lambda}+\mathbf{a}^\dagger_{-k\lambda}\mathbf{b}^\dagger_{k\lambda}-\mathbf{a}_{-k\lambda}\mathbf{b}_{k\lambda}\right)\} \end{aligned} \tag{B.32}$$

To diagonalize the Hamiltonian, we define a normal-mode annihilation operator

$$\alpha_k = w\mathbf{a}_k + x\mathbf{b}_k + y\mathbf{a}^\dagger_{-k} + z\mathbf{b}^\dagger_{-k} \tag{B.33}$$

where, as a normal-mode annihilation operator, it satisfies

$$[\alpha_k, H] = E_k\alpha_k \tag{B.34}$$

The solution or expansion of the previous equation leads to a set of equations which can be written in matrix form. Basically, it is an eigenvalue problem.

$$\begin{pmatrix} A & -iC & 0 & iC \\ iC & B & iC & 0 \\ 0 & iC & -A & -iC \\ iC & 0 & iC & -B \end{pmatrix} \begin{pmatrix} w \\ x \\ y \\ z \end{pmatrix} = E \begin{pmatrix} w \\ x \\ y \\ z \end{pmatrix} \tag{B.35}$$

where

$$A = \hbar\omega_k, \quad B = \hbar\omega_0(1+\beta)^{1/2}, \quad C = \frac{\hbar\sqrt{\omega_k\omega_0}}{2}\left(\frac{\beta}{(1+\beta)^{1/2}}\right)^{1/2}.$$

The determinant of the matrix gives,

$$\begin{aligned} E^4 - (A^2+B^2)E^2 + A^2B^2 - 4ABC^2 &= 0 \\ E^4 - E^2(\hbar^2\omega_k^2 + \hbar^2\omega_0^2(1+\beta)) + \hbar^2\omega_k^2\hbar^2\omega_0^2 &= 0 \end{aligned} \tag{B.36}$$

Hence

$$\frac{\hbar^2\omega_k^2}{E^2} = 1 + \frac{\hbar^2\omega_0^2\beta}{\hbar^2\omega_0^2 - E^2} \tag{B.37}$$

If we write $E = \hbar\omega$ and replace $\omega_0\beta = f$ we get back our original form of the dielectric function

$$\frac{\epsilon(\omega)}{\epsilon_0} = n^2 = \frac{\omega_k^2}{\omega^2} = 1 + \frac{f}{\omega_0^2 - \omega^2} \tag{B.38}$$

We only take the positive solutions to the determinant, in other words, positive values of energies. If we take the regime near resonance, we get the usual form of the ipper and lower polariton derived from a simple two level system.

$$E_{\substack{UP \\ LP}} = \frac{E_{phot} + E_{pol}}{2} \pm \frac{\sqrt{(E_{phot} - E_{pol})^2 + \Omega^2}}{2} \tag{B.39}$$

where $E_{phot} = \hbar\omega_k$ is the energy of the incident photon, $E_{pol} = \hbar\omega_0$ is the energy of the polarized particle and $\Omega = \sqrt{\omega_0^2\beta} = \sqrt{f}$ is the coupling constant. Actually, deriving this form the original Eq. (B.36) is not trivial. The following provides the steps to arrive at Eq. (B.39) from Eq. (B.36). We can rewrite Eq. (B.36) as

$$\omega^4 - b\omega^2 + c = 0$$

where $b = \omega_k^2 + \omega_0^2(1+\beta)$ and $c = \omega_k^2\omega_0^2$. I divided out $\hbar$ from $E = \hbar\omega$ so that it does not have to carry $\hbar$ in every step.

$$\omega = \sqrt{\frac{b}{2} \pm \frac{\sqrt{b^2 - 4c}}{2}}$$

Remember we are at close to resonance, $\omega_k \approx \omega_0$. The term $b^2 - 4c$ would be a very small number. Hence,

$$\begin{aligned} \omega &\approx \sqrt{\frac{b}{2}} \pm \frac{1}{2}\sqrt{\frac{b^2-4c}{2b}} \\ &= \sqrt{\frac{b}{2}} \pm \frac{1}{2}\sqrt{\left(b - 2\sqrt{c}\right)\frac{(b+2\sqrt{c})}{2b}} \end{aligned}$$

Substituting back b and c we have,

$$\begin{aligned} \sqrt{\frac{b}{2}} &= \sqrt{\frac{\omega_k^2 + \omega_0^2 + \omega_0^2\beta}{2}} \\ &= \sqrt{\frac{(\omega_k+\omega_0)^2 - 2\omega_k\omega_0 + \omega_0^2\beta}{2}} \\ &= \sqrt{\left(\frac{(\omega_k+\omega_0)^2}{2}\right)\left(1 - \frac{2\omega_k\omega_0 - \beta\omega_0^2}{(\omega_0+\omega_k)^2}\right)} \\ &\approx \sqrt{\left(\frac{(\omega_k+\omega_0)^2}{2}\right)\left(1 - \frac{2\omega_0^2 - \beta\omega_0^2}{4\omega_0^2}\right)} \\ &= \sqrt{\left(\frac{(\omega_k+\omega_0)^2}{2}\right)\left(1 - \frac{2-\beta}{4}\right)} \\ &\approx \sqrt{\left(\frac{(\omega_k+\omega_0)^2}{2}\right)\left(1 - \frac{1}{2}\right)} \\ &= \frac{\omega_k + \omega_0}{2} \end{aligned}$$

The assumption used here is that the coupling term $\beta = f/\omega_0$ is much smaller than 1.

The other term is easy enough.

$$b - 2\sqrt{c} = (\omega_0 - \omega_k)^2 + \beta\omega_0^2 = (\omega_0 - \omega_k)^2 + \Omega^2$$

Finally,

$$\begin{aligned}
\frac{b+2\sqrt{c}}{2b} &= \frac{1}{2}+\frac{\sqrt{c}}{b} \\
&= \frac{1}{2}+\frac{\omega_k\omega_0}{\omega_k^2+\omega_0^2+\beta\omega_0^2} \\
&\approx \frac{1}{2}+\frac{\omega_0^2}{2\omega_0^2+\beta\omega_0^2} \\
&= \frac{1}{2}+\frac{1}{2+\beta} \\
&\approx 1
\end{aligned}$$

Putting the $\hbar$ factor to the ω's and plugging back everything together we get the usual form of the upper and lower polariton equation.

$$E_{\substack{UP\\LP}} = \frac{E_{phot}+E_{pol}}{2} \pm \frac{\sqrt{(E_{phot}-E_{pol})^2+\Omega^2}}{2} \tag{B.40}$$

APPENDIX C

MICROCAVITY STRUCTURE

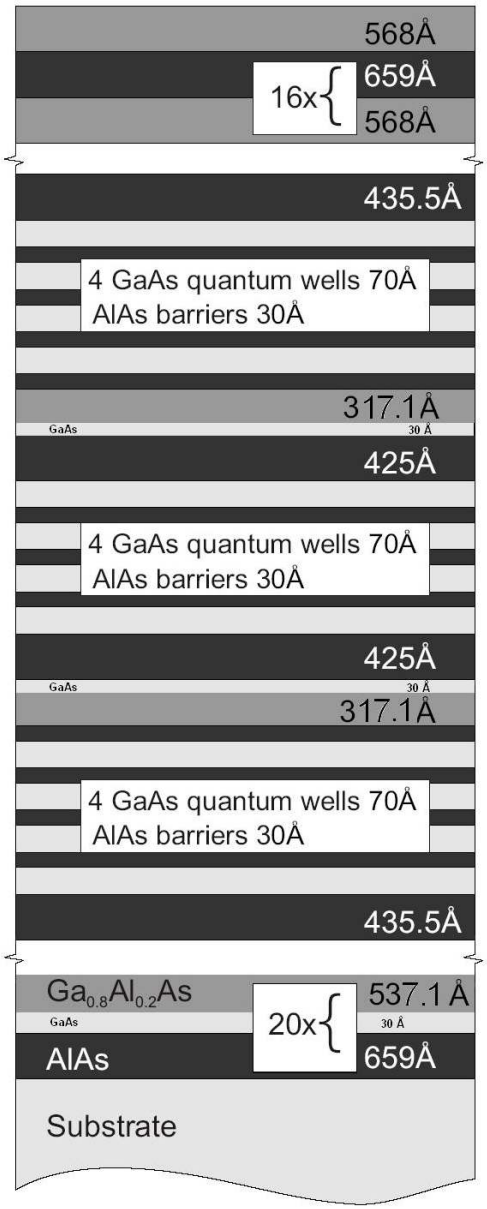

Figure C1: Layer structure of the semiconductor microcavity sample used in all the experiments.

APPENDIX D

DENSITY OF STATES FOR A *D*-DIMENSIONAL POWER LAW TRAP

As pointed out by many authors (e.g. Ref. [57]), BEC is also possible for low-dimensions in trapped geometries. Calculating the density of states for a given geometry is essential in finding the critical density for BEC. The two dimensional case is, of course, more useful in this dissertation but a general treatment of the density of states is handy when comparing the different cases. Power law traps are considered here mainly because it is relevant in this study. Anyhow, most traps can be approximated by a power law function near the minimum. In addition, using power law traps lead to analytical solutions for the critical density. The density of states will be solved semiclassically as traps commonly used in BEC are weakly confining which means that the energy level spacing is much smaller than the thermal energy of the particles.

The density of states is defined by $\rho(E) = N'(E)$ where $N(E)$ is the number of states with energy less than E. Semiclassically, apart from the constant in the denominator, the integral

$$N(E) = \int\int_{\frac{p^2}{2m}+V(r)<E} \frac{\mathrm{d}^d\mathbf{r}\ \mathrm{d}^d\mathbf{p}}{(2\pi\hbar)^d} \tag{D.1}$$

basically calculates the volume of a d-dimensional sphere of radius $\tilde{r}(\tilde{p})$. Hence, [1]

[1] The author recomends Ref. [118] for those interested in following the algebra in solving this integral.

$$
\begin{aligned}
N(E) &= \frac{1}{(2\pi\hbar)^d}\int_0^{\tilde{r}} \mathrm{d}^d\mathbf{r}\int_0^{\tilde{p}} \mathrm{d}^d\mathbf{p} \\
&= \frac{1}{(2\pi\hbar)^d}\left(\frac{2\pi^{d/2}}{\Gamma(d/2)}\right)^2 \int\int_{\frac{p^2}{2m}+V(r)<E} \mathrm{d}\tilde{r}\mathrm{d}\tilde{p}\ \tilde{r}^{d-1}\tilde{p}^{d-1}
\end{aligned}
\tag{D.2}
$$

where $\tilde{r}$ and $\tilde{p}$ are the maximum radius and momentum respectively. The maximum energy

$$
E = \frac{\tilde{p}^2}{2m} + \alpha\tilde{r}^n
$$

can be written in this form

$$
1 = \frac{\tilde{p}^2}{2mE} + \frac{\alpha}{E}\,\tilde{r}^n. \tag{D.3}
$$

To simplify the calculation, let

$$
p = \frac{\tilde{p}^2}{2mE} \quad \text{and} \quad r = \tilde{r}\left(\frac{\alpha}{E}\right)^{1/n}
$$

such that

$$
1 = p^2 + r^n = p^2 + (r^2)^{n/2}. \tag{D.4}
$$

$$
\begin{aligned}
N(E) &= \frac{1}{(2\pi\hbar)^d}\left(\frac{2\pi^{d/2}}{\Gamma(d/2)}\right)^2 \int\int_{p^2+r^n<1} \mathrm{d}\tilde{r}\mathrm{d}\tilde{p}\ \tilde{r}^{d-1}\tilde{p}^{d-1} \\
&= C\int\int_{p^2+r^n<1} \mathrm{d}r\mathrm{d}p\ r^{d-1}p^{d-1} \\
&\quad \text{where}\ \ C = \frac{1}{(2\pi\hbar)^d}\left(\frac{2\pi^{d/2}}{\Gamma(d/2)}\right)^2 \frac{1}{\alpha^{d/n}}(2m)^{d/2}E^{(d/n+d/2)} \\
&= \frac{C}{4}\int\int_{p^2+r^n<1} dr^2dp^2(r^2)^{d/2-1}(p^2)^{d/2-1}
\end{aligned}
$$

Again, we can simplify the equation by introducing a change of variables $x = r^2$ and $y = p^2$. Therefore,

$$\begin{aligned} N(E) &= \frac{C}{4}\int_0^1 dx x^{d/2-1}\int_0^{1-x^{n/2}} dy y^{d/2-1} \\ &= \frac{C}{4}\frac{d}{2}\int_0^1 dx x^{d/2-1}(1-x^{n/2})^{d/2} \\ &= \frac{C}{4}\frac{d}{2}\frac{2}{n}\frac{\Gamma(1+d/2)\Gamma(d/n)}{\Gamma(1+d/2+d/n)} \\ &= \frac{(2m)^{d/2}}{(2\hbar\alpha^{1/n})^d}\left(\frac{d}{2}\right)\frac{\Gamma(d/n+1)}{\Gamma(d/2)\Gamma(d/2+d/n+1)}E^{d/2+d/n} \end{aligned} \tag{D.5}$$

Finally, we can calculate for the density of states $\rho(E) = N'(E)$ for a d-dimensional system in a power law potential.

$$\rho(E) = \frac{(2m)^{d/2}}{(2\hbar\alpha^{1/n})^d}\left(\frac{d}{2}\right)\frac{\Gamma(d/n+1)}{\Gamma(d/2)\Gamma(d/2+d/n)}E^{d/2+d/n-1} \tag{D.6}$$

APPENDIX E

PIKUS-BIR HAMILTONIAN AND EXCHANGE TERM

The valence band energy shifts as a function of stresses is given by the Pikus-Bir deformation Hamiltonian[77]:

$$H_{PB} = a(\epsilon_{xx} + \epsilon_{yy} + \epsilon_{zz}) + b[(J_x^2 - J^2/3)\epsilon_{xx} + c.p.] + \frac{2d}{\sqrt{3}}\left[\frac{1}{2}(J_xJ_y + J_yJ_x)\epsilon_{xy} + c.p.\right] \quad \text{(E.1)}$$

where a, b, and d are deformation potentials, ϵ_{ij}'s are stress-tensor components, J's are the angular momentum operators acting on the spin states of the valence band ($m = 3/2$, $1/2$, $-1/2$, and $-3/2$), and $c.p.$'s correspond to cyclic permutations with respect to x, y, z. Relevant material properties, *e.g.* deformation potentials and elastic constants, used in our simulations are found in Refs. [78, 49, 79]. Acting on heavy-hole and light-hole basis, $\left|\frac{3}{2}, \frac{3}{2}\right\rangle, \left|\frac{3}{2}, \frac{1}{2}\right\rangle, \left|\frac{3}{2}, -\frac{1}{2}\right\rangle, \left|\frac{3}{2}, -\frac{3}{2}\right\rangle$, Eq. (E.1) gives the matrix form[78, 53] of the Pikus-Bir Hamiltonian

$$H_{PB} = -\begin{pmatrix} P+Q & -S & R & 0 \\ -S^* & P-Q & 0 & R \\ R^* & 0 & P-Q & -S \\ 0 & R^* & S^* & P+Q \end{pmatrix} \quad \text{(E.2)}$$

where

$$P = -a_v\left(\varepsilon_{xx} + \varepsilon_{yy} + \varepsilon_{zz}\right) \quad , \quad Q = -\frac{b}{2}\left(\varepsilon_{xx} + \varepsilon_{yy} - 2\varepsilon_{zz}\right),$$
$$R = \frac{\sqrt{3}}{2}b\left(\varepsilon_{xx} - \varepsilon_{yy}\right) - id\varepsilon_{xy} \quad , \quad S = -d\left(\varepsilon_{xz} - i\varepsilon_{yz}\right).$$

Diagonalizing this the matrix gives the shift of the valence band energies. The shift of the conduction band is given simply by $\Delta E_c = a_c\,(\varepsilon_{xx} + \varepsilon_{yy} + \varepsilon_{zz})$.

Of course, to be able to diagonalize H_{PB} through out the sample, we need the values for the strain at different points on the sample as we stress it (see Refs. [80, 40]to stressor geometry). The strain terms, ε_{xx}, ε_{yy}, *etc.*, could be computed using programs that could do finite-element analysis (*e.g.* ANSYS). Finite-element analysis numerically calculates the displacements of a discretized mesh-representation of the sample using the constitutive relations of GaAs [53]. We begin by calculating the equilibrium displacement of the mesh points by solving Newton's law for continuous media. Following notation from Ref. [53], we have

$$\sum_j \frac{\partial \sigma_{ij}}{\partial x_j} = \rho \ddot{u}_i, \tag{E.3}$$

where ρ is the density of GaAs and u_i is the diplacement of a volume element in the i direction. Combining this with Hooke's law, $\sigma_{ij} = \sum_{lm} C_{ijlm}\varepsilon_{lm}$, we get

$$\rho \ddot{u}_i = \sum_{jlm} C_{ijlm} \frac{\partial^2 u_l}{\partial x_j \partial x_m}, \tag{E.4}$$

where we define

$$\varepsilon_{lm} = \frac{1}{2}\left(\frac{\partial u_l}{\partial x_m} + \frac{\partial u_m}{\partial x_l}\right).$$

Eq. E.4 is discretized and applied to all points of the constructed mesh representation of the sample when doing the actual simulation. A force on the stressor pin, for example, corresponds to a displacement of the mesh points under the stressor. The right hand side of Eq. E.4 calculates the force felt by the other mesh points, due the initial displacement. The next iteration then is a displacement of each mesh point, in the same direction as the force, with magnitude proportional to the force felt by each point. After the displacement, the force is again calculated. The process repeats until equilibrium is reached. From the equilibrium displacements (u_i's), one can calculate the strain terms, ε_{xx}, ε_{yy}, *etc.*, that goes into H_{PB}.

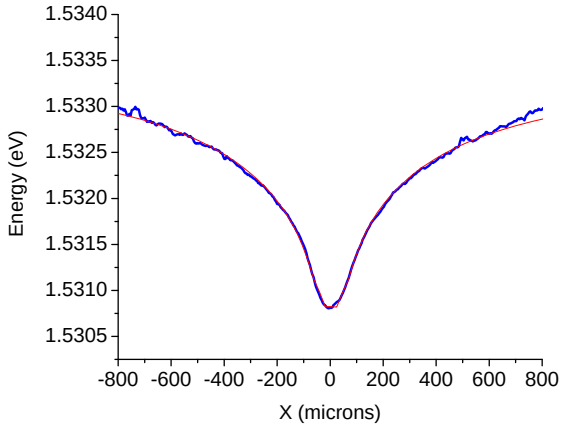

Figure E1: Example of a fit using strain simulations from ANSYS (red curve) on a single quantum well energy of a stressed double quantum well (blue curve, 0.7 N force on pin stressor), for an experiment similar to a work done previously [80]. The following book values (*e.g.* Ref. [78]) for the deformation potentials of GaAs were used for these fits: $a_c = -7.17$ eV, $a_v = 1.16$ eV, $b = -1.7$ eV, $d = -4.55$ eV.

The Hamiltonian that can split the degeneracy of the two bright states is the short-range electron-hole exchange interaction between a hole with spin S_h and an electron with spin S_h[106].

$$H_{exch} = -\sum_{i=x,y,z} a_i S_{h,i} S_{e,i} \tag{E.5}$$

where the a's are the coupling constants. The first exchange term acting on hole-electron basis, $\left|\frac{3}{2}\right\rangle|\uparrow\rangle$, $\left|\frac{3}{2}\right\rangle|\downarrow\rangle$, $\left|\frac{1}{2}\right\rangle|\uparrow\rangle$, $\left|\frac{1}{2}\right\rangle|\downarrow\rangle$, $\left|-\frac{1}{2}\right\rangle|\uparrow\rangle$, $\left|-\frac{1}{2}\right\rangle|\downarrow\rangle$, $\left|-\frac{3}{2}\right\rangle|\uparrow\rangle$, $\left|-\frac{3}{2}\right\rangle|\downarrow\rangle$, gives

$$-\begin{pmatrix}
\frac{a_z}{4} & 0 & 0 & \frac{-(a_x-a_y)}{\sqrt{3}} & 0 & 0 & 0 & 0 \\
0 & -\frac{a_z}{4} & \frac{-(a_x+a_y)}{\sqrt{3}} & 0 & 0 & 0 & 0 & 0 \\
0 & \frac{-(a_x+a_y)}{\sqrt{3}} & \frac{a_z}{12} & 0 & 0 & \frac{2(a_x-a_y)}{3} & 0 & 0 \\
\frac{-(a_x-a_y)}{\sqrt{3}} & 0 & 0 & -\frac{a_z}{12} & \frac{2(a_x+a_y)}{3} & 0 & 0 & 0 \\
0 & 0 & 0 & \frac{2(a_x+a_y)}{3} & -\frac{a_z}{12} & 0 & 0 & \frac{-(a_x-a_y)}{\sqrt{3}} \\
0 & 0 & \frac{2(a_x-a_y)}{3} & 0 & 0 & \frac{a_z}{12} & \frac{-(a_x+a_y)}{\sqrt{3}} & 0 \\
0 & 0 & 0 & 0 & 0 & \frac{-(a_x+a_y)}{\sqrt{3}} & -\frac{a_z}{4} & 0 \\
0 & 0 & 0 & 0 & \frac{-(a_x-a_y)}{\sqrt{3}} & 0 & 0 & \frac{a_z}{4}
\end{pmatrix} \tag{E.6}$$

The exchange term is added to the Pikus-Bir deformation matrix to account for the shift of the bands due to both exchange and deformation. The Pikus-Bir Hamiltonian, acting in

the same basis state as the exchange, gives

$$H_{PB} = -\begin{pmatrix} P+Q & 0 & -S & 0 & R & 0 & 0 & 0 \\ 0 & P+Q & 0 & -S & 0 & R & 0 & 0 \\ -S^* & 0 & P-Q & 0 & 0 & 0 & R & 0 \\ 0 & -S^* & 0 & P-Q & 0 & 0 & 0 & R \\ R^* & 0 & 0 & 0 & P-Q & 0 & S & 0 \\ 0 & R^* & 0 & 0 & 0 & P-Q & 0 & S \\ 0 & 0 & R^* & 0 & S^* & 0 & P+Q & 0 \\ 0 & 0 & 0 & R^* & 0 & S^* & 0 & P+Q \end{pmatrix}. \quad \text{(E.7)}$$

Diagonalizing $H_{PB} + H_{exch}$ at every point of a numerically discretized mesh of GaAs gives you the shifted band energies at every point of the mesh, with stress.

The heavy hole excitons are those with the valence-band 3/2 states, while the light-hole excitons are those with the valence-band 1/2 states. Only the states with J = 1 are bright states, i.e. states $\left|\frac{3}{2}\right\rangle|\downarrow\rangle$, $\left|-\frac{3}{2}\right\rangle|\uparrow\rangle$ for the heavy holes, and states $\left|\frac{1}{2}\right\rangle|\uparrow\rangle$, $\left|-\frac{1}{2}\right\rangle|\downarrow\rangle$ for the light holes. The radiative oscillator strength for each eigenstate is proportional to $|\langle vac|p|i\rangle|^2$, where

$$\begin{aligned} |i\rangle = \quad & \alpha_1 |hh,2\rangle + \alpha_2 |hh,1\rangle + \alpha_3 |lh,1\rangle + \alpha_4 |lh,0(a)\rangle \\ & + \alpha_5 |lh,0(b)\rangle + \alpha_6 |lh,-1\rangle + \alpha_7 |hh,-1\rangle + \alpha_8 |hh,-2\rangle \end{aligned} \quad \text{(E.8)}$$

is the eigenstate found in the above electron-hole basis. The matrix elements $\langle vac|p|hh,\pm 1\rangle = M_{hh}$ and $\langle vac|p|lh,\pm 1\rangle = M_{lh}$ are fit parameters and the other matrix elements are zero.

APPENDIX F

TRANSFER MATRIX SIMULATION CODE

```
(* Description: modifying reflectivitytester.nb by rearranging the \
order of how the transfer and interface matrices are made. This uses \
Dr. D. W. Snoke's method (from his book) of transfer matrices

TEST 2 uses the SPECS sent by Gregor Weihs WITH 30 Angs GaAs inserted \
in the GaAlAs layers
Sample 4_20_05.1 Specifications

This is the working version with Quantum Well resonance. Revised for \
normal incidence only.
*)

(*Remove["Global`*"];Off[General::"spell"];*)

<< PhysicalConstants`;
<< PlotLegends`;

kb = (BoltzmannConstant/ElectronCharge )[[1]];
h = PlanckConstant[[1]];
c = SpeedOfLight[[1]];
```

```
q = ElectronCharge[[1]];

(* Test Parameters *)

(*
Center PThick
PThick =0.968;
*)(* Increasing thickness of each layer by some percent *)
T = 4.0; (* Temperature is 4K *)
(* \[Theta]=0*\[Pi]/180;  Incoming wave angle *)
\[Lambda]C = 777.0*10^-9;

(* AlGaAs Refractive Index Model by Gehrsitz et. al.*)
(*
n[x_,\[Lambda]_,T_]:=Module[{conv,E\[Lambda],AGaAs,E1GaAs,E\
\[CapitalGamma]GaAs,R,A,C1,E1,C0,E0},
conv=1/1.239856; (*For converting energy in terms of (\[Mu]m)^-1*)
E\[Lambda]=h*c/(q*\[Lambda])*conv;
AGaAs=5.9613+7.178*10^-4T-0.953*10^-6T^2;
E1GaAs=4.7171-3.237*10^-4T-1.358*10^-6T^2;
E\[CapitalGamma]GaAs=(1.5192+1.8*15.9*10^-3(1-Coth[(15.9*10^-3)/(2*kb*\
T)])+1.1*33.6*10^-3(1-Coth[(33.6*10^-3)/(2*kb*T)]))*conv;

R=((1-x)1.55*10^-3)/(0.724*10^-3-E\[Lambda]^2)+(x*2.61*10^-3)/(1.331*\
10^-3-E\[Lambda]^2);
A=AGaAs-16.159*x+43.511*x^2-71.317*x^3+57.535*x^4-17.451*x^5;
C1=21.5647+113.74*x-122.5*x^2+108.401x^3-47.318*x^4;
E1=E1GaAs+11.006*x-3.08*x^2;
C0=(50.535-150.7*x-62.209*x^2+797.16*x^3-1125*x^4+503.79*x^5)^(-1);
E0=E\[CapitalGamma]GaAs+1.1308*x+0.1436*x^2;
```

```
Sqrt[A+C0/(E0^2-E\[Lambda]^2)+C1/(E1-E\[Lambda]^2)+R]
]

*)
(* AlGaAs Refractive Index Model by Afromowitz for Room Temperature \
Measurements ONLY *)
(*
n[x_,\[Lambda]_, T_]:=Module[{E\[Lambda],E0,Ed,E\[CapitalGamma],Ef,\
\[Eta],M1, M3,\[Chi] },

E\[Lambda]=h*c/(q*\[Lambda]);
E0=3.65 + 0.871*x  + 0.179*x^2;
Ed = 36.1 - 2.45*x;
E\[CapitalGamma]=1.424  + 1.266 *x  + 0.26*x^2;
Ef=Sqrt[2.0*E0^2-E\[CapitalGamma]^2];
\[Eta] = (\[Pi] * Ed)/(2.0*E0^3*(E0^2-E\[CapitalGamma]^2));
M1 = \[Eta]/(2.0*\[Pi])*(Ef^4-E\[CapitalGamma]^4);
M3 = \[Eta]/\[Pi]*(Ef^2-E\[CapitalGamma]^2);
\[Chi]= M1 +M3*E\[Lambda]^2+\[Eta]/\[Pi]*E\[Lambda]^4*Log[(Ef^2-E\
\[Lambda]^2)/(E\[CapitalGamma]^2-E\[Lambda]^2)];
Sqrt[\[Chi]+1.0]
]
*)

(*N for quantum Well Resonance*)
nGaAsRes[\[Lambda]_, T_, Ex_, f_] :=
 Module[{ E\[Lambda], ExEn, er, ei, n, k, \[CapitalGamma]},
  E\[Lambda] = 1000*h*c/(q*\[Lambda]);(*the units is in meV*)
  ExEn = (1000.0*h*c/(q*Ex*10^-9));
```

```
  (*** Modified indices ***)
  (*f=0.00625;*)
  \[CapitalGamma] = 0.2; (*units of meV*)

  er = 12.96 + (
    f*ExEn^2*(ExEn^2 - E\[Lambda]^2))/((ExEn^2 -
       E\[Lambda]^2)^2 + (\[CapitalGamma]*E\[Lambda])^2);
  ei = (f*ExEn^2*\[CapitalGamma]*
    E\[Lambda])/((ExEn^2 - E\[Lambda]^2)^2 + (\[CapitalGamma]*
      E\[Lambda])^2);
  n = 1/Sqrt[2]*((er^2 + ei^2)^(1/2) + er)^(1/2);
  k = 1/Sqrt[2]*((er^2 + ei^2)^(1/2) - er)^(1/2);
  n + \[ImaginaryI]*k

  ]

(* Jackson Method *)

Reflectivity[\[Lambda]_, nlist_, dlist_] :=
 Block[{layer, kmz, \[CapitalDelta], Dm, Pm, Transfer},
  layer = Length[nlist];
  (*ky=2\[Pi]*nlist[[1]]/\[Lambda] *Sin[\[Theta]];*)
  (*kmz[nm_]:=Sqrt[(2\[Pi]*nm/\[Lambda])^2-ky^2];*)
  kmz[nm_] := Sqrt[(2 \[Pi]*nm/\[Lambda])^2];
  \[CapitalDelta][nm_, nm1_] := kmz[nm]/kmz[nm1];
  Dm[nm_, nm1_] := ( {
      {1 + \[CapitalDelta][nm, nm1], 1 - \[CapitalDelta][nm, nm1]},
      {1 - \[CapitalDelta][nm, nm1], 1 + \[CapitalDelta][nm, nm1]}
     } )/2;
  Pm[nm_, dm_] := ( {
```

```
     {Exp[\[ImaginaryJ]*kmz[nm]*dm], 0},
     {0, Exp[-\[ImaginaryJ]*kmz[nm]*dm]}
    } );

  Transfer = IdentityMatrix[2];

  Transfer =
   Dm[nlist[[1]], nlist[[2]]].Pm[nlist[[1]], nlist[[1]]].Transfer;

  Do[
   Transfer =
    Dm[nlist[[q]], nlist[[q + 1]]] .Pm[nlist[[q]],
      dlist[[q]]].Transfer
   , {q, 2, layer - 1}];

  (Abs[Transfer[[2, 1]]/Abs[Transfer[[2, 2]]])^2
  ]

SetDirectory[
  "C:\\Documents and \
Settings\\Administrator\\Desktop\\RyanTempFile"];
(*ExList = Import["mar13_1DeducedExlPixel46-465.DAT","TSV"];*)

Clear[\[Lambda]];
(*range={\[Lambda],765.0*10^-9,778.0*10^-9,0.5*10^-9}; (* Wavelength \
range and increment *)
\[Lambda]list=Table[\[Lambda],Evaluate[range]]; *)
\[Lambda]list = Table[764.986 + 0.0140196*i, {i, 929}]*10^-9;

(* Variables for the excitong splitting fit from ArchiveJournal...
```

```
13Mar08_ExcitonSplittingFunction *)
xc =  256.9533;
A1 = 0.05;
A2 = -0.02376;
w1 = 156.37108;
w2 = 44.27311;
(* Difference in energy of the two stressed induced exciton states *)

ExDiff =
  Table[0.00036 + (A1/(w1*Sqrt[Pi/2]))*
      Exp[-2*((x - xc)/w1)^2] + (A2/(w2*Sqrt[Pi/2]))*
      Exp[-2*((x - xc)/w2)^2], {x, 46, 465, 1}]*1000;

PThick = Table[0.966 + (45 + i - 50)*0.0016/500 , {i, 420}];

R = {}; (* The reflectivity list *)
TopMirror = {};
BotMirror = {};

(*layer=105;*)

(*I Moved the Thickness List Here So That The Program Goes Faster*)
LAir = 4*\[Lambda]C*10^9/4;
dlist = {LAir, 57.94};
Do[dlist = Join[dlist, {67.22, 57.94}], {16}];
dlist = Join[dlist, {44.22}];
Do[dlist = Join[dlist, {7.00, 3.0}], {4}];
dlist = Join[dlist, {32.34, 3.0, 43.35, 7.00}];
Do[dlist = Join[dlist, {3.00, 7.00}], {3}];
dlist = Join[dlist, {43.35, 3.0, 32.34}];
```

```
Do[dlist = Join[dlist, {3.00, 7.00}], {4}];
dlist = Join[dlist, { 44.42}];
Do[dlist = Join[dlist, {54.78, 3.0, 67.22}], {20}];
dlist = Join[dlist, {700.0}];
LGaAs = 5*\[Lambda]C*10^9/(4*n00);
dlist = Append[dlist, LGaAs];
dlist = dlist*1.0*10^-9;
(*************************************************************)

 (* if the values of n20 = 3.6, n100 = 3.08, and n00 = 3.65 , it came \
from S.Pau et al., Phys. Rev. B., Vol. 51, No. 20 1995*)

(* Values of the refractive indices at 777 nm and 4 Kelvin using \
Gerhsitz et. al.
Here I made them constant around the region of interest just to move \
the simulation faster *)
n20 = 3.45078;(*  Refractive index of Subscript[Al, \
0.20]Subscript[Ga, 0.80]As *)
n100 = 2.97045;(*   Refractive index of AlAs *)
n00 = 3.58944; (* Refractive index of GaAs *)
(*************************************************************)
(* Building the refractive index and the thickness lists *)
(* First layer is air, second is AlGaAs *)
TopMirror = {1.0, n20};
(* LAir=4*\[Lambda]C*10^9/4;
dlist={LAir,57.94}; *)

(* Top DBR 16 Layers AlAs-Subscript[Al, 0.20]Subscript[Ga, 0.80]As *)

Do[TopMirror = Join[TopMirror, { n100, n20}], {16}];
```

```
(*Do[dlist=Join[dlist,{67.22,57.94}],{16}]; *)

(* Spacer *)
TopMirror = Join[TopMirror, {n100}];
(*dlist=Join[dlist,{44.22}]; *)

(***
.
.
.
***)

(* Spacer *)
BotMirror = {n100};
(*dlist=Join[dlist,{ 44.42}];*)

(* Bottom DBR 20 Layers Subscript[Al, 0.20]Subscript[Ga, \
0.80]As-GaAs-AlAs *)
Do[BotMirror = Join[BotMirror, {n20, n00, n100}], {20}];
(*Do[dlist=Join[dlist,{54.78,3.0,67.22}],{20}];*)

(* The last layer is the bulk GaAs *)
BotMirror = Join[BotMirror, {n00}];
(*dlist=Join[dlist,{700.0}]; *)

(* GaAs Substrate *)
BotMirror = Join[BotMirror, {n00}];
(* LGaAs =5*\[Lambda]C*10^9/(4*n00);
dlist=Append[dlist,LGaAs];
```

```
dlist=dlist*1.0*10^-9*PThick; *)
(*****************************************************************)

(*n20=n[0.20,\[Lambda],T];  (*Refractive index of Subscript[Al, \
0.20]Subscript[Ga, 0.80]As *)
n100=  n[1.0,\[Lambda],T];  (*Refractive index of AlAs *)
n00=n[0.0,\[Lambda],T]; (* Refractive index of GaAs *) *)
nQW = 2; (*Just for initialization *)

nlist = TopMirror;

(* 4 Quantum wells *)
Do[nlist = Join[nlist, {nQW, n100}], {4}];
(*Do[dlist=Join[dlist,{7.00,3.0}],{4}]; *)

(* Spacer *)
nlist = Join[nlist, {n20, n00, n100, nQW}];
(*dlist=Join[dlist,{32.34,3.0,43.35, 7.00}]; *)

(* 3 Quantum wells *)
Do[nlist = Join[nlist, {n100, nQW}], {3}];
(*Do[dlist=Join[dlist,{3.00,7.00}],{3}]; *)

(* Spacer *)
nlist = Join[nlist, {n100, n00, n20}];
(*dlist=Join[dlist,{43.35,3.0, 32.34}]; *)

(* 4 Quantum wells *)
Do[nlist = Join[nlist, {n100, nQW}], {4}];
(*Do[dlist=Join[dlist,{3.00,7.00}],{4}]; *)
```

```
nlist = Join[nlist, BotMirror];

y0 = 767.19055;
mslope = 0.00076;
A1 = 1142.08324;
w1 = 205.39376;
xc = 209.75365;
A2 = 2.1992;
w2 = 26.94719;

For [FileNum = 0, FileNum < 6, FileNum = FileNum + 1,
  coup = 0.00600;
  RSeparated1 = {};
  RSeparated2 = {};
  ExList =
   Table[y0 + 0.0015*0.25*FileNum*y0 + mslope*x +
     0.20*FileNum*(2*A1*w1/Pi/(4*(x - xc)^2 + w1^2) +
        A2*Exp[-((x - xc)/w2)^2]), {x, 1, 420, 1}];

  For[ctr = 0, ctr < 2, ctr++,
   coup = coup + ctr*0.0001*FileNum/5.0;
   Ex = ExList + ctr*0.20*FileNum*ExDiff; (*
   Splitting of the Exciton changes with stress *)

   (*For[m=1,m<Length[\[Lambda]list]+1,m=m+40,*)
   For[m = 600, m < 900 + 1, m = m + 1,
    (*If [m==200, m =650]; (*Skip areas with no features*) *)
    \[Lambda] = \[Lambda]list[[m]];
```

```
 For[YPix = 1, YPix < 421, YPix = YPix + 1,

  nQW = nGaAsRes[\[Lambda], T, Ex[[YPix]], coup];
  (*Quantum Wells*)
  nlist[[36]] = nQW;
  nlist[[38]] = nQW;
  nlist[[40]] = nQW;
  nlist[[42]] = nQW;

  nlist[[47]] = nQW;
  nlist[[49]] = nQW;
  nlist[[51]] = nQW;
  nlist[[53]] = nQW;

  nlist[[58]] = nQW;
  nlist[[60]] = nQW;
  nlist[[62]] = nQW;
  nlist[[64]] = nQW;



  (*PThick=0.967+ (45+YPix-50)*0.002/
  410;*) (*Center at YPix 255 Corresponding to PThick = 0.968*)
  (*R=Append[R,{\[Lambda]*10^9, YPix,
  Reflectivity[\[Lambda],\[Theta],nlist,dlist*PThick]}];*)
  R =
   Append[R,
    Reflectivity[\[Lambda], nlist, dlist*PThick[[YPix]] ]];
  ];
 ];
If[RSeparated1 == {}, RSeparated1 = R, RSeparated2 = R];
```

```
   R = {};
   ];
  RSeparated1 = Partition[RSeparated1, 420];
  RSeparated2 = Partition[RSeparated2, 420];
  Export["aug07_Sep1" <> "Stress" <> ToString[FileNum] <> "Ver9.DAT",
   Transpose[RSeparated1], "TSV"];
  Export["aug07_Sep2" <> "Stress" <> ToString[FileNum] <> "Ver9.DAT",
   Transpose[RSeparated2], "TSV"];
  ];

(*SetDirectory["C:\\temp\\ArchiveJournal\\25Sep2008\\13Mar08"];
RSeparated1 = Import["mar13_Separated1Stress1.DAT","TSV"];
RSeparated2 = Import["mar13_Separated2Stress1.DAT","TSV"];*)

(*Animate[MatrixPlot[Sin[a]^2*Transpose[RSeparated2]+Cos[a]^2*\
Transpose[RSeparated1],ColorFunction->"GrayTones", \
PlotRange->{Automatic,{100,150},{0,1.05}}],{a,0,Pi}]*)


(*Animate[MatrixPlot[Sin[a]^2*Transpose[RSeparated2]+Cos[a]^2*\
Transpose[RSeparated1],ColorFunction->"Rainbow", \
PlotRange->{Automatic,{20,80},Automatic}],{a,0,Pi}]*)

(*MatrixPlot[(Transpose[RSeparated2]+Transpose[RSeparated1])/2,\
ColorFunction->"GrayTones", \
PlotRange->{Automatic,{140,160},{0,1.05}}]*)

(*Animate[ListPlot[{RDat[[1,All]],Sin[a]^2*RDat[[2,All]]+Cos[a]^2*\
RDat[[3,All]]}, Joined->True, PlotRange \
->{Automatic,{0,1.01}}],{a,0,Pi}] *)
```

```
(*ListDensityPlot[RDat,InterpolationOrder->3,ColorFunction->\
"GrayTones", PlotRange->{Automatic,{1,512},{0,1.05} }, AspectRatio -> \
0.551]*)

(*<<Graphics`Animation`

ShowAnimation[Table[ListDensityPlot[Sin[a]^2*RSeparated1+Cos[a]^2*\
RSeparted2,InterpolationOrder->3,ColorFunction->"GrayTones", \
PlotRange->{Automatic,Automatic,{0,1.05} }],{a,0,Pi}]]*)
```

APPENDIX G

MATLAB CODE FOR STRESS ANALYSIS

G.1 FUNCTION FOR PIKUS-BIR AND EXCHANGE CALCULATION

```
function StressExchangeUsingANSYSdata(StressOn, xf, yf, zf, u1 , u2, v1,
v2, w1, w2)

global StrainDat Emat ExchE OscStrength1 OscStrength2 HydroTerm vcenter
vside1 SimXaxis exx eyy ezz exy exz eyz

% Here I separated the Oscillator strength for the Right (OscStrength1)
% and Left (OscStrength2) Circular polarizations

% ImportantParameters For GaAs and AlAs
% from Table K.1 & K.2 of Physics of Optoelectronic Devices by S.L. Chuang

% band gap in units of eV
    EgGa = 1.519;
    EgAl = 3.13;
    EovavGa = -6.92;   % absolute energy level scale obtained from theory
    EovavAl = -7.49;   % absolute reference energy level useful for
                       % deriving band lineups
```

```
% split-orbit splitting energy
    DeltaGa = 0.34;
    DeltaAl = 0.28;

% constants
    e = 1.602E-19;  %electron charge in Coulombs
    me = 9.11E-31;  %electron mass in kg
    hbar= 6.626E-34/(2*pi);  %hbar in J.s
    mcGa = 0.067;   %elec. mass, indirect band gap, Eg(X) value, mcGa/me
    mcAl = 0.15;    %elec. mass, indirect band gap, Eg(X) value, mcAl/me
    epsilono = 8.85E-12;    %electric permittivity constant in F/m
    epsilon = 13.1*epsilono;    %dielectric constant og GaAs

% well width

    L = 8.475E-9; %QW width in units of m
    lhf = 1.0; %adjust factor at which light hole is smaller in energy
    kz = pi/L;

% Luttinger Parameters
    gamma1Ga = 6.8;
    gamma2Ga = 1.9;
    gamma3Ga = 2.73;

    gamma1Al = 3.45;
    gamma2Al = 0.68;
    gamma3Al = 1.29;

% Deformation Potentials (eV)
```

```
    acGa = -7.17;
    avGa =  1.16;
    bGa = -1.7;
    dGa = -4.55;

    acAl = -5.64;
    avAl = 2.47;
    bAl = -1.5;
    dAl = -3.4;

% Elastic Stiffness Tensor (10^11 dyne/cm^2) at low temp
    C11Ga = 12.11;
    C12Ga = 5.48;
    C44Ga = 6.04;

    C11Al = 12.5;
    C12Al = 5.34;
    C44Al = 5.42;

%-----------------------------------------------------------%
%-----Everything below this point changes with stress-----%
%-----------------------------------------------------------%

% note: I didn't include the center because it's a singularity
% center points are from r=0 to ri/n1=0.03/4 = 0.0075

StrainDat=dlmread('C:ANSYSsims\OffCenter4o3NFitDat10.txt');

SimXaxis = 1000*[-flipud(StrainDat(:,1)); StrainDat(:,1)]+2.5;
```

```
exx = [flipud(StrainDat(:,2)); StrainDat(:,2)];
eyy = [flipud(StrainDat(:,3)); StrainDat(:,3)];
%ezz = [flipud(StrainDat(:,4)); StrainDat(:,4)];
exy = [flipud(StrainDat(:,5)); StrainDat(:,5)];
eyz = [flipud(StrainDat(:,6)); StrainDat(:,6)];
exz = [flipud(StrainDat(:,7)); StrainDat(:,7)];

ezz =StressOn*( -(C12Ga/C11Ga)*(exx+eyy));

% Matrix Elements of the Pikus-Bir Hamiltonian form from
% Appendix C.2 of Physics of Electronic Devices by S.L. Chuang
    % GaAs Valence Band Parameters
    PeGa = -avGa*(exx + eyy + ezz);
    QeGa = -bGa/2*(exx + eyy - 2*ezz);
    ReGa = ((3/4)^.5*bGa*(exx-eyy)-i*dGa*exy);
    SeGa = -dGa*(exz-i*eyz);
    % GaAs Conduction Band Parameters
    PcGa = acGa*(exx + eyy + ezz);



% GaAs Dimensionless, strain dependent factors (S.L.Chuang book eqn 4.5.38)
% for effective mass corrections
xGa = QeGa/DeltaGa;
fGa = (2*xGa.*(1+3/2*(xGa-1+(1+2*xGa+9*xGa.^2).^0.5))+6*xGa.^2)
./(3/4*(xGa-1+(1+2*xGa+9*xGa.^2).^0.5).^2+xGa-1
+(1+2.*xGa+9*xGa.^2).^0.5-3*xGa.^2);

% [row,col] = find(X, ...) returns the row and column indices
% of the nonzero entries in the matrix X.
[xp,yp]=find(xGa == 0);
```

```
fGa(xp,yp) = 1;

% Effective masses perpendicular (z) and parallel (x-y) in units of
% electron masses (me)
% S.L.Chuang book eqn. 4.5.39
    mhhzGa = 1/(gamma1Ga - 2*gamma2Ga);
    mhhtGa = 1/(gamma1Ga + gamma2Ga);
    mlhzGa = 1./(gamma1Ga + 2*fGa*gamma2Ga);
    mlhtGa = 1./(gamma1Ga - 2*fGa*gamma2Ga);
    msozGa = 1/(gamma1Ga + 2*gamma2Ga);
    msotGa = 1/(gamma1Ga - 2*gamma2Ga);

% Matrix elements, 0 for j=+-2, 2 for light hole and 1 for heavy hole

% note: From the fit of LH and HH exciton coupling in our paper, HH
% \Omega \propto sqrt(f), f \propto |<fin|M|ini>|^2, \Omega \propto <M>

% Right Circularly polarized spin 1
MatElements1(:,1) = [0 7.55 6.0 0 0 0 0 0];

% Left Circularly Polarized spin -1
MatElements2(:,1) = [0 0 0 0 0 6.0 7.55 0];

% Pikus-Bir Hamiltonian for GaAs and AlAs and eigenvales

HydroTerm = (exx + eyy + ezz);

for dox = 1:length(SimXaxis)

% PiezoElectric term
```

```
e14 = 0.16; %Coulombs/m^2
mu = e * 0E-9;
Efield = exy*e14/epsilon;
PiezShift = -mu*Efield/e;

Ehh = (hbar^2*kz^2/(2*e*mhhzGa*me))-PiezShift(dox);
Elh = lhf*(hbar^2*kz^2/(2*e*mlhzGa(dox)*me))-PiezShift(dox);

% Valence band calculations! No Exchange included

MatrGa(1,:) = [Ehh+PeGa(dox)+QeGa(dox) -SeGa(dox) ReGa(dox) 0 ];
MatrGa(2,:) = [-conj(SeGa(dox)) Elh+PeGa(dox)-QeGa(dox) 0 ReGa(dox)];
MatrGa(3,:) = [conj(ReGa(dox)) 0 Elh+PeGa(dox)-QeGa(dox) SeGa(dox) ];
MatrGa(4,:) = [0 conj(ReGa(dox)) conj(SeGa(dox)) Ehh+PeGa(dox)+QeGa(dox)];

% Valence band energy PLUS shift
EvalenceGa = EovavGa + DeltaGa/3 + eig(-MatrGa);
EhhGaA = EvalenceGa(3);
EhhGaB = EvalenceGa(4);
ElhGaA = EvalenceGa(1);
ElhGaB = EvalenceGa(2);

% Conduction Band Energy Plus Shift in eV
EcGa = EovavGa + DeltaGa/3 + EgGa + PcGa(dox)
  + hbar^2*(1*kz)^2/(2*e*mcGa*me);

% Calculation of Confinement energy in a finite quantum well
% follow Chap. 3.2 of S.L.ChuangBook

mrhh = me*(1/mhhtGa + 1/mcGa)^-1;
```

```
mrlh = me*(1/mlhtGa(dox) + 1/mcGa)^-1;
mrso = me*(1/msotGa + 1/mcGa)^-1;

% Rydberg energy for the electron-hole pair
Ryhh = mrhh*e^3/(32*pi^2*epsilon^2*hbar^2);
Rylh = mrlh*e^3/(32*pi^2*epsilon^2*hbar^2);
% Ryso = mrso*e^3/(32*pi^2*epsilon^2*hbar^2);

% Calculation of QW Transition Energy with shift
Emat(dox,1) = EcGa - EhhGaA;
Emat(dox,2) = EcGa - EhhGaB;
Emat(dox,3) = EcGa - ElhGaA;
Emat(dox,4) = EcGa - ElhGaB;

% Calculation with Exchange
ax = -0.0003*xf; %Units of eV
ay = -0.0003*yf;
az = -0.0003*zf;

bx = 0.0*0.00019; %Units of eV
by = 0.0*.8*bx;
bz = 0.0*.0001;

Coup1 = -(ax-ay)/(3^0.5) + (bx-by)*7*(3^0.5)/16;
Coup2 = -(ax+ay)/(3^0.5) + (bx+by)*7*(3^0.5)/16;
Coup3 = (ax+ay)*2/3 + (bx+by)*20/16;
Coup4 = (ax-ay)*2/3 + (bx-by)*20/16;
Coup5 = az/4;
Coup6 = az/12;
```

```
% Coup1 = (ax-ay)*(3^0.5)/4 + (bx-by)*7*(3^0.5)/16;
% Coup2 = (ax+ay)*(3^0.5)/4 + (bx+by)*7*(3^0.5)/16;
% Coup3 = (ax+ay)/2 + (bx+by)*20/16;
% Coup4 = (ax-ay)/2 + (bx-by)*20/16;
% Coup5 = 3*az/4;
% Coup6 = az/4;

Coup7 = bz*27/16;
Coup8 = bz/16;
Coup9 = (bx-by)*6/16;
Coup10 = (bx+by)*6/16;

MatrExch(1,:)=[ Ehh+PeGa(dox)+QeGa(dox)+Coup5+Coup7  0  -SeGa(dox)
Coup1  ReGa(dox)  0  0  Coup10  ];
MatrExch(2,:)=[ 0  Ehh+PeGa(dox)+QeGa(dox)-Coup5-Coup7  Coup2  -SeGa(dox)
0  ReGa(dox)  Coup9  0  ];
MatrExch(3,:)=[ -conj(SeGa(dox))  Coup2
Elh+PeGa(dox)-QeGa(dox)+Coup6+Coup8  0  0  Coup4  ReGa(dox)  0  ];
MatrExch(4,:)=[ Coup1  -conj(SeGa(dox))  0
Elh+PeGa(dox)-QeGa(dox)-Coup6-Coup8  Coup3  0  0  ReGa(dox)  ];
MatrExch(5,:)=[ conj(ReGa(dox))  0  0  Coup3
Elh+PeGa(dox)-QeGa(dox)-Coup6-Coup8  0  SeGa(dox)  Coup1  ];
MatrExch(6,:)=[ 0  conj(ReGa(dox))  Coup4  0  0
Elh+PeGa(dox)-QeGa(dox)+Coup6+Coup8  Coup2  SeGa(dox)  ];
MatrExch(7,:)=[ 0  Coup9  conj(ReGa(dox))  0  conj(SeGa(dox))
Coup2  Ehh+PeGa(dox)+QeGa(dox)-Coup5-Coup7  0  ];
MatrExch(8,:)=[ Coup10  0  0  conj(ReGa(dox))  Coup1  conj(SeGa(dox))
0  Ehh+PeGa(dox)+QeGa(dox)+Coup5+Coup7  ];

   [v,d] = eig(MatrExch); % eigen values at the side of the well
```

```
    for ctr = 1:8
        % oscillator strength for spin 1
        OscStrength1(dox,ctr)= abs(sum(v(:,ctr).*MatElements1)).^2;
        % oscillator strength for spin -1
        OscStrength2(dox,ctr)= abs(sum(v(:,ctr).*MatElements2)).^2;
    end

    if (dox == ceil(length(SimXaxis)*10/21))
     vcenter = v;
    end;
    if (dox == ceil(length(SimXaxis)/4))
     vside1 = v;
    end;

EvalenceGa = EovavGa + DeltaGa/3-d*ones(8,1);

% commented lines are mostly dark (j=0 or j=+-2)
E1 = EvalenceGa(1);
E2 = EvalenceGa(2);
E3 = EvalenceGa(3);
E4 = EvalenceGa(4);
E5 = EvalenceGa(5);
E6 = EvalenceGa(6);
E7 = EvalenceGa(7);
E8 = EvalenceGa(8);

ExchE(dox,1) = EcGa - E1;
ExchE(dox,2) = EcGa - E2;
ExchE(dox,3) = EcGa - E3;
ExchE(dox,4) = EcGa - E4;
```

```
ExchE(dox,5) = EcGa - E5;
ExchE(dox,6) = EcGa - E6;
ExchE(dox,7) = EcGa - E7;
ExchE(dox,8) = EcGa - E8;

end

end
```

G.2 MAIN EXECUTABLE FILE

```
close all
global StrainDat Emat ExchE OscStrength1 OscStrength2 HydroTerm vcenter
vside1 SimXaxis exx eyy ezz exy exz eyz

stressfile = dlmread('ActualSplitting.txt');

StressExchangeUsingANSYSdata(1, 3.8, 3.8, 2.8)

Edgn1=ExchE(:,1);
Edgn2=ExchE(:,2);
Edgn3=ExchE(:,3);
Edgn4=ExchE(:,4);
Edgn5=ExchE(:,5);
Edgn6=ExchE(:,6);
Edgn7=ExchE(:,7);
Edgn8=ExchE(:,8);

Osc1dgn1=OscStrength1(:,1);
```

```
Osc1dgn2=OscStrength1(:,2);
Osc1dgn3=OscStrength1(:,3);
Osc1dgn4=OscStrength1(:,4);
Osc1dgn5=OscStrength1(:,5);
Osc1dgn6=OscStrength1(:,6);
Osc1dgn7=OscStrength1(:,7);
Osc1dgn8=OscStrength1(:,8);

Osc2dgn1=OscStrength2(:,1);
Osc2dgn2=OscStrength2(:,2);
Osc2dgn3=OscStrength2(:,3);
Osc2dgn4=OscStrength2(:,4);
Osc2dgn5=OscStrength2(:,5);
Osc2dgn6=OscStrength2(:,6);
Osc2dgn7=OscStrength2(:,7);
Osc2dgn8=OscStrength2(:,8);

figure

subplot(2,3,1)
plot(SimXaxis,Edgn5,'Color','black','LineWidth',2)
hold on
plot(SimXaxis,Edgn6,':','Color','red','LineWidth',2)
plot(SimXaxis,Edgn7,'Color','green','LineWidth',2)
plot(SimXaxis,Edgn8,':','Color','blue','LineWidth',2)

subplot(2,3,4)
plot(SimXaxis,Edgn1,'Color','black','LineWidth',2)
hold on
plot(SimXaxis,Edgn2,':','Color','red','LineWidth',2)
```

```
plot(SimXaxis,Edgn3,'Color','green','LineWidth',2)
plot(SimXaxis,Edgn4,':','Color','blue','LineWidth',2)

subplot(2,3,2)
plot(SimXaxis,Osc1dgn5,'Color','black','LineWidth',2)
hold on
plot(SimXaxis,Osc1dgn6,':','Color','red','LineWidth',2)
plot(SimXaxis,Osc1dgn7,'Color','green','LineWidth',2)
plot(SimXaxis,Osc1dgn8,':','Color','blue','LineWidth',2)

subplot(2,3,5)
plot(SimXaxis,Osc1dgn1,'Color','black','LineWidth',2)
hold on
plot(SimXaxis,Osc1dgn2,':','Color','red','LineWidth',2)
plot(SimXaxis,Osc1dgn3,'Color','green','LineWidth',2)
plot(SimXaxis,Osc1dgn4,':','Color','blue','LineWidth',2)

subplot(2,3,3)
plot(SimXaxis,Osc2dgn5,'Color','black','LineWidth',2)
hold on
plot(SimXaxis,Osc2dgn6,':','Color','red','LineWidth',2)
plot(SimXaxis,Osc2dgn7,'Color','green','LineWidth',2)
plot(SimXaxis,Osc2dgn8,':','Color','blue','LineWidth',2)

subplot(2,3,6)
plot(SimXaxis,Osc2dgn1,'Color','black','LineWidth',2)
hold on
plot(SimXaxis,Osc2dgn2,':','Color','red','LineWidth',2)
plot(SimXaxis,Osc2dgn3,'Color','green','LineWidth',2)
plot(SimXaxis,Osc2dgn4,':','Color','blue','LineWidth',2)
```

```
% figure
% plot(Edgn3(50:100)-Edgn4(50:100),':','Color','blue','LineWidth',2)

% if change in photon energy is linear only
% Eph = 1.6038 - SimXaxis*2.40E-6;

%if we add a parabolic shift in the energy of the photon
Eph = 1.60355 - SimXaxis*2.40E-6 - 0.35*HydroTerm;

Omega3 = 0.0065*(((Osc1dgn3+Osc2dgn3)/2)/29.5).^0.5;
%Omega4 = 0.007*(((Osc1dgn4+Osc2dgn4)/2)/2+ 0.045*HydroTerm/0.0029).^0.5;

Omega4 = 0.0065*(((Osc1dgn4+Osc2dgn4)/2)/29.5).^0.5;

for n=1:length(Edgn1)

% damping terms does not affect the splitting. It does affect the shift
% of the LP and UP far from resonance

% Hpol1(1,:) = [ Edgn3(n)-i*0.0005   Omega3(n)];
% Hpol1(2,:) = [ Omega3(n) Eph(n)-i*0.0004 ];
%
% Hpol2(1,:) = [ Edgn4(n)-i*0.0005   Omega4(n) ];
% Hpol2(2,:) = [ Omega4(n)  Eph(n)-i*0.0004 ];

  Hpol1(1,:) = [ Edgn3(n)   Omega3(n)];
  Hpol1(2,:) = [ Omega3(n) Eph(n) ];

  Hpol2(1,:) = [ Edgn4(n)   Omega4(n) ];
```

```
  Hpol2(2,:) = [ Omega4(n)  Eph(n) ];

  PolE1(n,:) = real(eig(Hpol1));
  PolE2(n,:) = real(eig(Hpol2));
end

% shape of the actual exciton data.
y0 = 767.19055;
mslope = 0.00076;
Ai = 1142.08324;
wi = 205.39376;
xc = 209.75365;
Aj = 2.1992;
wj = 26.94719;
FileNum=4;
x = [1:420];
ExList =1239.84./(y0 + 0.0015*0.25*FileNum*y0 + mslope*x
+ 0.20*FileNum*(2*Ai*wi/pi./(4*(x - xc).^2 + wi^2)
+ Aj*exp(-((x - xc)/wj).^2)));

filecnt = 10;
file1 = strcat('C:Aug_07_08_FileInfo\aug07_zdeg',num2str(filecnt)
,'_filenfo.txt');
file2 = strcat('C:Aug_07_08_FileInfo\aug07_ndeg',num2str(filecnt)
,'_filenfo.txt');
zdeg = dlmread(file1, '', 'D2..D513');
ndeg = dlmread(file2, '', 'D2..D513');

figure
plot(SimXaxis,Edgn3,'Color','green','LineWidth',2)
```

```
hold on
plot(SimXaxis,Edgn4,':','Color','blue','LineWidth',2)
plot(SimXaxis,Eph)
plot(SimXaxis,PolE1(:,1),'Color','green','LineWidth',2)
plot(SimXaxis,PolE1(:,2),'Color','green','LineWidth',2)
plot(SimXaxis,PolE2(:,1),':','Color','blue','LineWidth',2)
plot(SimXaxis,PolE2(:,2),':','Color','blue','LineWidth',2)
plot(([45:475]-255)/0.476,1239.84./zdeg(45:475))
plot(([45:475]-255)/0.476,1239.84./ndeg(45:475))

lpline1 = PolE1(:,1);
lpline2 = PolE2(:,1);
lpline(:,1)=SimXaxis;
lpline(:,2)=lpline1;
lpline(:,3)=lpline2;

% save('SimSplitLP2.txt', 'lpline', '-ASCII', '-tabs')

a = (lpline1-lpline2);

figure
plot(([0:400]-214)/(0.476),stressfile(45:445,filecnt+1),'Color','black')
hold on
plot(SimXaxis,a,'Color','blue','LineWidth',2)

% save('OffCenterReidStress10.txt', 'a', '-ASCII')

figure

test1=((vside1(2,3)+vside1(3,3))/(vside1(6,3)+vside1(7,3)));
```

```
test2=((vside1(2,4)+vside1(3,4))/(vside1(6,4)+vside1(7,4)));
angle1=(atan2(imag(test1),real(test1))/2);
angle2=(atan2(imag(test2),real(test2))/2);

test3=((vcenter(2,3)+vcenter(3,3))/(vcenter(6,3)+vcenter(7,3)));
test4=((vcenter(2,4)+vcenter(3,4))/(vcenter(6,4)+vcenter(7,4)));
angle3=(atan2(imag(test3),real(test3))/2);
angle4=(atan2(imag(test4),real(test4))/2);

polar((angle1)*ones(1,5),abs(test1)*[0:4]/4,':green');
hold on
polar((angle2)*ones(1,5),abs(test2)*[0:4]/4,':blue');
polar((angle3)*ones(1,5),abs(test3)*[0:4]/4,'green');
polar((angle4)*ones(1,5),abs(test4)*[0:4]/4,'blue');
title('Polarization');
legend('Low Energy, side', 'High Energy, side',
'Low Energy, center','High Energy, center');
```

APPENDIX H

ANSYS INPUT FILE

This input file was slightly modified from R.H. Reid's original model to suit the experimental parameters.

```
finish
/clear

/title, Reid Microcavity Model

! Units:  mks

! Parameters:

tk       =  0.125          !Thickness of chip in mm
ww       =  4.000          !Width of chip in mm
ri       =  0.012         !Load radius in mm
ro       =  0.625          !Support radius in mm

! Good fits with clamps on top condition,
! off center, 25 microns away from center of pin, 125 microns thick
```

```
load     =  4.3/4                !Applied Load in N fits Stress Data 10
!load     =  3.2/4               !Applied Load in N fits Stress Data 8
!load     =  2.1/4               !Applied Load in N fits Stress Data 6
!load     =  1.0/4               !Applied Load in N fits Stress Data 4
!load     =  0.2/4               !Applied Load in N fits Stress Data 2

!exspec   =  86E3                 !Modulus of Elasticity in N/mm^2

!Modeling Divisions:
ne1      = 4                     !Load region
ne2      = 30                    !Middle region
ne3      = 20                    !Outer region
neai     = 20                    !Inner arc
neao     = neai                  !Outer arc
nedge    = neai                  !Outer edge
netk     = 10                    !Through thickness

! Plotting
/triad, off

/CWD,'C:\Documents and Settings\rbb7\Desktop'

/prep7
local, 11, 1
csys, 0
! Keypoints:
k, 1, 0.0000, 0.0000, 0.0000
k, 2,     ri, 0.0000, 0.0000
k, 3,     ro, 0.0000, 0.0000
k, 4,  ww/2., 0.0000, 0.0000
```

```
k, 5,  ww/2.,  ww/2., 0.0000
k, 6, 0.0000,  ww/2., 0.0000
k, 7, 0.0000,     ro, 0.0000
k, 8, 0.0000,     ri, 0.0000
csys,  11
k, 9,     ri,  45.00, 0.0000
k,10,     ro,  45.00, 0.0000
csys,   0
kgen,   2,  all, , , , ,tk, 10
! Lines
l,  1,  2,    ne1      $l, 11, 12,    ne1
l,  2,  3,    ne2      $l, 12, 13,    ne2
l,  3,  4,    ne3      $l, 13, 14,    ne3
l,  1,  8,    ne1      $l, 11, 18,    ne1
l,  8,  7,    ne2      $l, 18, 17,    ne2
l,  7,  6,    ne3      $l, 17, 16,    ne3
l,  4,  5,  nedge      $l, 14, 15,  nedge
l,  5,  6,  nedge      $l, 15, 16,  nedge
csys, 11
l,  2,  9,   neai      $l, 12, 19,   neai
l,  9,  8,   neai      $l, 19, 18,   neai
l,  3, 10,   neao      $l, 13, 20,   neao
l, 10,  7,   neao      $l, 20, 17,   neao
csys, 0
l,  9, 10,    ne2      $l, 19, 20,    ne2
l, 10,  5,    ne3      $l, 20, 15,    ne3
csys, 0
l,  1, 11,   netk                          !Vertical Lines
l,  2, 12,   netk
l,  3, 13,   netk
```

```
l,  4, 14,   netk
l,  5, 15,   netk
l,  6, 16,   netk
l,  7, 17,   netk
l,  8, 18,   netk
l,  9, 19,   netk
l, 10, 20,   netk
!Volumes:
v,  1,  2,  9,  8, 11, 12, 19, 18
v,  2,  3, 10,  9, 12, 13, 20, 19
v,  9, 10,  7,  8, 19, 20, 17, 18
v,  3,  4,  5, 10, 13, 14, 15, 20
v, 10,  5,  6,  7, 20, 15, 16, 17

ET,1,SOLID185 ! Define elment type
! Available anisotropic solids in ANSYS
! 185, 186, 187, 5, 98, 226, 227
! or from Chap. 4.64 SOLID64 3-D Anisotropic Solid

!! Material Properties:
!mp, ex, 1, exspec

TB,ANEL,1,1,21,0 ! Define elastic tensor in N/mm^2
TBTEMP,0
TBDATA,,12.11e4,5.48e4,5.48e4,0,0,0
TBDATA,,12.11e4,5.48e4,0,0,0,12.11e4
TBDATA,,0,0,0,6.04e4,0,0
TBDATA,,6.04e4,0,6.04e4,,,

! Create Elements:
```

```
mshape, 0
vmesh, all

! Boundary Conditions:

csys, 11
ksel, s, loc, x, ro
ksel, r, loc, z, 0
csys, 0
lslk, s, 1
dl, all,, uz,0                    !Circular Support
alls

csys, 11  !Cylindrical coordinate
nsel, s, loc, x, ro, ww
nsel, r, loc, z, tk
d, all, uz, 0                     !Circular top clamp
csys, 0  !Cartesian coordinates
alls

csys, 11  !Cylindrical coordinate
nsel, s, loc, x, ro, ww
nsel, r, loc, z, 0
d, all, uz,0                     !Circular bottom clamp
csys, 0   !Cartesian coordinates
alls

csys, 0
ksel, s, loc, x, 0
```

```
lslk, s, 1
asll, s, 1
nsla, s, 1
dsym, symm, x, 0                !Symmetry about y-axis
alls

csys, 0
ksel, s, loc, y, 0
lslk, s, 1
asll, s, 1
nsla, s, 1
dsym, symm, y, 0                !Symmetry about x-axis
alls

! Apply Load:

!ksel, s, kp, , 11
!nslk, s
!*get, nnload, node, 0, num, max
!f, nnload, fz, -load
!alls

csys, 11 !Cylindrical coordinate
nsel, s, loc, x, 0, ri
nsel, r, loc, z, tk
*get, ncount, node, 0, count
f, all, fz,-load/ncount
csys, 0 !Cartesian coordinates
alls
```

```
! Transfer loads to model:

sbctran
/pbc, all, 1
eplo
fini

! Solve
/sol
solve
fini

! Post-Process:
/post1

PATH,LinePath,2,300,300,!Define path for data
PPATH,1,0,0.00132,0.02497,0.0025,0,!Path 0.0025 mm away from the bottom,
!25 microns off center give better results
PPATH,2,0,0.475,0,0.0025,0,

AVPRIN,0, ,  !Define what we need Exx, Eyy etc
PDEF, ,EPEL,X,AVG

AVPRIN,0, ,
PDEF, ,EPEL,Y,AVG

AVPRIN,0, ,
PDEF, ,EPEL,Z,AVG

AVPRIN,0, ,
```

```
PDEF, ,EPEL,XY,AVG

AVPRIN,0, ,
PDEF, ,EPEL,YZ,AVG

AVPRIN,0, ,
PDEF, ,EPEL,XZ,AVG

PLPATH,EPELX,EPELY,EPELZ,EPELXY,EPELYZ,EPELXZ !Plot strain

/PAGE,1000,,1000,
/OUTPUT,test,txt,

PRPATH,EPELX,EPELY,EPELZ,EPELXY,EPELYZ,EPELXZ !List strain
```

BIBLIOGRAPHY

[1] Leggett, A. *Rev. Mod. Phys.* **73**, 307–356 (2001).

[2] Lifshitz, E. and Pitaevskii, L. *Statistical Physics Part 2.* Pergamon Press, (1980).

[3] Nozieres, P. and Pines, D. *Theory of Quantum Liquids.* Perseus Books, (1999).

[4] Annett, J. *Superconductivity, Superfluids and Condensates.* Oxford University Press, (2004).

[5] Anderson, M., Ensher, J., Matthews, M., Wieman, C., and Cornell, E. *Science* **269**, 198 (1995).

[6] Davis, K., Mewes, M.-O., Andrews, M., van Druten, N., Durfee, D., Kurn, D., and Ketterle, W. *Phys. Rev. Lett* **75**, 3969–3973 (1995).

[7] Chu, S., Hollberg, L., Bjorkholm, J. E., Cable, A., and Ashkin, A. *Phys. Rev. Lett.* **55**(1), 48–51 Jul (1985).

[8] Deng, H., Weihs, G., Snoke, D., Bloch, J., and Yamamoto, Y. *Proc. Nat. Acad. Sci.* **100**, 15318 (2003).

[9] Weihs, G., Deng, H., Snoke, D., and Yamamoto, Y. *Proc. Nat. Acad. Sci. (a)* **201**, 625 (2004).

[10] Weihs, G., Deng, H., Huang, R., Sugita, M., Tassone, F., and Yamamoto, Y. *Semi. Sci. Tech.* **18**, S386 (2003).

[11] Doan, T., Cao, H. T., Thoai, D. T., and Haug, H. *Phys. Rev. B* **72**, 085301 (2005).

[12] Kundermann, S., Saba, M., Ciuti, C., Guillet, T., Oesterle, U., Staehli, J. L., and Deveaud, B. *Phys. Rev. Lett.* **91**(10), 107402 Sep (2003).

[13] Laussy, F., Malpuech, G., Kavokin, A., and Bigenwald, P. *Phys. Rev. Lett.* **93**, 016402 (2004).

[14] Huynh, A., Tignon, J., Larsson, O., Roussignol, P., Delalande, C., Andre, R., Romestain, R., and Dang, L. *Phys. Rev. Lett.* **90**, 106401 (2003).

[15] Stevenson, R., Astratov, V., Skolnick, M., Whittaker, D., Emam-Ismail, M., Tartakovskii, A., Savvidis, P., Baumberg, J., and Roberts, J. *Phys. Rev. Lett.* **85**, 3680 (2000).

[16] Poras, D., Ciuti, C., Baumberg, J., and Tejedor, C. *Phys. Rev. B* **66**, 085304 (2002).

[17] Keeling, J., Eastham, P. R., Szymańska, M. H., and Littlewood, P. B. *Phys. Rev. Lett.* **93**(22), 226403 Nov (2004).

[18] Messin, G., Karr, J., Baas, A., Khitrova, G., Houdre, R., Stanley, R., Oesterle, U., and Giacobino, E. *Phys. Rev. Lett.* **87**, 127403 (2001).

[19] Snoke, D. *Science* **298**, 1368 (2002).

[20] Hopfield, J. *Phys. Rev.* **112**, 1555–1567 (1958).

[21] Andreani, C., Tassone, F., and Bassani, F. *Solid State Comm.* **77**, 641–645 (1991).

[22] Deveaud, B., Clerot, F., Roy, N., Satzke, K., Sermage, B., and Katzer, D. *Phys. Rev. Lett.* **67**, 2355–2358 (1991).

[23] Weisbuch, C., Nishioka, M., Ishikawa, A., and Arakawa, Y. *Phys. Rev. Lett.* **69**, 3314 (1992).

[24] Agarwal, G. S. *Phys. Rev. Lett.* **53**(18), 1732–1734 Oct (1984).

[25] Zhu, Y., Gauthier, D., Morin, S., Wu, Q., Carmichael, H., and Mossberg, T. *Phys. Rev. Lett* **64**, 2499–2502 (1990).

[26] Andreani, L., Savona, V., Schwendimann, P., and Quattropani, A. *Superlattices Microstruct.* **15**, 453–458 (1994).

[27] Savona, V., Andreani, L., Schwendimann, P., and Quattropani, A. *Solid State Comm.* **93**, 733–739 (1994).

[28] Imamoglu, A., Ram, R., Pau, S., and Yamamoto, Y. *Phys. Rev. A* **53**, 4250 (1996).

[29] Dang, L., Heger, D., André, R., Boeuf, F., and Romestain, R. *Phys. Rev. Lett.* **81**, 3920 (1998).

[30] Senellart, P. and Bloch, J. *Phys. Rev. Lett.* **82**, 1233 (1999).

[31] Boeuf, F., André, R., Romestain, R., Dang, L., Péronne, E., Lampin, J., Hulin, D., and Alexandrou, A. *Phys. Rev. B* **62**, R2279 (2000).

[32] Langbein, W. In *The Physics of Semiconductor Microcavities,* Deveaud, B., editor, 171–185. Wiley, (2007).

[33] Ciuti, C. *Phys. Rev. B* **69**(24), 245304 Jun (2004).

[34] Ballarini, D., Sanvitto, D., Amo, A., na, L. V., Wouters, M., Carusotto, I., Lemaitre, A., and Bloch, J. *Physical Review Letters* **102**(5), 056402 (2009).

[35] Sermage, B., Long, S., Abram, I., Marzin, J., Bloch, J., Planel, R., and Thierry-Mieg, V. *Phys. Rev. B* **53**, 16516 (1996).

[36] Kavokin, A. and Malpuech, G. *Cavity Polaritons*. Elsevier, (2005).

[37] Balili, R., Hartwell, V., Snoke, D., Pfeiffer, L., and West, K. *Science* **316**, 1007 (2007).

[38] Hartwell, V. *Dynamics of Trapped Polaritons in Stressed GaAs Quantum Well-Microcavity Structures: Experiments and Numerical Simulations*. PhD thesis, University of Pittsburgh, (2008).

[39] Tassone, F., Piermarocchi, C., Savona, V., Quattropanni, A., and Schwendimann, P. *Phys. Rev. B* **56**, 7554 (1997).

[40] Balili, R., Snoke, D., Pfeiffer, L., and West, K. *Appl. Phys. Lett.* **88**, 031110 (2006).

[41] Snellart, P., Bloch, J., Sermage, B., and Marzin, J. *Phys. Rev. B.* **62**, R16263 (2000).

[42] Kavokin, A., Baumberg, J., Malpuech, G., and Laussy, G. *Microcavities*. Oxford University Press, (2007).

[43] Savvidis, P., Baumberg, J., Stevenson, R., Skolnick, M., Whittaker, D., and Roberts, J. *Phys. Rev. Lett* **84**, 1547 (2000).

[44] Savvidis, P., Baumberg, J., Porras, D., Skolnick, M., Whittaker, D., and Roberts, J. *Phys. Rev. B* **65**, 073309 (2002).

[45] Baumberg, J., Savvidis, P., Stevenson, R., Tartakovskii, A., Skolnick, M., Whittaker, D., and Roberts, J. *Phys. Rev. B* **62**, R16247 (2000).

[46] Whittaker, D. *Phys. Rev. B* **64**, 193305 (2001).

[47] Ciuti, C., Schwendimann, P., and Quattropanni, A. *Semicon. Sci. Technol.* **18**, S279–S293 (2003).

[48] Savona, V., Schwendimann, P., and Quattropani, A. *Phys. Rev. B* **71**(12), 125315 Mar (2005).

[49] Blakemore, J. S. *Journal of Applied Physics* **53**(10), R123–R181 (1982).

[50] Afromowitz, M. *Solid State Comm.* **15**, 59–63 (1974).

[51] Gehrsitz, S., Reinhart, F., Gourgon, C., Herres, N., Vonlanthen, A., and Sigg, H. *Journal of Applied Physics* **87**, 7825 (2000).

[52] Stanley, R., Houdre, R., Weisbuch, C., Oesterle, U., Gailhanou, M., and Ilegems, M. *Appl. Phys. Lett.* **65**, 1883 (1994).

[53] Snoke, D. *Solid State Physics: Essential Concepts*. Addison-Wesley, (2009).

[54] Berezinskii, V. *Soviet Phys. JETP* **34**, 610 (1971).

[55] Kosterlitz, J. and Thouless, D. *J. Phys. C.* **6**, 1181 (1973).

[56] Mullin, W. *J. Low. Temp. Phys.* **106**, 615 (1997).

[57] Bagnato, V. and Kleppner, D. *Phys. Rev. A.* **44**, 7439 (1991).

[58] Fernandez, J. and Mullin, W. *J. Low Temp. Phys.* **128**, 233 (2002).

[59] Berman, O., Lozovik, Y., and Snoke, D. *Phys. Rev. B* **77**, 155317 (2008).

[60] Huang, K. In *Bose-Einstein Condensation,* Griffin, A., Snoke, D., and Stringari, S., editors, 31–50. Cambridge University Press, (1995).

[61] Ohta, T. and Jasnow, D. *Phys. Rev. B* **20**(1), 139–146 Jul (1979).

[62] Nelson, D. and Kosterlitz, J. *Phys. Rev. Lett.* **39**, 1201 (1977).

[63] Combescot, M. and Snoke, D. *Phys. Rev. B* **78**, 144303 (2008).

[64] Moskalenko, S. and Snoke, D. *Bose-Einstein Condensation of Excitons and Biexcitons*. Cambridge University Press, (2000).

[65] Snoke, D. *Solid State Comm.* **146**, 73 (2008).

[66] Bajoni, D., Senellart, P., Lemaître, A., and Bloch, J. *Phys. Rev. B* **76**, 201305(R) (2007).

[67] Thomas, G., Rice, T., Hensel, J., and Phillips, P. In *Solid State Physics,* Ehrenreich, H., Seitz, F., and Turnbull, D., editors, volume 32. Academic Press, (1977).

[68] Deng, H., Weihs, G., Santori, C., Bloch, J., and Yamamoto, Y. *Science* **298**, 199 (2002).

[69] Bloch, J., Freixanet, T., Marzin, J. Y., Thierry-Mieg, V., and Planel, R. *Applied Physics Letters* **73**(12), 1694–1696 (1998).

[70] Dickerson, J. H., Son, J. K., Mendez, E. E., and Allerman, A. A. *Phys. Lett.* **81**, 803 (2002).

[71] Stanley, R., Houdre, R., Weisbuch, C., Oesterle, U., and Ilegrams, M. *Phys. Rev. B* **53**, 10995 (1996).

[72] Sermage, B., Malpuech, G., Kavokin, A., and Thierry-Mieg, V. *Phys. Rev. B* **64**, R081303 (2001).

[73] Christophoulos, S., Baldassari, G., Grundy, A., Lougoudakis, P., Kavokin, A., Baumberg, J., Christmann, G., Butté, R., Feltin, E., Carlin, J., and Grandjean, N. *Phys. Rev. Lett.* **98**, 126405 (2007).

[74] Snoke, D. *Phys. Stat. Sol. (b)* **238**(3), 389–396 (2003).

[75] Bajoni, D., Senellart, P., Wertz, E., Sagnes, I., Miard, A., Lemaître, A., and Bloch, J. *Physical Review Letters* **100**(4), 047401 (2008).

[76] Daïf, O. E., Baas, A., Guillet, T., Brantut, J., Kaitouni, R. I., Staehli, J. L., Morier-Genoud, F., and Devaud, B. *Appl. Phys. Lett.* **88**, 061105 (2006).

[77] Yu, P. Y. and Cardona, M. *Fundamentals of Semiconductors*. Springer, 3rd. edition, (1996).

[78] Chuang, S. *Physics of Electronic Devices*. Wiley, (1995).

[79] Cottam, R. and Saunders, G. *J. Phys. C.: Solid State Phys.* **6**, 2105 (1973).

[80] Negoita, V., Snoke, D. W., and Eberl, K. *Appl. Phys. Lett.* **75**, 2059 (1999).

[81] Berman, O., Lozovik, Y., and Snoke, D. *Phys. Stat. Sol. (c)* **3**(10), 3373–3377 (2006).

[82] Davis, K., Mewes, M.-O., Joffe, M., Andrews, M., and Ketterle, W. *Phys. Rev. Lett.* **74**, 5202 (1995).

[83] K.B. Davis and, M.-O. M. and Ketterle, W. *Appl. Phys. B* **60**, 155–159 (1995).

[84] Ficek, Z. and Swain, S. *Quantum Interference and Coherence: Theory and Experiments*. Springer, (2004).

[85] Stern, M., Garmider, V., Umansky, V., and Bar-Joseph, I. *Phys. Rev. Lett.* **100**, 256402 (2008).

[86] Katkov, M. V., Pershin, Y. V., and Piermarocchi, C. *Physical Review B (Condensed Matter and Materials Physics)* **74**(22), 224306 (2006).

[87] Goldman, V. V., Silvera, I. F., and Leggett, A. J. *Phys. Rev. B* **24**, 2870 (1981).

[88] Kasprzak, J. and et. al. *Nature* **443**, 409 (2006).

[89] Sarchi, D. and Savona, V. *Phys. Rev. B* **75**, 115326 (2007).

[90] Balili, R., Nelsen, B., Snoke, D., Pfeiffer, L., and West, K. *Phys. Rev. B* **79**, 075319 (2009).

[91] Love, A., Krizhanovskii, D., Whittaker, D., Bouchekioua, R., Sanvitto, D., S. Al Rizeiqi, R. B., Skolnick, M., Eastham, P., André, R., and Dang, L. S. *Phys. Rev. Lett* **101**, 067404 (2008).

[92] Bajoni, D., Senellart, P., Wertz, E., Sagnes, I., Miard, A., Lemaître, A., and Bloch, J. *Phys. Rev. Lett* **100**, 047401 (2008).

[93] Szymańska, M. H., Keeling, J., and Littlewood, P. N. *Phys. Rev. Lett.* **96**, 230602 (2006).

[94] Sarchi, D. and Savona, V. *Phys. Stat. Sol. B* **243**, 2317 (2006).

[95] Doan, T., Cao, H. T., Thoai, D. T., and Haug, H. *Phys. Rev. B* **77**, 075320 (2008).

[96] Laussy, F., Shelykh, I., Malpuech, G., and Kavokin, A. *Phys. Rev. B* **73**, 035315/1–11 (2006).

[97] Malpuech, G., Glazov, M., Shelykh, I., Bigenwald, P., and Kavokin, K. *Appl. Phys. Lett* **88**, 111118 (2006).

[98] Ivchenko, E., Kaminski, A., and Rössler, U. *Phys. Rev. B* **54**, 5852 (1996).

[99] Romanov, N. and Baranov, P. *Nanotechnology* **12**, 585–590 (2001).

[100] Jorda, S., Rössler, U., and Broido, D. *Phys. Rev. B* **48**(3), 1669–1677 Jul (1993).

[101] Seguin, R., Schliwa, A., Rodt, S., Pötschke, K., Pohl, U., and Bimberg, D. *Physica E* **32**, 101 (2006).

[102] van Kesteren, H. W., Cosman, E. C., van der Poel, W. A. J. A., and Foxon, C. T. *Phys. Rev. B* **41**(8), 5283–5292 Mar (1990).

[103] Cho, K. *Phys. Rev. B* **14**(10), 4463–4482 Nov (1976).

[104] Klopotowski, L., Martin, M., Amo, A., Vina, L., Shelykh, I., Glazov, M., Malpuech, G., Kavokin, A., and André, R. *Sol. Stat. Comm.* **139**, 511 (2006).

[105] Vörös, Z. *Interaction of Excitons in Two-dimensional Potentials*. PhD thesis, University of Pittsburgh, (2008).

[106] Ivchenko, E. and Pikus, G. *Superlattices and Other Heterostructures*. Springer, 2nd. edition, (1997).

[107] Snoke, D. *Nature* **4**, 673 (2008).

[108] Amo, A., Sanvitto, D., Laussy, F. P., Ballarini, D., del Valle, E., Martin, M. D., Lemaître, A., Bloch, J., Krizhanovskii, D. N., Skolnick, M. S., Tejedor, C., and na, L. V. *Nature* **457**, 291–295 (2009).

[109] Lagoudakis, K., Wouters, M., Richard, M., Baas, A., Carusotto, I., André, R., Dang, L. S., and Deveaud-Plédran, B. *Nature* **4**, 706–710 (2008).

[110] Bogoliubov, N. *J. Phys. (USSR)* **11**, 23 (1947).

[111] Utsonomiya, S., Tian, L., Roumpos, G., Lai, C., Kumada, N., Fujisawa, T., Kuwata-Gonokami, M., Löffler, A., Höfling, S., Forchel, A., and Yamamoto, Y. *Nature* **4**, 700–705 (2008).

[112] Baas, A., Lagoudakis, K. G., Richard, M., André, R., Dang, L. S., and Deveaud-Plédran, B. *Physical Review Letters* **100**(17), 170401 (2008).

[113] Christopoulos, S., von Högersthal, G. B. H., Grundy, A., Lagoudakis, P., Kavokin, A., Baumberg, J., Christmann, G., Butté, R., Feltin, E., Carlin, J.-F., and Grandjean, N. *Physical Review Letters* **98**(12), 126405–[4pp] March (2007).

[114] Kittel, C. *Quantum Theory of Solids*. Wiley, 2nd. rev. edition, (1987).

[115] Quattropani, A., Andreani, L., and Bassani, F. *Il Nuovo Cimento* **7 D**, N. 1 (1986).

[116] Jackson, J. *Classical Electrodynamics*. Wiley, 3rd. edition, (1999).

[117] Klingshirn, C. *Semiconductor Optics*. Springer, 3rd. edition, (2007).

[118] Pathria, R. *Statistical Mechanics*. Elsevier, 2nd. edition, (1996).